DFT and DMFT: Implementations and Applications to the Study of Correlated Materials

By

ERIK RYAN YLVISAKER
B.S. (Southern Oregon University) 2003
M.S. (University of California, Davis) 2004

DISSERTATION

Submitted in partial satisfaction of the requirements for the degree of

DOCTOR OF PHILOSOPHY

in

PHYSICS

in the

OFFICE OF GRADUATE STUDIES

of the

UNIVERSITY OF CALIFORNIA

DAVIS

Approved:

Committee in Charge

2008

Abstract

While DFT-LDA has enjoyed great success in describing many ground-state properties of solids, there is an ever increasing list of materials which are not described even qualitatively correct in DFT-LDA. Here I describe some applications of DFT and dynamical mean field theory.

This dissertation is divided into two parts. Part I describes the theoretical background of DFT and DMFT, and the simplest extension to DFT to study correlated materials, LDA+U, is examined in detail. We find that the behavior of LDA+U can differ quite strongly between AMF and FLL, the two commonly used double-counting functionals. AMF has a strong energetic penalty for magnetic states, which roughly cancels the exchange splitting found in LSDA. In Part I, I also describe in detail the implementation of LDA+DMFT in the publicly available code FPLO.

Part II focuses on applications. I describe the application of LDA to $LiNbO_2$, where Wannier functions and effective tight-binding Hamiltonians are constructed for $LiNbO_2$. We found that second neighbor hopping t_2 is the largest, but the first neighbor hopping depends strongly on the Nb-O distance, so that with small variations of O position t_1 varies by an order of magnitude. I also describe in part II the application of LDA in density functional perturbation theory (DFPT) to calculate phonons for Al, Na and diamond to compute melting curves using the Lindemann criteria. The resulting $T_m(P)$ curves agree rather well with experiment in most conditions for these materials, including reproducing the drop of 300 K of T_m in bcc-Na. Detailed calculations in LDA+DMFT using Hubbard I and QMC impurity solvers are used to describe the valence transition in Yb. The QMC calculations showed some unique ergodicity which proved difficult to deal with. The agreement with experimental XAES and RIXS measurements of n_f is rather good, and even the highly approximate Hubbard I impurity solver gives reasonably good results. Finally, I discuss the application of LDA+U to molecular orbitals in RbO_2 to examine the possibility of orbital ordering in the O π^* orbitals. The orbital ordering in this system is highly frustrated, which is likely responsible for the many low-temperature structural

distortions seen experimentally. Two kinds of orbital ordering are found, depending on the parameters U and U' which describe intraorbital repulsion and interorbital repulsion for the π_x^* and π_y^* orbitals.

Contents

1 Introduction **1**

I Methods **4**

2 Density Functional Theory **5**
2.1 Introduction . . . 5
2.2 DFT Method . . . 6
2.2.1 Hohenberg-Kohn Theorem . . . 6
2.2.2 The Kohn-Sham Auxilliary System . . . 7
2.3 Exchange Correlation Approximations . . . 10
2.3.1 Local Density Approximation . . . 10
2.3.2 Generalized Gradient Approximation . . . 11
2.4 Density Functional Perturbation Theory . . . 12
2.4.1 Phonons . . . 13
2.5 Basis Sets . . . 14
2.5.1 Planewaves . . . 15
2.5.2 Local Orbitals (FPLO) . . . 17
2.6 Wannier Functions . . . 18
2.7 Tight Binding . . . 20

3 LSDA+U **22**
3.1 Introduction . . . 22
3.2 The LSDA+U Correction ΔE . . . 27
3.2.1 Short formal background to the LSDA+U method. . . . 28
3.2.2 Fluctuation forms of LSDA+U . . . 30
3.2.3 The Fully Localized Limit (FLL) Functional . . . 31
3.2.4 Implementation of LSDA+U in Some Widely Used Codes . . . 32
3.2.5 General Remarks . . . 32
3.3 Analysis of the Functionals . . . 33
3.4 Fractional Occupations . . . 37
3.5 Orbital Potential Matrix Elements . . . 39
3.6 Numerical Results . . . 41
3.7 Discussion . . . 46
3.7.1 Examples of LSDA+U behavior from applications . . . 47

3.8 Acknowledgments . . . 51
3.9 Calculation of the Stoner I for $3d$ and $4f$ Shells . . . 51

4 Dynamical Mean Field Theory **55**
4.1 Introduction . . . 55
4.2 Cavity Method Derivation . . . 55
4.3 Method . . . 59
4.4 Hubbard I Impurity Solver . . . 61
4.4.1 Vanilla HI . . . 61
4.4.2 HI with exchange . . . 65
4.4.3 Connecting the Crystal Problem with the Impurity Problem . . . 66
4.5 Hirsch-Fye Quantum Monte Carlo Impurity Solver . . . 68
4.5.1 Analytic Continuation . . . 71
4.5.2 Orbital Susceptibility . . . 73

5 Charge Self-Consistent LDA+DMFT **75**
5.1 Local Orbital Basis . . . 75
5.1.1 Nonorthogonal Basis . . . 75
5.1.2 Second Quantization . . . 76
5.2 LDA+DMFT . . . 78
5.2.1 Double Counting . . . 78
5.2.2 DMFT Interface with FPLO . . . 80
5.2.3 Calculation of Local Orbital Occupation Values . . . 80
5.2.4 Computation of Crystal Green's Function . . . 84
5.2.5 Mixing . . . 85
5.2.6 Charge self-consistency . . . 86
5.3 Pole Expansion of Self-Energy . . . 88
5.4 Parabolic Guess for Chemical Potential . . . 90

II Applications **92**

6 Wannier Functions in $LiNbO_2$ **93**
6.1 Introduction . . . 93
6.2 Structure . . . 96
6.3 Electronic Structure Calculations . . . 97
6.4 Zone Center Wave functions . . . 99
6.5 Wannier Function . . . 100
6.6 Tight Binding . . . 104
6.7 Zone Center Vibrational Modes . . . 110
6.7.1 Phonon mode descriptions . . . 112
6.7.2 Clarifying Comments . . . 113
6.8 Effective charges . . . 114
6.9 Summary . . . 115
6.10 Acknowledgments . . . 116

7 Gruneisen Parameters and Equation of State **117**
7.1 Introduction . . . 117
7.2 Theoretical Background . . . 119
7.2.1 Grüneisen Parameter . . . 119
7.2.2 Melting Rules . . . 120
7.3 Method . . . 121
7.4 Materials . . . 122
7.4.1 Aluminum . . . 123
7.4.2 Sodium . . . 124
7.4.3 Diamond . . . 127
7.5 Conclusion . . . 128

8 DMFT applied to Yb Valence Transition **130**
8.1 Introduction . . . 130
8.2 Calculations . . . 131
8.2.1 DFT-LDA calculations . . . 131
8.2.2 All electron LDA+DMFT . . . 132
8.2.3 Hubbard Parameters . . . 133
8.3 Equation of State . . . 134
8.4 Orbital occupation . . . 135
8.4.1 QMC Ergodicity . . . 138
8.4.2 Spectral Function . . . 140
8.5 Conclusion . . . 141
8.6 Acknowledgements . . . 142

9 Orbital Ordering in RbO_2 **143**
9.1 Introduction . . . 143
9.2 Tight Binding Hamiltonian . . . 144
9.3 Poor Man's LDA+U method . . . 149
9.4 Conclusion . . . 153

Bibliography **156**

List of Figures

3.1 Angular momentum values for AMF and FLL . . . 41
3.2 ΔE^{FLL} vs. ΔE^{AMF} . . . 43
3.3 Scatter plot of energies for all states in AMF, FLL and Fl-nS . . . 45
3.4 Shell-Stoner integrals for the $3d$ and $4f$ atoms. . . . 52

4.1 Schematic of the DMFT cycle. . . . 60
4.2 Comparison of $\Sigma(\omega)$ for HI at selected μ values. . . . 67

6.1 Band structure for $LiNbO_2$ . . . 97
6.2 Partial density of states for Nb and O atoms in $LiNbO_2$ . . . 98
6.3 Isosurface plot of Γ-point wavefunctions . . . 100
6.4 Isosurface plot of Nb d_{z^2} Wannier function in $LiNbO_2$ . . . 101
6.5 Isosurface plot of $|W_{z=0.1359}(\mathbf{r})| - |W_{z=0.1263}(\mathbf{r})|$ . . . 102
6.6 Band structure for $LiNbO_2$ with $z = 0.1167$ . . . 104
6.7 Band structure for $LiNbO_2$ with $z = 0.1359$ . . . 105

7.1 Calculated Grüneisen parameter for Na, Al and diamond. . . . 122
7.2 Melting curve for aluminum . . . 124
7.3 Phonon moments ω_n for Al and Na . . . 125
7.4 Calculated phase diagram of Na, compared to experiment and molecular dynamics calculations . . . 126
7.5 Melt curve of diamond, compared to other theoretical methods . . . 128

8.1 Plot of LDA+DMFT parameters U and ε_f . . . 133
8.2 Plot of P-V curves from LDA, GGA and LDA+DMFT(HI) . . . 134
8.3 Yb f occupation under pressure, compared to experiment . . . 136
8.4 Calculated n_f for Yb at temperatures 16 K, 630 K, and 1580 K . . . 137
8.5 Distribution of sampled Hubbard-Stratonovich field configurations . . . 139
8.6 Spectral density of Yb from LDA+DMFT(HI) . . . 140

9.1 Structure of RbO_2 . . . 145
9.2 Band structure and DOS from LDA at $V = V_0$ . . . 146
9.3 Band structure and DOS from LDA at $V = 0.65V_0$ . . . 147
9.4 Tight-binding schematic . . . 148
9.5 Tight-binding parameters vs. volume . . . 150
9.6 U-U' phase diagram of RbO_2 . . . 154
9.7 Density of states for various phases in RbO_2 . . . 155

Chapter 1

Introduction

In the past 40 years, the density functional theory (DFT) developed by Kohn and Sham [1] has had a great deal of success in describing the quantum mechanical ground state of electrons in systems of interest in quantum chemistry and solid-state physics. This is in no small part thanks to accurate approximations to the exchange-correlation functional, such as those described in Refs. [2] and [3]. DFT has been successfully applied to a wide range of materials in condensed matter physics, from simple elements to complex compounds, both as atoms, molecules, or three dimensional solids, as well as two dimensional interfaces and surfaces. It can in many cases accurately predict a variety of material properties. Spin-dependent exchange-correlation functionals have allowed DFT to be applied to both ferromagnetic and antiferromagnetic materials. Properties such as the equation of state (P-V curves and structural phase transitions), and the existence of magnetic phases have been succesfully and accurately computed with DFT for many materials.

Extensions of DFT like linear response [4] and density functional perturbation theory [5] have allowed computation of response to external perturbations, such as atomic displacements or infinitesimal electric fields. These approaches have beeen used to calculate phonon frequencies in a wide range of materials, as well as Born effective charges of ions. These methods have also been used to calculate electron-phonon interactions to compute superconductivity properties in BCS theory.

In spite of DFT's successes, there exists a growing class of materials for which DFT fails to adequately describe, even qualitatively. Most of these materials contain localized d and f electrons whose contributions to exchange and correlation are not accurately computed in the commonly used local density approximation. This results in two common issues; the inaccurately calculated exchange results in a large self-interaction, and the splitting between occupied and unoccupied states ends up being too small (and often zero).

A variety of approaches have been developed for overcoming the shortcomings of DFT. The most basic method is the LDA+U method, where to the DFT functional is added an orbital-dependent interaction term characterized by an energy scale U, the screened Coulomb interaction between the correlated orbitals. This method has worked well in describing several materials which fall into a class of materials termed Mott insulators. The high temperature superconducting cuprates are among the most well known successes of LDA+U. In these materials, LDA+U has successfully produced the antiferromagnetic insulating ground state of the undoped cuprates. LDA+U has also been applied to model the remarkable $Na_{1-x}CoO_2$ systems and the unusual volume and moment collapse transitions of MnO.

LDA+U, being the most basic approximation to many-body effects, has some notable failures. It is certainly not expected to adequately describe a system which is not a good Mott insulator, or at least such a description with LDA+U is questionable at best. Notable failures of the application of LDA+U to elements include Pu, where the phase diagram is extremely complex, and Yb, where the valence transition is gradual under pressure. There are many methods which go beyond LDA+U, but the one of interest here (and the next most simplest after LDA+U) is dynamical mean field theory (DMFT). DMFT (or LDA+DMFT) goes beyond LDA+U by allowing the interaction potential of the correlated orbitals to be energy (frequency) dependent. This frequency dependent potential, or self-energy, is computed for the correlated orbitals only using many-body techniques within an accurate impurity solver. This calculation can be done as accurately as one desires, and it is significantly cheaper in CPU time than solving a full many-body problem for all the

orbitals. DMFT does neglect spatial correlations however. There are also several methods which go beyond DMFT, to treat impurity clusters rather than single site impurities in order to recapture some of the spacial correlations lost in DMFT. The dynamical cluster approximation [6] is one such method, where a course grained **k**-dependence of the self-energy is retained.

This dissertation is broken up into two parts, part I being methods and part II discussing applications. First in chapter 2, the theoretical background of DFT is reviewed. Then in chapter 3, I examine the behavior of the LSDA+U method in detail based on energetic arguments and compare various LDA+U functionals. In chapter 4, I have a summary of the theoretical background of DMFT, as well as detailed descriptions of two impurity solvers (which could be considered the most and least accurate impurity solvers available). In chapter 5, I describe an implementation of LDA+DMFT that I wrote and integrated with the FPLO electronic structure code.

In part II, chapters 6 and 7 discuss applications of DFT to various materials. Chapter 6 covers $LiNbO_2$, a material which superconducts when hole doped by removing Li. Chapter 7 includes equation of state calculations for three elements, Na, Al and diamond. Chapter 8 discusses LDA+DMFT application to the valence transition under pressure that is seen in Yb. Chapter 9 discusses the interesting molecular solid RbO_2.

Part I

Methods

Chapter 2

Density Functional Theory

2.1 Introduction

Early on in the study of extended periodic systems, it was realized that the wavefunction approach presented by Schrödinger would be rather unweildy for systems containing many identical and interacting particles. One approach that has enjoyed a great deal of success is to recast the problem so that the basic variable is the real-space density $n(\mathbf{r})$, a function of only three variables. Then the total energy is constructed as a functional of the density. The earliest tractable approach using density functionals was the Thomas-Fermi method, which had several failings, such as the inability to bind atoms to form molecules. [7]

The most important modern density functional method was developed by Kohn and Sham [1] for which Kohn was awarded the Nobel prize in Chemistry in 1998. This, along with accurate approximations of the exchange-correlation functional provide the basis for all modern calculations done with Density Functional Theory (DFT).

There are many excellent references on DFT. Reference [8] provides a fairly detailed overview of DFT as well as descriptions of exchange-correlation functionals and approaches to solving numerical issues (density mixing, etc.). A thorough discussion of DFT would be quite lengthy, as such I will provide an overview of DFT with references to other resources that go in depth for the interested reader.

2.2 DFT Method

2.2.1 Hohenberg-Kohn Theorem

In quantum mechanics, there is no doubt that the ground state electronic density is determined by the external potential. One of the most important proofs for DFT is that this relationship can be inverted [9]. That is, given a ground state density the potential can be unambiguously recovered. To prove this we use two external, local potentials $V_1(\mathbf{r})$ and $V_2(\mathbf{r})$ which differ by more than a constant, and lead to different ground-state wavefunctions $|1\rangle$ and $|2\rangle$ which both have the same ground state density $n(\mathbf{r})$. (We will assume here that the ground state is non-degenerate. This restriction can be lifted, however.) The two potentials lead to different Hamiltonians $H_i = K + V_i + U$, with U being an interaction term. Since $|2\rangle$ is not the ground state of H_1, it follows that

$$E_1 = \langle 1|H_1|1\rangle < \langle 2|H_1|2\rangle. \tag{2.1}$$

We rewrite the last term as

$$\begin{aligned} \langle 2|H_1|2\rangle &= \langle 2|H_2|2\rangle + \langle 2|H_1 - H_2|2\rangle & (2.2)\\ &= E_2 + \langle 2|V_1 - V_2|2\rangle & (2.3)\\ &= E_2 + \int (V_1(\mathbf{r}) - V_2(\mathbf{r}))\, n(\mathbf{r})\, \mathrm{d}^3 r & (2.4) \end{aligned}$$

giving

$$E_1 < E_2 + \int (V_1(\mathbf{r}) - V_2(\mathbf{r}))\, n(\mathbf{r})\, \mathrm{d}^3 r. \tag{2.5}$$

There's nothing special about H_1 or H_2, so we can swap the labels 1 and 2 to give

$$E_2 < E_1 + \int (V_2(\mathbf{r}) - V_1(\mathbf{r}))\, n(\mathbf{r})\, \mathrm{d}^3 r, \tag{2.6}$$

and then adding (2.5) and (2.6) gives the contradiction $E_1 + E_2 < E_1 + E_2$. Thus there cannot be two different potentials which give rise to the same ground state density; the potential must be uniquely determined by $n(\mathbf{r})$ (to within a constant).

The Hohenberg-Kohn theorem presented here is very general. There is no assumption that the particles are Fermions, Bosons, identical particles, or non-interacting.

2.2.2 The Kohn-Sham Auxilliary System

The key idea in modern density functional theory is to replace the interacting problem with a much simpler noninteracting problem with the density as the basic variable. The Hohenberg-Kohn theorem rigorously proves that the density can be used as the basic variable in calculating properties of the system, but does not give a framework for doing so. The Kohn-Sham approach does so by constructing an auxillary system of noninteracting quasiparticles that have the same density as the true interacting problem.

We start by assuming that there exists a system of noninteracting electrons that has the same density as the interacting system. That is, there exists some single particle potential $v_s(\mathbf{r})$ which when applied to noninteracting electrons, yields the same ground state density as the fully interacting problem. This assumption is justified only empirically, in fact there are a few known examples for which a Kohn-Sham system does not exist. For systems of interest in condensed matter systems however, the Kohn-Sham system always exists.

The Hohenberg-Kohn theorem tells us that total energy for the interacting system can be written

$$E[n] = T[n] + V[n] + \int v_{\text{ext}}(\mathbf{r}) n(\mathbf{r})\, d^3r \tag{2.7}$$

where $T[n]$ is the interacting kinetic energy functional and $V[n]$ is the Coulomb potential functional for the interacting system, and $v_{\text{ext}}(\mathbf{r})$ is the external potential. (For clarity, the nuclear-nuclear interaction has been left out, but it is of course important to include in any practical application of the total energy. The Born-Oppenheimer approximation is used as well, so the nuclear kinetic energy operator is neglected.)

Since we have assumed the single particle system and the interacting system have the same density, we can add and subtract $T_s[n]$ (the noninteracting kinetic energy) and $E_H[n]$ (the Hartree energy) to (2.7), giving

$$E[n] = T_s[n] + E_H[n] + \{T[n] - T_s[n] + V[n] - E_H[n]\} + \int v_{\text{ext}}(\mathbf{r}) n(\mathbf{r})\, d^3r \quad (2.8)$$

$$E[n] = T_s[n] + E_H[n] + E_{xc}[n] + \int v_{\text{ext}}(\mathbf{r}) n(\mathbf{r})\, d^3r \quad (2.9)$$

where the exchange-correlation energy has been defined as

$$E_{xc}[n] = T[n] - T_s[n] + V[n] - E_H[n]. \quad (2.10)$$

Remarkably, $E_{xc}[n]$ is a universal functional; there is no dependence on the external potential. The kinetic energy difference $T[n] - T_s[n]$ is the kinetic contribution to correlation. The difference $V[n] - E_H[n]$ is made up of Hartree-Fock exchange and the electrostatic contribution to correlation. Since the exchange correlation potential contains all the important quantum many-body effects, the true exchange correlation functional is likely to be very complex, but in many cases it can be approximated reasonably well by simple functionals, discussed further in Sec. 2.3.

The Hartree energy $E_H[n]$ is the classical electrostatic energy for a charge distribution $n(\mathbf{r})$

$$E_H[n] = \frac{1}{2} \iint \frac{n(\mathbf{r}) n(\mathbf{r}')}{|\mathbf{r} - \mathbf{r}'|}\, d^3r\, d^3r', \quad (2.11)$$

the noninteracting kinetic energy T_s is evaluated from the single particle wavefunctions,

$$T_s[n] = \sum_i \frac{1}{2} \langle \psi[n] | p_i^2 | \psi[n] \rangle = -\sum_i \frac{1}{2} \int \psi_i^*(\mathbf{r}) \nabla^2 \psi_i(\mathbf{r})\, d^3r, \quad (2.12)$$

and the density $n(\mathbf{r})$ and particle count N of the noninteracting system are straightfor-

wardly calculated as

$$n(\mathbf{r}) = \sum_{i}^{\text{occ}} |\psi_i(\mathbf{r})|^2 \tag{2.13}$$

$$N = \int n(\mathbf{r})\, d^3r. \tag{2.14}$$

We can now construct a procedure for evaluating the total energy and the single particle wavefunctions. To build in the constraint on the total number of particles, we will introduce μ (the chemical potential) as a Lagrange multiplier. To enforce orthonormality of the wavefunctions we also introduce additional Lagrange multipliers ε_{ij}. The functional to be minimized is then $E - \mu N - \sum_{ij} \varepsilon_{ij}(\langle\psi_i|\psi_j\rangle - \delta_{ij})$ with respect to $\psi_i^*(\mathbf{r})$. This yields

$$\frac{\delta E - \mu N}{\delta \psi_i^*(\mathbf{r})} = \frac{\delta T_s[n]}{\delta \psi_i^*(\mathbf{r})} + v_s(\mathbf{r})\psi_i(\mathbf{r}) - \mu\psi_i(\mathbf{r}) - \sum_j \varepsilon_{ij}\psi_j(\mathbf{r}) = 0 \tag{2.15}$$

$$v_s(\mathbf{r}) = \int \frac{n(\mathbf{r}')}{|\mathbf{r} - \mathbf{r}'|}\, d^3r' + v_{xc}(\mathbf{r}) + v_{\text{ext}}(\mathbf{r}). \tag{2.16}$$

In any pratical application, one expands ψ_i in terms of a set of basis functions to give a matrix equation which can be diagonalized. Basis functions are discussed in further detail in Sec. 2.5.

The Kohn-Sham procedure is then as follows:

1. Guess an initial density.
2. Calculate Hamiltonian from (2.16) in the chosen basis, and diagonalize it to get the wavefunctions and band energies.
3. Fill states with N Fermionic particles to determine which states are occupied.
4. Construct a new density from the wavefunctions for occupied states.
5. Mix the input and output densities for numerical stability reasons.
6. If the density hasn't converged, go to step 2.

2.3 Exchange Correlation Approximations

There are a variety of approximations for the exchange-correlation functional. The most widely used ones in condensed matter physics are the local density approximation (LDA) and the generalized gradient approximation (GGA). All exchange correlation functionals calculate correlation as an enhancement over exchange,

$$E_{xc} = \int n(\mathbf{r}) v_x(\mathbf{r}) F_{xc}(...)\, d^3r \tag{2.17}$$

where F_{xc} is the enhancement and its parameters depend on whether the functional is LDA or GGA.

2.3.1 Local Density Approximation

LDA functionals are, as the name implies, all local functionals of the density, meaning that

$$E_{xc}^{\mathrm{LDA}}[n] = \int f(n(\mathbf{r}))\, d^3r. \tag{2.18}$$

Its spin-polarized generalization, the local spin density approximation (LSDA), satisfies

$$E_{xc}^{\mathrm{LSDA}}[n_\uparrow, n_\downarrow] = \int f(n_\uparrow(\mathbf{r}), n_\downarrow(\mathbf{r}))\, d^3r. \tag{2.19}$$

The LDA approximation is designed to be exact in the limit of a uniform electron gas, so to calculate the exchange contribution, one evaluates the Fock exchange integral

$$E_x[\psi] = -\frac{1}{2} \sum_\sigma \sum_{i,j \in occ} \iint \frac{\psi_{i\sigma}^*(\mathbf{r}) \psi_{j\sigma}^*(\mathbf{r}') \psi_{i\sigma}(\mathbf{r}') \psi_{j\sigma}(\mathbf{r})}{|\mathbf{r} - \mathbf{r}'|} \tag{2.20}$$

for a uniform electron gas with density n. Then one assumes that the contribution to the exchange-correlation integral (2.18) at a point $\mathbf{r}$ is that of a uniform gas with density $n(\mathbf{r})$.

This leads to the well known result

$$E_x^{\mathrm{LDA}} = \frac{3}{4\pi}\int \left(3\pi^2 n(\mathbf{r})\right)^{1/3} n(\mathbf{r})\, d^3r \tag{2.21}$$

$$\equiv \int \varepsilon_x(\mathbf{r}) n(\mathbf{r})\, d^3r \tag{2.22}$$

$$\varepsilon_x(\mathbf{r}) = \frac{3}{4}\left(\frac{3}{\pi}\right)^{1/3} n^{1/3}(\mathbf{r}) \tag{2.23}$$

The correlation contribution is generally fit as an enhancement of exchange, in the form

$$E_{xc} = \int n(\mathbf{r})\varepsilon_x(\mathbf{r}) F_{xc}(n(\mathbf{r}))\, d^3r \tag{2.24}$$

taken from Monte Carlo simulations of a free electron gas. Most of the modern functionals in use are fits based off Monte Carlo data published by Ceperley and Alder [10]. Commonly used LDA correlation functionals are Vosko-Wilk-Nusair [11], M. Teter-Pade [12], and Perdew-Zunger [3]. Since these fits are all based of the Ceperley-Alder data, there is not much more than minor variation between them.

2.3.2 Generalized Gradient Approximation

The next level of generalization of the exchange-correlation functional above LDA is to allow a dependency on the density gradients, so E_{xc} is then calculated via

$$E_{xc}^{\mathrm{GGA}}[n] = \int n(\mathbf{r})\varepsilon_x(\mathbf{r}) F_{xc}(n_\uparrow(\mathbf{r}), n_\downarrow(\mathbf{r}), |\nabla n_\uparrow|, |\nabla n_\downarrow|)\, d^3r. \tag{2.25}$$

In practice, it has been found that GGA functionals don't perform significantly better than LDA functionals in general. GGA usually leads to improvements in bond lengths and lattice constants, but in some cases it leads to worse results. Common GGA functionals are Perdew-Wang [13] and Perdew-Burke-Enzerhof (PBE) [2]. There exist several variations on PBE, such as revPBE [14] and PBEsol [15] which are obtained by changing some of the empirical parameters used in PBE.

2.4 Density Functional Perturbation Theory

Density functional perturbation theory (DFPT) [5] is a procedure developed for the calculation of response functions. It is closely related to the method of linear response [4]. A detailed description of the implementation of DFPT for phonons and electric field response is given in references [16] and [17], and is quite lengthy. Practical applications of DFPT have been used to calculate phonon frequencies and Born effective charges.

The general approach is to consider a perturbation to the external potential with the expansion

$$v_{\text{ext}} = v_{\text{ext}}^{(0)} + \lambda v_{\text{ext}}^{(1)} + \lambda^2 v_{\text{ext}}^{(2)} + \lambda^3 v_{\text{ext}}^{(3)} + \ldots, \tag{2.26}$$

then other perturbed quantities E, H, $\psi_{\mathbf{k}n}$, $n(\mathbf{r})$, etc. are similarly expanded. Generally the quantity of interest in applications of DFPT is the second order energy $E^{(2)}$, which corresponds to taking two derivatives of the energy with respect to an external parameter (or possibly two, if a second mixed partial of E is desired). This quantity is used in calculation of the dynamical matrix for phonon calculations, and the computation of Born effective charges. If one writes the density functional energy as

$$E[\psi] = \min_{\psi} \sum_{i \in occ} \langle \psi_i | T + V_{ext} | \psi_i \rangle + E_{\text{Hxc}}[n] \tag{2.27}$$

then the second order energy [4, 5, 16] is

$$\begin{aligned} E^{(2)} = \min_{\psi^{(1)}} \sum_{i \in occ} \Big[& \langle \psi_i^{(1)} | H^{(0)} - \varepsilon_i^{(0)} | \psi^{(1)} \rangle + \langle \psi_i^{(1)} | v_{\text{ext}}^{(1)} | \psi_i^{(0)} \rangle + \langle \psi_i^{(0)} | v_{\text{ext}}^{(1)} | \psi^{(1)} \rangle \\ & + \langle \psi_i^{(0)} | v_{\text{ext}}^{(2)} | \psi_i^{(0)} \rangle \Big] + \frac{1}{2} \iint \left. \frac{\delta^2 E_{Hxc}}{\delta n(\mathbf{r}) \delta n(\mathbf{r}')} \right|_{n^{(0)}} n^{(1)}(\mathbf{r}) n^{(1)}(\mathbf{r}') \, d^3r \, d^3r' \\ & + \int \frac{d}{d\lambda} \left. \frac{\delta E_{Hxc}}{\delta n(\mathbf{r})} \right|_{n^{(0)}} n^{(1)}(\mathbf{r}) \, d^3r \frac{1}{2} \left. \frac{d^2 E_{Hxc}}{d\lambda^2} \right|_{n^{(0)}} \end{aligned} \tag{2.28}$$

with the constraint that the first order wavefunctions are orthogonal to the ground state

wavefunctions,

$$\langle \psi_i^{(0)} | \psi_j^{(1)} \rangle = 0. \tag{2.29}$$

The second order energy is variational with respect to the first order wavefunctions. Since only the first order wavefunctions are needed to compute second derivatives of the energy, one can compute second mixed partials of the energy with respect to different perturbations using the wavefunction response to only one of the perturbations. This approach can be used to calculate, eg. Born effective charges, where the second mixed partial of total energy with respect to an electric field and atomic displacement is needed.

2.4.1 Phonons

For computation of phonons aside from the Γ point, one must consider the effect of non-commensurate perturbations characterized by a wavevector $\mathbf{q}$ in the first Brillouin zone. In this case, the ground state potential is periodic,

$$v_{\text{ext}}^{(0)}(\mathbf{r} + \mathbf{R}) = v_{\text{ext}}^{(0)}(\mathbf{r}), \tag{2.30}$$

and the first order potential will satisfy

$$v_{\text{ext},\mathbf{q}}^{(1)}(\mathbf{r} + \mathbf{R}) = e^{i\mathbf{q}\cdot\mathbf{R}}\, v_{\text{ext},\mathbf{q}}^{(1)}(\mathbf{r}). \tag{2.31}$$

This perturbation is non-Hermitian, so one must also consider the same perturbation with wavevector $-\mathbf{q}$. However, the response to the sum of perturbations will be just the sum of the responses to the individual perturbation, so we can consider the non-Hermitian operator for simplicity in this discussion. The first order responses in the wavefunction and density satisfy

$$\psi_{i,\mathbf{k},\mathbf{q}}^{(1)}(\mathbf{r} + \mathbf{R}) = e^{i(\mathbf{k}+\mathbf{q})\cdot\mathbf{R}}\, \psi_{i,\mathbf{k},\mathbf{q}}^{(1)}(\mathbf{r}) \tag{2.32}$$

$$n_{\mathbf{q}}^{(1)}(\mathbf{r} + \mathbf{R}) = e^{i\mathbf{q}\cdot\mathbf{R}}\, n_{\mathbf{q}}^{(1)}(\mathbf{r}). \tag{2.33}$$

The perturbing potential for a collective atomic displacement where the κ-th atom located at $\mathbf{s}_\kappa$ is moved in the direction α will be given by

$$v^{(1)}_{\mathrm{ext},\mathbf{q}}(\mathbf{r}) = \sum_j e^{i\mathbf{q}\cdot\mathbf{R}_j} \frac{\partial}{\partial \tau_{\kappa,\alpha}} v_\kappa(\mathbf{r}-\mathbf{R}_j) \tag{2.34}$$

$$v^{(2)}_{\mathrm{ext},\mathbf{q}}(\mathbf{r}) = \sum_j \frac{1}{2} \frac{\partial^2}{\partial^2 \tau_{\kappa,\alpha}} v_\kappa(\mathbf{r}-\mathbf{R}_j) \tag{2.35}$$

where v_κ is the potential from the atom being perturbed.

The calculation of phonon spectrum procedes as follows. First, for each atom in the unit cell, one computes the dynamical matrix

$$D_{\kappa i,\kappa' j}(\mathbf{R}) = \frac{\partial^2 E}{\partial s_{\mathbf{R}\kappa i} \partial s_{\mathbf{0}\kappa' j}} \tag{2.36}$$

by computing the response to atomic displacements for each atom in each direction. Then the Fourier transformed dynamical matrix when diagonalized in the generalized eigenvalue problem

$$D(\mathbf{q})\mathbf{s} = M\omega^2_{\mathbf{q}}\,\mathbf{s} \tag{2.37}$$

yields the phonon frequencies at pseudomomentum vector $\mathbf{q}$. Here, M is a matrix with the atomic masses on the diagonal, and the resulting eigenvalues $\omega^2_{\mathbf{q}}$ are actually the squares of the phonon frequencies.

2.5 Basis Sets

In practice, an application of DFT requires that the Kohn-Sham eigenstates are expanded in some finite basis set. The discussion up to this point in this chapter on DFT has been general; there have been no boundary conditions assumed. In this section we will discuss basis sets which are useful mainly for solids, so periodic boundary conditions will be assumed.

There are a large variety of basis sets; a partial list of the most widely used ones would

include planewaves (PW), local orbitals (LO), linearized augmented planewaves (LAPW), linearized muffin-tin orbitals (LMTO). In this section, I will discuss the two basis sets that have been used most extensively in this research, which are PW and LO.

2.5.1 Planewaves

A basis set composed entirely of planewaves has the convenient property that with appropriate selection of planewaves, the basis automatically fulfills the periodicity condition of a crystalline solid. The Kohn-Sham eigenstate $\psi_{n\mathbf{k}}$ is expanded in planewaves as

$$\langle \mathbf{r}|\psi_{n\mathbf{k}}\rangle = \sum_{\mathbf{G}} c_{n,\mathbf{k}+\mathbf{G}}\, e^{i(\mathbf{k}+\mathbf{G})\cdot\mathbf{r}} = e^{i\mathbf{k}\cdot\mathbf{r}} u_{\mathbf{k}}(\mathbf{r}) \tag{2.38}$$

where $\mathbf{r}$ is a real-space vector, and $\mathbf{G} = \sum_i n_i \mathbf{b}_i$ where n_i are integers and the b_i are the reciprocal lattice vectors. The satisfaction of the Bloch condition is explicit; the function $u_{\mathbf{k}}(\mathbf{r})$ has the periodicity of the unit cell as it is composed of planewaves with wavevectors that are integer multiples of the reciprocal lattice vectors.

For a practical implementation, the basis set needs to be cut off somewhere to contain a finite number of planewaves. This is generally done with a single parameter E_{cut} which is taken as the maximum kinetic energy of any planewave used in the expansion. This results in the condition that planewaves are kept in the basis set expansion if they satisfy the condition

$$\frac{1}{2}(\mathbf{k}+\mathbf{G})^2 \leq E_{\text{cut}} \tag{2.39}$$

Loosely speaking, this condition represents a sphere in reciprocal space inside which points representing planewave vectors which satisfy the Bloch condition are kept in the basis expansion, and planewaves with very high kinetic energy that fall outside the sphere are discarded.

In practice, a planewave expansion is not practical to use for the basic solid problem where the atomic cores have potential $-Z/r$ and all electrons are treated on the same

footing. The difficulty with the planewave basis is caused by two factors. The first complication is the treatment of highly localized core electrons. The wavefunctions for these electrons is very rapidly varying in the region near the atomic cores, and rapidly goes to zero away from the nucleus. Expanding this type of wavefunction would require a extremely large set of planewaves with extremely large kinetic energy to accurately represent these core electrons. Such a large basis set would end up being completely unwieldy computationally, and rather unnecessary as the core electrons do not play a role in many of properties of interest in solids.

The second complication for planewaves can come in expanding the core region of the valence wavefunctions, for electrons with a high principle quantum number. This is because states with different quantum numbers must be orthogonal. For electrons with the same angular momentum quantum numbers l and m_l values but principle quantum numbers n, the orthogonality cannot be taken care of by the angular part, so the radial functions must have a different number of nodes to be orthogonal. As a general rule, for hydrogenic wave functions the number of nodes in the radial wavefunction is $n-l-1$, so electrons with higher n will have extra nodes. These nodes always occur near the atomic cores in solids. Correctly capturing these nodes in a planewave basis would require a very large basis set.

The solution that is always used in planewave basis sets is to replace the atomic potential with a pseudopotential. There are a large variety of methods for generating pseudopotentials, but all of the results presented in this dissertation using planewaves were done with norm-conserving Troullier-Martins pseudopotentials [18]. These pseudopotentials are non-local [19], and can optionally include a nonlinear core correction [20]. A non-local pseudopotential contains different potentials for different orbital angular momentum values, and can be written

$$V = \sum_{lm} |lm\rangle V_l \langle lm|. \tag{2.40}$$

The basic approach to generating a Troullier-Martins pseudopotential is this. One

chooses which valence states should be used to generate the nonlocal potentials, and a core-radius for each is chosen. Outside this radius, the pseudopotential is exactly the atomic potential $-Z/r$, with Z equal to the number of valence electrons. Inside this radius the pseudopotential becomes a smooth function which is not divergent at $r = 0$. A detailed discussion of generating pseudopotentials, as well as pseudopotentials for all elements up to Pu can be found in Reference [21].

2.5.2 Local Orbitals (FPLO)

Of all the common basis sets, planewaves could be (loosely) thought of as being the 'delocalized extreme,' where each basis function is completely delocalized. The opposite extreme would be a basis set composed entirely of localized, atomic-like orbitals. This is what is implemented in the Full Potential Local Orbital (FPLO) code. [22]

The basis functions are computed by solving an atomic like problem with potential

$$v_{\mathrm{at}}(r) = -\frac{1}{4\pi}\int v(\mathbf{r}-\mathbf{R}-\mathbf{s})d\Omega + \left(\frac{r}{r_0}\right)^m. \tag{2.41}$$

The first term in (2.41) is the spherical average of the crystal potential, and the second term is the confining potential, with a typical value of m of 4. r_0 is a compression parameter which is recast in terms of a dimensionless parameter x_0 such that $r_0 = (x_0 r_{NN}/2)^{3/2}$ with r_{NN} the nearest neighbor distance, and then x_0 is then taken as a variational parameter in the self-consistent procedure. The basis functions that are used in the first step of the calculation are computed just from the atomic potential $v_{\mathrm{at}}(r) = -Z/r$, but after the density is computed in each DFT step, the basis functions are recalculated based on the new crystal potential.

It is important to note that although the atomic orbitals are orthogonal, the basis functions used in the crystal are not. The overlap matrix has form

$$S_{ij}^{(\mathbf{k})} = \delta_{ij} + \sum_{\mathbf{R}} \langle \mathbf{R}i|\mathbf{0}j\rangle e^{i\mathbf{k}\cdot(\mathbf{R}+\mathbf{s}_i-\mathbf{s}_j)} \tag{2.42}$$

where $\mathbf{s}_i$ locates the i-th atom in the unit cell, and $\mathbf{R}$ is a Bravais lattice vector, so that the vector $\mathbf{R} + \mathbf{s}_i - \mathbf{s}_j$ goes between the i-th atom in the unit cell at the origin and the j-th atom in the unit cell located at $\mathbf{R}$. The overlap matrix is not the identity matrix because the tail of a basis function on one atom overlaps the tail of basis functions on other atoms. This changes the secular equation, requiring that a generalized eigenvalue problem be solved,

$$|\mathbf{k}n\rangle = \sum_j c_{j\mathbf{k}n} \sum_{\mathbf{R}} N_{\mathbf{R}}^{-1/2} e^{i\mathbf{k}\cdot\mathbf{R}} |\mathbf{R}j\rangle \tag{2.43}$$

$$\sum_{j'} \left[H_{jj'}^{(\mathbf{k})} - \varepsilon_{\mathbf{k}n} S_{jj'}^{(\mathbf{k})} \right] c_{j'\mathbf{k}n} = 0 \tag{2.44}$$

where $|\mathbf{k}n\rangle$ is the wavefunction and $c_{j\mathbf{k}n}$ is the coefficient in the basis expansion. The second summation in (2.43) ensures that $|\mathbf{k}n\rangle$ satisfies the Bloch theorem.

2.6 Wannier Functions

The use of Bloch waves as solutions in a crystalline solid allows us identify the pseudo-momentum $\mathbf{k}$ as a good quantum number (or three, rather), and to block diagonalize the full Hamiltonian so that there is only a series of $\mathbf{k}$-dependent Hamiltonians. Visualization of these wavefunctions is nontrivial however, because (1) Bloch waves are completely delocalized and (2) they are $\mathbf{k}$-dependent, so there is a very large number of different wavefunctions to visualize, even for a single band.

A solution to both these problems is available by constructing of Wannier functions. Wannier functions are essentially a Fourier transform of the wavefunctions labeled by $\mathbf{k}$ to basis functions which exist at each site in the lattice. Additionally, the Wannier functions are independent of $\mathbf{R}$, so that the same Wannier functions sit at every lattice site. In this way, one needs to visualize no more than one Wannier function per electronic band of interest. Wannier functionals also incorporate the effects of bonding that occur in the crystal, so for this reason they are sometimes colloquially referred to as 'molecular orbitals

of solids.'

The construction of Wannier functions is as follows. The m-th Wannier function located at site $\mathbf{R}$, designated as $|\mathbf{R}m\rangle$ is given by

$$|\mathbf{R}m\rangle = N_{\mathbf{k}}^{-1/2} \sum_{\mathbf{k}} U_{mn}^{\mathbf{k}} e^{-i\mathbf{k}\cdot\mathbf{R}} |\mathbf{k}n\rangle \tag{2.45}$$

where $U^{\mathbf{k}}$ is a unitary matrix. $U^{\mathbf{k}}$ need not be a square matrix actually, this procedure can be applied by projecting out M Wannier functions from N bands where $M \leq N$. In this case, the rows of $U^{\mathbf{k}}$ must represent a set of orthogonal vectors.

The appearance of $U^{\mathbf{k}}$ in (2.45) allows a gauge freedom in this transformation. In practice, the wavefunctions $|\mathbf{k}n\rangle$ come from diagonalizing the Hamiltonian matrix in some basis, and of course any eigenvector returned by a numerical diagonalization routine may come with an attached phase factor $e^{i\alpha}$. Numerical diagonalization routines don't generally make any guarantees about what phase factors are attached to the eigenvectors, so it may not even be consistent or continuous at different $\mathbf{k}$-points. The inclusion of $U^{\mathbf{k}}$ in the sum (2.45) allows one to normalize the phase factors for each wavefunction included in the sum so that the wavefunctions constructively interfere near the desired site, and destructively interfere away from the site so that the Wannier function is localized. There are a few different approaches to choosing the $U^{\mathbf{k}}$ matrices, such as Maximally Localized Wannier Functions [23, 24], or by using projections onto local orbitals. [25, 26]

The existence of the gauge freedom allows for a certain degree of arbitrariness in the resultant Wannier functions. It is generally desirable to have Wannier functions that are both localized and real, which greatly cuts down on the gauge freedom. It seems that in every example considered in the literature both these properties come together, however there is no general proof that this is true in three dimensions or with multiple entangled bands. Such a proof is only known for a single band in one dimension. [27]

2.7 Tight Binding

The tight binding model allows one to construct wavefunctions for a periodic crystal from localized atomic orbitals. It is sometimes called linear combination of atomic orbitals (LCAO). Since the tight binding approach is detailed in many introductory solid-state physics texts [8, 28, 29], I will only present a brief overview of tight-binding here as it applies to the applications discussed in chapters 6 and 9.

The goal of the tight binding approach is to construct a representation of the Hamiltonian and its wavefunctions in a basis of localized atomic orbitals $|\mathbf{R}b\rangle$, which represents the b-th atomic orbital at site $\mathbf{R}$. The real space projection is $\langle\mathbf{r}|\mathbf{R}b\rangle = \phi_b(\mathbf{r}-\mathbf{R})$ where $\phi_b(\mathbf{r})$ is the real space atomic orbital. Henceforth we shall assume that the on-site orbitals are orthogonal, $\langle\mathbf{R}b|\mathbf{R}b'\rangle = \delta_{bb'}$.

The first thing to do is construct basis states that satisfy the Bloch condition, by defining

$$|\mathbf{k}b\rangle = N^{-1/2}\sum_{\mathbf{R}} e^{i\mathbf{k}\cdot\mathbf{R}}|\mathbf{R}b\rangle. \tag{2.46}$$

Then the Hamiltonian can be calculated via the overlap

$$H^{\mathbf{k}}_{b,b'} \equiv \langle\mathbf{k}b|H|\mathbf{k}b'\rangle = \varepsilon_b\,\delta_{b,b'} + \sum_{\mathbf{R}\neq\mathbf{0}} t_{b,b'}(\mathbf{R})e^{i\mathbf{k}\cdot\mathbf{R}} \tag{2.47}$$

where ε_b is the on-site energy $\langle\mathbf{0}b|H|\mathbf{0}b\rangle$ and $t_{b,b'}(\mathbf{R}) = \langle\mathbf{0}b|H|\mathbf{R}b'\rangle$ is the tight binding coefficient, often interpreted as the amplitude for hopping from an orbital b at the origin to an orbital b' at a distance $\mathbf{R}$.

This basis has not been constructed in a manner that implies orthogonality. The atomic orbitals used in the basis are not (necessarily) orthogonal to orbitals residing on different sites. Thus, it is necessary to calculate the overlap matrix

$$S^{\mathbf{k}}_{b,b'} \equiv \langle\mathbf{k}b|\mathbf{k}\mathbf{b}'\rangle = \delta_{b,b'} + \sum_{\mathbf{R}\neq\mathbf{0}} s_{b,b'}(\mathbf{R})e^{i\mathbf{k}\cdot\mathbf{R}} \tag{2.48}$$

where $s_{b,b'}(\mathbf{R}) = \langle \mathbf{0}b|\mathbf{R}b'\rangle$ is the overlap integral between orbital b on the site at the origin with another orbital b' at a site $\mathbf{R}$.

The appearance of a non-identity overlap matrix necessitates that the secular equation to be solved takes the form of a generalized eigenvalue problem,

$$H^{\mathbf{k}}|\mathbf{k}n\rangle = \varepsilon_{\mathbf{k}n} S^{\mathbf{k}}|\mathbf{k}n\rangle. \tag{2.49}$$

If one chooses Wannier functions as defined in section 2.6 for the atomic orbitals, then the overlap matrix (2.48) becomes the identity matrix and one can solve the regular eigenvalue problem.

What is often done in tight-binding fits is to take a bandstructure $\varepsilon_{\mathbf{k}n}$ from an LDA calculation and treat the tight-binding parameters ε_b and $t_{b,b'}(\mathbf{R})$ as fitting parameters, along with the assumption that the local orbitals are Wannier functions so that the overlap matrix is the identity matrix. This works well for systems with an isolated set of bands without large bandwidths. In this case it is generally expected that one does not need many parameters to get a good fit to the DFT band structure. The tight binding parameters can then be used in model Hamiltonian calculations for more sophisticated many-body methods. For more detailed examples of tight-binding fits, see chapters 6 and 9.

Chapter 3

LSDA+U

The work described in this chapter was done in collaboration with Warren E. Pickett and Klaus Koepernik.

3.1 Introduction

Density functional theory (DFT) and its associated local (spin) density approximation [L(S)DA] is used widely to describe the properties of a wide variety of materials, often with great success. However there exists a class of materials which are poorly described, sometimes qualitatively, by LDA. These so-called strongly correlated materials typically contain atoms with open d or f shells, in which the corresponding orbitals are in some sense localized. The LSDA+U approach was introduced by Anisimov, Zaanen, and Andersen[30] to treat correlated materials as a modification of LDA ('on top of LDA') that adds an intra-atomic Hubbard U repulsion term in the energy functional. Treated in a self-consistent mean field ('Hartree-Fock') manner, in quite a large number of cases the LDA+U result provides a greatly improved description of strongly correlated materials.

At the most basic level, the LSDA+U correction tends to drive the correlated orbital m occupation numbers $n_{m\sigma}$ (σ denotes spin projection) to integer values 0 or 1. This in turn produces, under appropriate conditions, insulating states out of conducting LSDA

states, and the Mott insulating state of several systems is regarded as being well described by LSDA+U at the band theory level. Dudarev *et al.*[31] and Petukhov *et al.*[32] provided some description of the effect of the spin dependence of two different double counting terms within an isotropic approximation. Beyond this important but simple effect, there is freedom in which of the spin-orbitals ($m\sigma$) will be occupied, which can affect the result considerably and therefore makes it important to understand the effects of anisotropy and spin polarization in LSDA+U. After the successes of providing realistic pictures of the Mott insulating state in La_2CuO_4 and the transition metal monoxides,[30] the anisotropy contained in the LSDA+U method produced the correct orbitally ordered magnetic arrangement for $KCuF_3$ that provided an understanding of its magnetic behavior.[33]

The anisotropy of the interaction, and its connection to the level of spin polarization, is a topic that is gaining interest and importance. One example is in the LSDA+U description of the zero temperature Mott transition under pressure in the classic Mott insulator MnO. The first transition under pressure is predicted to be[34] an insulator-insulator (not insulator-metal) transition, with a $S = \frac{5}{2} \rightarrow S = \frac{1}{2}$ moment collapse and a volume collapse. The insulator-to-insulator aspect is surprising, but more surprising is the form of moment collapse: each orbital remains singly occupied beyond the transition, but the spins of electrons in two of the orbitals have flipped direction. This type of moment collapse is totally unanticipated (and hence disbelieved by some), but it is robust against crystal structure (occurring in both rocksalt and NiAs structures) and against reasonable variation of the interaction strength. Detailed analysis indicates it is a product of the anisotropy of the LSDA+U interaction and the symmetry lowering due to antiferromagnetic order.

Another unanticipated result was obtained[35] in $LaNiO_2$, which is a metal experimentally. This compound is also a metal in LSDA+U over a very large range of interaction strength U, rather than reverting to a Mott insulating Ni^{1+} system which would be isovalent with $CaCuO_2$. For values of U in the range expected to be appropriate for the Ni ion in this oxide, the magnetic system consists of an atomic singlet consisting of antialigned $d_{x^2-y^2}$ and d_{z^2} spins on each Ni ion. Again the anisotropy of the interaction

evidently plays a crucial role in the result, with its effect being coupled thoroughly with band mixing effects.

The addition of a Hubbard U interaction also introduces the need for "double counting" correction terms in the energy functional, to account for the fact that the Coulomb energy is already included (albeit more approximately) in the LSDA functional. All double counting schemes subtract an averaged energy for the occupation of a selected reference state depending only on $\{N_\sigma\}$, which largely cancels the isotropic interaction of the E_I term Eq. (3.2). Several forms for these double-counting terms have been proposed,[30, 36, 37] but primarily two are commonly used. These LDA+U functionals are most often referred to as around mean field (AMF) and the fully localized limit (FLL), which is also referred to as the atomic limit (AL). The distinctions between these forms have attracted some discussion, but without consideration of the full anisotropy of the interaction.

The need for double-counting corrections is not unique to the LDA+U method; any other method that adds correlation terms to the LSDA functional, such as the dynamical LDA+DMFT (dynamical mean field theory) approach, also will require double-counting corrections. This is an unfortunate consequence of LDA's success; LDA works too well, even in correlated systems where it usually gets interatomic charge balance reasonably, to just throw it away.[1] The common approach has been to use LSDA for correlated materials and include a double-counting correction. There are techniques being developed which do not build on a correction to DFT-LDA, but it remains to be seen whether these approaches will be successfully applied to a broad range of solid-state materials.

Although there has been much study on the performance of these LDA+U functionals in the context of real materials, and an early review of the method and some applications was provided by Anisimov, Aryasetiawan, and Lichtenstein,[38] relatively little has been done to understand, qualitatively and semi-quantitatively, how the functionals operate based solely on their energetics, distinct from DFT-LSDA effects. In this paper we analyze

[1]There are numerous examples for strongly correlated (*heavy fermion*) metals where the Fermi surface calculated within LDA is predicted as well as for more conventional metals. This surely requires that the charge balance between the various atoms is accurate.

the functionals that are commonly used, as well as others which were introduced early on but are not so commonly used. Some of the nomenclature in the literature is confusing, so we try to clarify these confusions where we can.

LDA+U Functional	E_{dc}	=	E_{dc} (rewritten)	DFT XC Functional
Fl-nS	$\frac{1}{2}UN^2 - \frac{U+2lJ}{2l+1}\frac{1}{4}N^2$	=	$\frac{1}{2}UN^2 - \frac{U+2lJ}{2l+1}\frac{1}{2}\sum_\sigma(\frac{N}{2})^2$	LDA
Fl-S (AMF)	$\frac{1}{2}UN^2 - \frac{U+2lJ}{2l+1}\frac{1}{2}\sum_\sigma N_\sigma^2$	=	$\frac{1}{2}UN^2 - \frac{U+2lJ}{2l+1}\frac{1}{2}\sum_\sigma N_\sigma^2$	LSDA
FLL	$\frac{1}{2}UN(N-1) - \frac{1}{2}J\sum_\sigma N_\sigma(N_\sigma-1)$	=	$\frac{1}{2}UN(N-1) - \frac{1}{2}J\sum_\sigma(N_\sigma^2 - N_\sigma)$	LSDA
FLL-nS	$\frac{1}{2}UN(N-1) - \frac{1}{4}JN(N-2)$	=	$\frac{1}{2}UN(N-1) - \frac{1}{2}J\sum_\sigma((\frac{N}{2})^2 - N_\sigma)$	LDA

Table 3.1: The double-counting terms of various LDA+U functionals. In the second expression two of them are rewritten to reflect how they are (somewhat deceptively) identical in form, but in one case a distinction between spin-up and spin-down (relative to half of N: $N_\sigma \leftrightarrow N/2$) is made. Note that while the first two forms appear to contain an isotropic self-interaction [$\frac{1}{2}UN^2$ rather than $\frac{1}{2}N(N-1)$] they are derived from a form which *explicitly* has *no* self-interaction between the orbital fluctuations $\delta_{M\sigma}$. See text for more discussion.

3.2 The LSDA+U Correction ΔE

The LDA+U functional is usually coded in a form in which the choice of coordinate system is irrelevant, often referred to as the rotationally-invariant form.[33] This form involves Coulomb matrix elements that have four orbital indices, and the orbital occupation numbers are matrices in orbital space (*viz.* $n_{mm'}$). One can always (after the fact) rotate into the orbital Hilbert space in which the occupations are diagonal, in which case the interactions have only two indices. In our discussion we will work in the diagonal representation.

The LDA+U functionals considered here can all be written in the form

$$\Delta E = E_I - E_{dc}, \tag{3.1}$$

where the direct interaction is

$$E_I = \frac{1}{2} \sum_{m\sigma \neq m'\sigma'} W^{\sigma\sigma'}_{mm'} n_{m\sigma} n_{m'\sigma'} \tag{3.2}$$

and E_{dc} is the double-counting correction. The Coulomb matrix elements are given in terms of the direct and (spin-dependent) exchange contributions as

$$W^{\sigma\sigma'}_{mm'} = (U_{mm'} - J_{mm'}\delta_{\sigma,\sigma'}). \tag{3.3}$$

By the convention chosen here, E_I and E_{dc} are both positive quantities as long as the constants U and J (which define the matrix elements $U_{mm'}$ and $J_{mm'}$ but are not the same) as chosen conventionally, with U much larger than J.

Note that the orbital+spin diagonal term has been omitted in Eq. 3.2 – there is no self-interaction in E_I. However, it is formally allowed to include the diagonal 'self-interaction' term, because the matrix element vanishes identically (self-interaction equals self-exchange: $U_{mm} = J_{mm}$), and it can simplify expressions (sometimes at a cost in clarity) if this is done. The double counting correction depends only on the orbital sum

N_σ, which appears up to quadratic order. A consequence is that it will contain terms in $n_{m\sigma}n_{m\sigma}$, which are self-interactions. Thus while the LSDA+U method was not intended as a self-interaction correction method, it is not totally self-interaction free. In fact, the underlying LSDA method also contains self-interaction, and the double-counting term may serve to compensate somewhat this unwanted effect. We discuss self-interaction at selected points in this paper.

3.2.1 Short formal background to the LSDA+U method.

The "LSDA+U method" is actually a class of functionals. Each functional has the same form of interaction E_I, with differences specified by

(1) choice of the form of double counting term.

(2) choice of constants U and J. For a given functional, these are 'universal' constants like $\hbar, m, e$, i.e. they are not functional of the density in current implementations. Possibilities for doing so, that is, determining them self-consistently within the theory, have been proposed.[39]

(3) choice of projection method to determine the occupation matrices from the Kohn-Sham orbitals. Given identical choices for (1) and (2) above, there will be some (typically small) differences in results from different codes due to the projection method.

The occupation numbers (or, more generally, matrices) are functionals of the density, $n_{m\sigma}[\rho]$, through their dependence on the Kohn-Sham orbitals. Then, whereas in LSDA one uses the functional derivative

$$\text{LSDA}: \quad \frac{\partial E_{LSDA}[\{\rho_s\}]}{\partial \rho_\sigma(r)} \tag{3.4}$$

in minimizing the functional, in LSDA+U the expression generalizes to

$$\text{LSDA + U}: \quad \frac{\partial (E_{LSDA}[\{\rho_s\}] + \Delta E[\{n_{ms}[\rho_s]\}])}{\partial \rho_\sigma(r)} \tag{3.5}$$

Since the resulting spin densities ρ_s are changed by including the ΔE correction, the change in energy involves not only ΔE but also the change in E_{LSDA}. In practice, there is no reason to compare E_{LSDA+U} with E_{LSDA} as they are such different functionals. However, in the following we will be assessing the importance of the choice of the double counting term in the LSDA+U functional, and it is of interest to compare, for fixed U and J, the energy differences between LSDA+U functionals differing only in their double counting terms in order to understand the differing results. Even if the set of occupation numbers turn out to be the same (a situation we consider below), the densities ρ_σ will be different and the differences in E_{LSDA} may become important.

As with the non-kinetic energy terms in E_{LSDA}, the functional derivatives of ΔE lead to potentials in the Kohn-Sham equation. These are non-local potentials, which (via the same projection used to define the occupation numbers) give rise to orbital-dependent (nonlocal) potentials

$$\begin{aligned} v_{m\sigma} &\equiv \frac{\partial \Delta E}{\partial n_{m\sigma}} = v^I_{m\sigma} - v^{dc}_{m\sigma}, \\ v^I_{m\sigma} &= \sum_{m'\sigma' \neq m\sigma} W^{\sigma\sigma'}_{mm'} n_{m'\sigma'}. \end{aligned} \tag{3.6}$$

The double counting orbital potential is discussed later.

The corresponding contribution to the eigenvalue sum E_{sum} is

$$\Delta E_{sum} = \sum_{m\sigma} v_{m\sigma} n_{m\sigma}, \tag{3.7}$$

which is subtracted from the eigenvalue sum to obtain the Kohn-Sham kinetic energy. However, there are indirect effects of the orbital potentials that affect all of the kinetic and (LSDA) potential energies; these will be different for different ΔE functionals because the orbital potentials, which depend on the derivative of ΔE and not simply on the values of $n_{m\sigma}$, differ for each functional. This makes it necessary, for understanding the effects of the ΔE correction and the change in energy, to analyze the orbital potentials. We provide

a brief discussion in Sec. V.

3.2.2 Fluctuation forms of LSDA+U

First we consider the class of functionals that can be written in what is termed here as a *fluctuation form*. The original LDA+U functional was introduced in 1991 by Anisimov, Zaanen and Andersen[30] and was written as

$$\Delta E^{Fl-nS} = \frac{1}{2} \sum_{m\sigma \neq m'\sigma'} W^{\sigma\sigma'}_{mm'} (n_{m\sigma} - \bar{n})(n_{m'\sigma'} - \bar{n}), \tag{3.8}$$

where $\bar{n} = N^{\rm corr}/2(2l+1)$ is the average occupation of the correlated orbitals. (Henceforth $N \equiv N^{\rm corr}$.) Note that the energy is changed only according to *angular 'fluctuation'* away from the (spin-independent) angular average occupation. This form is properly used with LDA (the 'LDA averages' $\bar{n}$ are the reference) and not LSDA. This form was originally advocated with generic $(U - J\delta_{\sigma,\sigma'})$ matrix elements instead of the full Coulomb matrix, but we use the full $W^{\sigma\sigma'}_{mm'}$ here for comparison with other functionals.

In 1994, Czyzyk and Sawatzky[37] introduced a change to (3.8) and also proposed a new functional. The motivation for changing (3.8) was to use an LSDA exchange-correlation functional to treat spin splitting effects rather than LDA. This change motivated the following equation,

$$\begin{aligned} \Delta E^{Fl-S} &= \frac{1}{2} \sum_{m\sigma \neq m'\sigma'} W^{\sigma\sigma'}_{mm} (n_{m\sigma} - \bar{n}_{\sigma})(n_{m'\sigma'} - \bar{n}_{\sigma'}) \\ &= \Delta E^{AMF} \end{aligned} \tag{3.9}$$

where $\bar{n}_\sigma = N_\sigma/(2l+1)$ is the average occupation of a single spin of the correlated orbitals. Here the energy correction is due to *angular fluctuations* away from the spin-dependent angular mean, and hence must be used with LSDA. We point out that the authors in Ref. [[37]] refer to Eq. (3.8) as $E^{\rm LDA+AMF}$ and Eq. (3.9) as $E^{\rm LSDA+AMF}$. This wording may have caused subsequent confusion, due to the way these terms have come to be used, and

also because a discussion of the "+U" functionals requires explicit specification of whether LDA or LSDA is being used just to understand which functional is being discussed. Also confusing is that Solovyev, Dederichs, and Anisimov[40] rejustified Eq. 3.8 using "atomic limit" terminology.

The fluctuation forms of LSDA+U are automatically particle-hole symmetric, since $n_{m\sigma} \to 1 - n_{m\sigma}$, $\bar{n}_\sigma \to 1 - \bar{n}$ gives $n_{m\sigma} - \bar{n}_\sigma \to -(n_{m\sigma} - \bar{n}_\sigma)$ and the expression is quadratic in these fluctuations. The general form of Eq. 3.1 need not be particle-hole symmetric.

Many authors (present authors included) have used the term LDA+U where the term LSDA+U would be more appropriate, which is especially confusing when discussing the AMF functional. We choose to depart from this confusing nomenclature by giving (3.8) and (3.9) unique names specifying their fluctuation forms, and their connection to LSDA (Fl-S) or to LDA (Fl-nS). We collect the double-counting terms for the various functionals, along with their connection to LDA or LSDA, in Table I.

3.2.3 The Fully Localized Limit (FLL) Functional

The second functional introduced by Czyzyk and Sawatzky[37] is the FLL functional. (A J=0 version of FLL was introduced in 1993 by Anisimov *et al.*[36]) The authors referred to it (confusingly, as terminology has progressed) as the "around mean field" functional but the atomic limit double counting term. This double-couting term can be obtained by considering the energy of an isolated atomic shell with N electrons, so in the literature it is commonly referred to as the atomic limit, or fully localized limit (FLL) functional. This functional cannot be written in the fluctuation form of the previous two functionals (the fluctuation form is exhausted by the -S and -nS cases). The FLL functional is written in the form of (3.1), with the double-counting term given in Table 3.1.

There is yet another LDA+U functional that is available, which was introduced in 1993 by Anisimov *et al.* [36] There is no clear name for it, but since it can be obtained by using $N_\sigma = N/2$ in E_{dc} for FLL, one might consistently refer to it as FLL-nS, corresponding to

FLL with no spin dependence. The authors in Ref. [36] indicate that this functional is to be used with LDA, in accordance with the lack of spin dependence in the double counting term.

3.2.4 Implementation of LSDA+U in Some Widely Used Codes

The Fl-nS functional is implemented in the WIEN2K code, as $nldau = 2$, and called HMF (Hubbard in Mean Field),[41] however it is apparently not often used.
The Fl-S (AMF) functional is implemented in the WIEN2K code[41] as $nldau = 0$ and the FPLO code[22] as AMF.
The FLL functional is implemented in several general-purpose DFT codes, such as WIEN2K ($nldau = 1$)[41], FPLO (select AL in fedit)[22], VASP and PW/SCF.
The FLL-nS functional is available in VASP.

3.2.5 General Remarks

When the Fl-nS and Fl-S functionals are written in their fluctuation form, there is no separate double-counting term, hence one does not need the double-counting interpretation. They can of course be expanded to be written in the 'interaction minus double-counting' form of (3.2), which is useful especially for comparing with functionals that can only be written in that form. A comparison of the double-counting terms is given in Table 3.1. Reducing all to interaction minus double-counting form makes the difference between the functionals most evident; since they all have the same "direct-interaction" term, the *only difference* between the functionals is what double-counting energy is used; the uninteresting tail seems to be wagging the exciting dog, which is in fact the case. The double-counting terms can be reduced to dependence only on N and N_σ thanks to summation rules (there

is at least one free index) on the $U_{mm'}$ and $J_{mm'}$ matrices,

$$\sum_m U_{mm'} = (2l+1)U \tag{3.10}$$

$$\sum_m J_{mm'} = U + (2l)J, \tag{3.11}$$

that is, the sum over any column (or row) of the U and J matrices is a fixed simple value, which depends on the input parameters U and J. One can then simply see that a sum over a column of W is $(2l+1)U$ if $\sigma \neq \sigma'$ and $2l(U-J)$ if $\sigma = \sigma'$.

The $U_{mm'}$ and $J_{mm'}$ matrices satisfy, by definition, $U_{mm} - J_{mm} = 0$, so that there is no self-interaction, whether or not the (vanishing)diagonal term $m\sigma = m'\sigma'$ is included in the interaction term. As mentioned earlier, the following analysis assumes the the occupation matrix has been diagonalized. While this can always be done, the transformed matrix elements $U_{mm'}$ and $J_{mm'}$ will not be exactly what we have used in Sec. 3.6.

3.3 Analysis of the Functionals

The $J = 0$ simplification.

It is not uncommon for practitioners to use 'effective' values $\tilde{U} = U - J, \tilde{J} = 0$ and insert these constants (for U, J) into LDSA+U. For $J = 0$, of course Hund's coupling (intra-atomic exchange) is lost, but J also controls the anisotropy of the interaction, and for $J = 0$ anisotropy also is lost ($U_{mm'} \equiv U$ as well as $J_{mm'} \equiv 0$ for $m \neq m'$). This case is relatively simple, it seems it should provide the "big picture" of what LSDA+U does with simple Coulomb repulsion, and it has been discussed several times before. With $J = 0$,

the fluctuation functionals simplify to

$$\begin{aligned}\Delta E^{Fl-\kappa}_{J=0} &= \frac{U}{2}\sum_{m\sigma\neq m'\sigma'}\delta n_{m\sigma}\delta n_{m'\sigma'} \\ &= \frac{U}{2}\left[\left(\sum_{m\sigma}\delta n_{m\sigma}\right)^2-\sum_{m\sigma}(\delta n_{m\sigma})^2\right] \\ &= -\frac{U}{2}\sum_{m\sigma}(\delta n_{m\sigma})^2 \equiv -\frac{U}{2}\Gamma^2_\kappa \leq 0, \end{aligned} \tag{3.12}$$

because the sum of fluctuations vanishes by definition for either form $\kappa = nS$ or S; note the 'sign change' of this expression when the diagonal terms are added, and subtracted, to simplify the expression. Here Γ^2 is the sum of the squares of the fluctuations, bounded by $0 \leq \Gamma^2_\kappa \leq N$. For integer occupations the energy corrections for Fl-nS and Fl-S (AMF) can be written

$$\begin{aligned}\Delta E^{Fl-S}_{J=0} &= -\frac{U}{2}\left[N(1-\bar{n})-\frac{M^2}{2(2l+1)}\right], \\ \Delta E^{Fl-nS}_{J=0} &= -\frac{U}{2}N(1-\bar{n}). \end{aligned} \tag{3.13}$$

There are two things to note here.

1. In Fl-nS, the energy is independent of both the spin and orbital polarization of the state, which lacks the basic objective of what LSDA+U is intended to model. Considering the form of its double counting term (see Table 3.1) with its self-interaction term (proportionality to N^2), Fl-nS for J=0 becomes simply a self-interaction correction method.

2. In Fl-S (AMF), configurations with magnetic moments are energetically *penalized*, *proportionally to U* and quadratically with M. In later sections we will discuss the partial cancellation with the LSDA magnetic energy.

Under the same conditions, the FLL functional becomes

$$\Delta E^{FLL} = \frac{U}{2} \sum_{m\sigma} n_{m\sigma}(1 - n_{m\sigma}) \geq 0. \tag{3.14}$$

Solovyev *et al.*[40] noted the important and easily recognizable characteristics of this expression. Besides being non-negative, for integer occupations the energy vanishes. It is a simple inverted parabola as a function of each $n_{m\sigma}$. From the derivative, the orbital potentials are linear functions of $n_{m\sigma}$, with a discontinuity of U when $n_{m\sigma}$ crosses an integer value. These characteristics underlie the most basic properties of the LSDA+U method: integer occupations are energetically preferred, and discontinuities in the potentials model realistically the Mott insulator gap that occurs in strongly interacting systems at (and only at) integer filling.

$J \neq 0$, but Isotropic

Simplification of the full expression for a functional results by separating out the isotropic parts of the interaction:

$$U_{mm'} = U + \Delta U_{mm'} \tag{3.15a}$$

$$J_{mm'} = U\delta_{mm'} + J(1 - \delta_{mm'}) + \Delta J_{mm'}. \tag{3.15b}$$

The isotropic parts simplify, giving

$$\begin{aligned} \Delta E^{Fl-nS} &= -\frac{U-J}{2} \sum_{m\sigma} n_{m\sigma}^2 - \frac{J}{4} M^2 \\ &\quad + \frac{U-J}{2} N\overline{n} + \Delta E^{\text{aniso}}, \end{aligned} \tag{3.16}$$

$$\begin{aligned} \Delta E^{Fl-S} &= -\frac{U-J}{2} \sum_{m\sigma} n_{m\sigma}^2 + \frac{U-J}{4} \frac{M^2}{2l+1} \\ &\quad + \frac{U-J}{2} N\overline{n} + \Delta E^{\text{aniso}}, \end{aligned} \tag{3.17}$$

$$\begin{aligned} \Delta E^{FLL} &= -\frac{U-J}{2} \sum_{m\sigma} n_{m\sigma}^2 + \frac{U-J}{2} N \\ &\quad + \Delta E^{\text{aniso}} \end{aligned} \tag{3.18}$$

with the universal anisotropy contribution

$$\Delta E^{\text{aniso}} = \frac{1}{2}\sum_{mm'\sigma\sigma'} \Delta W^{\sigma\sigma'}_{mm'} n_{m\sigma} n_{m'\sigma'}, \tag{3.19}$$

$$\Delta W^{\sigma\sigma'}_{mm'} \equiv \Delta U_{mm'} - \Delta J_{mm'}\delta_{\sigma\sigma'}. \tag{3.20}$$

is the anisotropic part of the interaction matrix elements. These equations, up to the ΔW term, are the extensions of Eq. (3.13) to include isotropic exchange in explicit form.

The first term in each of these expressions contains $-\frac{1}{2}\tilde{U}n^2_{m\sigma}(\tilde{U} \equiv U - J)$ and hence has the appearance of a self-interaction correction. Since the diagonal term of the interaction E_I is specifically excluded, it does not actually contain any self-interaction; in fact, the sign of the interaction E_I is *positive*. (The double counting term does contain terms quadratic in N which must be interpreted as self-interaction.) Nevertheless, the rewriting of the functional leads to a self-interaction-like form, and that part of the functional will have an effect related to what appears in the self-interaction-corrected LDA method, but by an amount proportional to $\tilde{U}$ rather than a direct Coulomb integral, and depending on the difference of $n_{m\sigma}$ from the reference occupation, see Sec. IV.

Fl-nS

For Fl-nS, if we are restricted to integer occupations (so $n^2_{m\sigma} = n_{m\sigma}$), then Γ^2 depends only on N, so the first term in ΔE^{Fl-nS} above depends only on N. Then, up to corrections in ΔU and ΔJ, the state with the largest total spin moment will be favored; this is Hund's first rule. In fact, even with the ΔU and ΔJ terms, the $-JM^2/4$ term is still strongly dominant. Except for $N = 7$, there are many ways to arrange electrons in orbitals which maximizes S. Energy differences between these arrangements arise only from anisotropy (ΔU and ΔJ) and spin-orbit coupling.

Fl-S

In Fl-S, instead of having the $-JM^2/4$ term from Fl-nS which *favors* magnetism, there is a term $\frac{(U-J)}{4(2l+1)}M^2$ which *opposes* magnetism. This term (as in the $J = 0$ case) comes from the occupation variance which wants to evenly distribute electrons across both spin channels. Within LSDA there is something like a Stoner term of the form $-\frac{1}{4}IM^2$ which will compete with this Fl-S magnetic penalty. We return to this aspect in later sections and the appendix.

Spin-orbit Coupling; Particle-Hole Symmetry

Without spin-orbit interaction, for a given N there are many states that are degenerate for both double counting schemes. Every value of N has at least four degeneracies, those with $\pm L_z, \pm S_z$.

Any state which has the same number of spin up as spin down electrons ($M = 0$) gives the same energy from Fl-nS and Fl-S, since then $\bar{n}_\uparrow = \bar{n}_\downarrow = \bar{n}$ (the orbital potentials are distinct, however). Of course this fixed N, M=0 specification may contain many different configurations. Looking at results mentioned later, for Fl-S the ground state for an even number of electrons is $S_z = 0$ (so $\bar{n}_\sigma = \bar{n}$), thus the configuration which gives the Fl-S ground state has the same energy in Fl-S and Fl-nS.

3.4 Fractional Occupations

Here we briefly discuss the effect of non-integer occupations in LSDA+U. Taking a general set of occupations as $\{n_{m\sigma}\}$, we define a set of integer occupations, $\{\hat{n}_{m\sigma}\}$, and the fractional part of the occupations as $\gamma_{m\sigma} = n_{m\sigma} - \hat{n}_{m\sigma}$. For illustration purposes we will choose the simplest possible scenario, where charge is transfered to an empty orbital a from an occupied orbital b both of the same spin, so that $0 < \gamma_{a\uparrow} = -\gamma_{b\uparrow}$, $\hat{n}_{a\uparrow} = 0$ and $\hat{n}_{b\uparrow} = 1$. With this selection, N_σ is unchanged (and therefore, N and M as well) so that E_{dc} is unchanged. Thus, the effect of the charge transfer is entirely contained in the E_I

term. Expanding E_I for the general occupation set gives

$$E_I[\{n_{m\sigma}\}] - E_I[\{\hat{n}_{m\sigma}\}] = U\gamma_{a\uparrow}(1-\gamma_{a\uparrow}) \tag{3.21}$$

for the $J = 0$ case, and for $J \neq 0$ we find

$$\begin{aligned} E_I[\{n_{m\sigma}\}] &- E_I[\{\hat{n}_{m\sigma}\}] \\ &= \sum_{m\sigma}(W_{am}^{\uparrow\sigma} - W_{bm}^{\uparrow\sigma})\hat{n}_{m\sigma}\gamma_{a\uparrow} \\ &\quad -W_{ab}^{\uparrow\uparrow}\gamma_{a\uparrow}^2. \end{aligned} \tag{3.22}$$

The dominant term in (3.22) is where $m\sigma = b\uparrow$. This term gives a contribution $W_{ab}^{\uparrow\sigma'}\gamma_{a\uparrow} \sim U\gamma_{a\uparrow}$ (since $U >> J$ for typical parameter choices, where other terms give contributions proportional to $(W_{am}^{\uparrow\sigma} - W_{bm}^{\uparrow\sigma})\gamma_{a\uparrow} \propto J\gamma_{a\uparrow}$. The term with $m\sigma = a\uparrow$ is killed off by the factor of $\hat{n}_{a\uparrow}$, and the term in γ^2 is significantly smaller than the others for $\gamma < 0.5$.

This shows that there is an energy penalty for fractional occupation, proportional to U and *linear in* γ at small γ. Thus, in configuration space, the LSDA+U functionals have many local minima around configurations with integer occupations. This result is fairly general. Even for charge transfer between orbitals of opposite spins, the linear energy penalty in γ is still dominant over any additional terms coming from the double-counting or spin-orbit.

In practice, this gives the possibility that LSDA+U will get 'stuck' in a local minimum with some configuration that may not be the true ground state. This behavior is not uncommon; LSDA+U has been reported[42] to find multiple local minima depending on the starting configuration.

3.5 Orbital Potential Matrix Elements

Up to now only the energy functionals themselves were discussed. Now we return to the derivatives, the orbital potentials $v_{m\sigma}$. It is simple to derive the exact expressions, and the interaction term E_I common to all forms gives a potential $\Delta v_{m\sigma}$ which depends only on the occupations of the *other* orbitals $n_{m'\sigma'}, m'\sigma' \neq m\sigma$. The potential resulting from the double counting term is functional specific, and may contain a contribution from $n_{m\sigma}$ itself, i.e. a self-interaction.

We confine our observations here to the subdivision (introduced just above) of the interaction into an unitarily invariant isotropic part, and into an anisotropic part Eq. (3.15) that is much smaller and more difficult to analyze. As for the energy itself, it is convenient to add and subtract the diagonal self-Coulomb and self-exchange, which makes the effect of the potential much more transparent at the cost of introducing the misleading self-interaction interpretation.

The potential matrix elements are

$$\begin{aligned}
\Delta v_{m\sigma}^{Fl-nS} &= -(U-J)\left[n_{m\sigma}-\overline{n}\right]-\frac{J}{2}M\sigma \\
&\quad +\Delta v_{m\sigma}^{aniso}, && (3.23)\\
\Delta v_{m\sigma}^{Fl-S} &= -(U-J)\left[n_{m\sigma}-\overline{n}_{\sigma}\right]+\frac{U-J}{2}\frac{M}{2l+1}\sigma \\
&\quad +\Delta v_{m\sigma}^{aniso}, && (3.24)\\
\Delta v_{m\sigma}^{FLL} &= -(U-J)\left[n_{m\sigma}-\frac{1}{2}\right]+\Delta v_{m\sigma}^{\text{aniso}}, && (3.25)
\end{aligned}$$

with the anisotropic potential term

$$\Delta v_{m\sigma}^{\text{aniso}} = \sum_{m'\sigma'} \Delta W_{mm'}^{\sigma\sigma'} n_{m'\sigma'}. \tag{3.26}$$

The main occupation number dependent term, proportional to $n_{m\sigma}$, has a self-interaction appearance and effect, as discussed above for the functionals. The differences in this

term arise from the "reference" occupation with which $n_{m\sigma}$ is compared to determine the potential shift. The "fluctuation" $n_{m\sigma} - n_{\mathrm{ref}}$ is smaller for $Fl-S$ (AMF) than for $Fl-nS$ because the occupation for a given spin direction tends to be closer to $\bar{n}_\sigma$ than to $\bar{n}$. The reference occupation for FLL is, like $Fl-nS$, spin-independent, in fact, the reference is half-filling. In this sense, FLL seems more like a single-band Hubbard model treatment than the other two functionals.

The other difference that is evident in this form is the spin dependence. $Fl-nS$ additionally has a spin orientation dependent potential shift proportional to J and to M (similar to an LSDA treatment, but using J instead of the Stoner I) and enhances spin-splitting of the eigenenergies ε accordingly. In Fl-S (AMF) the analogous term is $+(U-J)\,\frac{M}{2(2l+1)}\sigma$, with a sign that impedes magnetism. It can be simplified to $\approx \frac{J}{2}M\sigma$ when $U \approx 2\,(l+1)\,J$. This expression illuminates the reason that AFM is sometimes found to *decrease* the magnetic moment: this term more or less cancels the spin splitting of LSDA due to the opposite sign. What is left is a splitting of occupied and unoccupied levels due to the $n_{m\sigma}$ term, which is almost independent of M. The effect is to support a spin-polarized solution, but provide little discrimination between different M. Since the spin polarization energy does not favor large M, we end up with a tendency of a near degeneracy of different M values, as we already pointed out from purely energetic arguments. For the case of a half-filled fully polarized shell $n_{ms} = \delta_{\sigma,1}$ (the case $N = M = 7$ in Section 3.6) the potential matrix vanishes, which can be seen from $\overline{n} = \frac{1}{2}\,\frac{M}{2(2l+1)} = \overline{n} = \frac{1}{2}$. However, at the same time the energy contribution also vanishes $\Delta E^{Fl-S} = 0$ (for integer occupations) and the Fl-S functional has no effect at all.

The SIC term in FLL splits occupied and unoccupied states symmetrically, while in the fluctuation functionals the splitting happens with respect to the averaged occupation, which is seen in the overall energy positions in Fig 3.3.

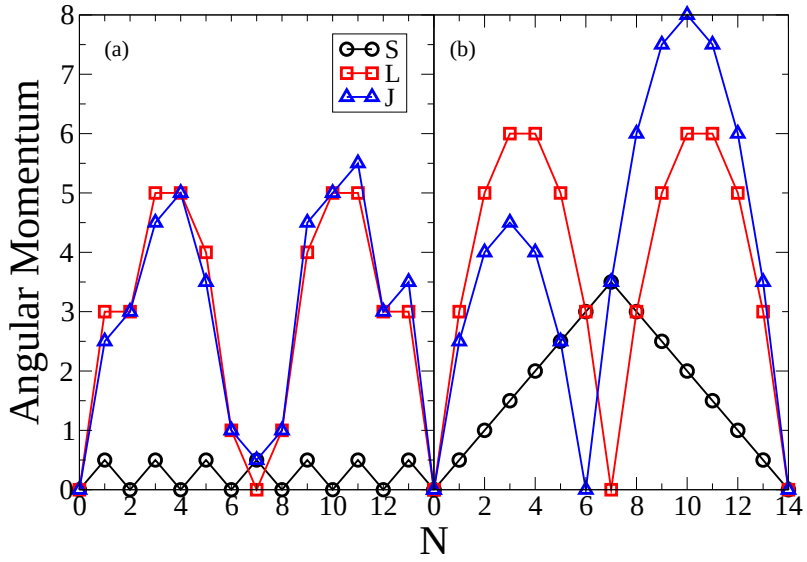

Figure 3.1: (Color online) Angular momentum values of S_z, L_z, and J_z of the lowest energy state for (a) AMF (Fl-S) and (b) FLL, with spin-orbit coupling. Parameter values are $U = 8$, $J = 1$, $I = 0.75$. The AMF (Fl-S) curves do not follow Hund's rules, because the Stoner parameter is too small. FLL follows Hund's rules exactly with these parameters.

3.6 Numerical Results

Following common terminology, for the remainder of the paper we refer to the Fl-S functional simply as the AMF form. We have taken values for $U_{mm'}$ and $J_{mm'}$ (used for Eu) from Ref. [43] (recalculated, to include more significant figures). These matrices are generated using $U = 8$ and $J = 1$ (values typical of rare earths) following the procedure given in the appendix of Ref. [37].

In our analysis of the AMF and FLL functionals, which are based on an LSDA reference state, we include a Stoner term

$$E(M) = -\frac{1}{4} I M^2 \tag{3.27}$$

to model the magnetic effects of LSDA on the total energy. The addition of this term helps to give a picture of the degree to which the functionals reproduce Hund's first rule. Typical values of I for ionized lanthanides are 0.75 eV, so we use this value for the calculations of

this section. Further discussion of the Stoner I is included in the appendix.

Spin-orbit interaction is included in the form

$$E_{SO} = \lambda \vec{S} \cdot \vec{L} \rightarrow \sum_{m\sigma} S_z L_z, \tag{3.28}$$

where the second form applies when only z-components of moments are treated, as is done in current implementations of the LSDA+U method. Due to this restriction, LSDA+U often does not produce the correct multiplet energies in the atomic limit. The visible result in LSDA+U band structures is splittings of occupied, or unoccupied, correlated suborbitals that can be as large as a few times J, and understanding the splittings is not straightforward. For $4f$ systems these splittings[43, 44] may not be of much interest unless one of the correlated bands approaches the Fermi level. In heavy fermion compounds, for example, LSDA+U results are used to infer which parts of the Fermi surface has a larger amount of f character.[45] The same effects (eigenvalue splittings) occur in $3d$ or $5f$ systems, however, where they are expected to become more relevant but are masked by stronger banding tendencies.

Here we consider values of λ of 0 and 0.2 eV. The magnitude of the spin-orbit interaction is not critical to the results; it mainly serves to break degeneracies. Without the spin-orbit interaction, the ground state for any of the functionals at a given N is degenerate with several other states. For instance with $N = 6$, the AMF functional has states with $L_z = 1, S_z = 0$ and $L = 11, S_z = 0$ with the same lowest energy.

In Fig. 3.1 are the ground states for both AMF and FLL with $U = 8$, $J = 1$ and $I = 0.75$. The FLL and Fl-nS (not shown) schemes both reproduce Hund's rules exactly with these parameters. AMF does not reproduce Hund's rules (in fact penalizes magnetism) until I is increased to around 1.5, which is somewhat larger than reasonable values of I. If one expects LSDA+U to reproduce Hund's rules, then the AMF scheme performs rather poorly. For instance, at $N = 7$, Hund's rules ask that all electrons be spin-aligned, but the AMF ground state has only one unpaired spin due to the magnetic penalty appearing in

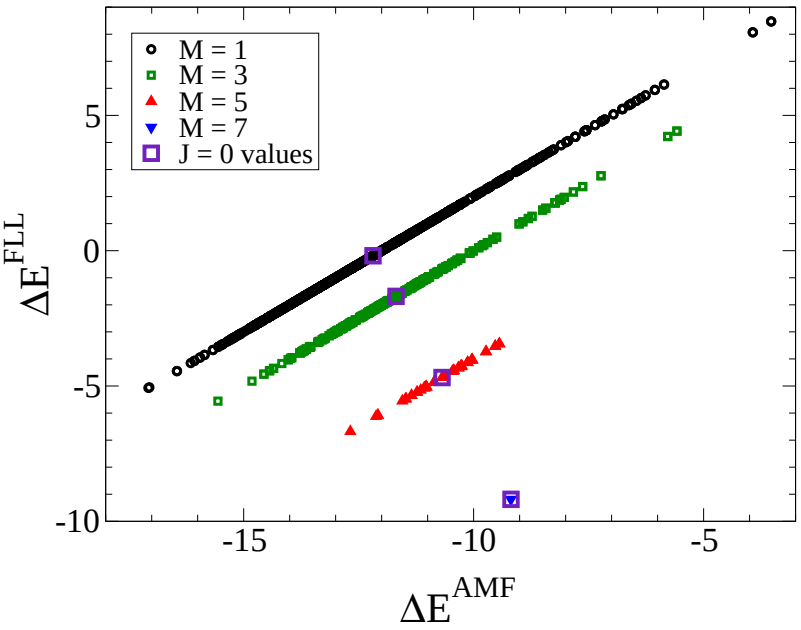

Figure 3.2: (Color online) Shown here is ΔE^{FLL} plotted vs. ΔE^{Fl-S} for each of the 3432 configurations of $N = 7$ electrons, using $U = 8, J = 1, I = 0.75$, all in eV. The ordering of states is shown for Fl-S by counting from left to right, and for FLL by counting from bottom to top. Open squares show values for $U = 7$ and $J = 0$.

Eq. (3.13). With these parameter choices, $U/(2l+1) > I$, so the AMF magnetic penalty wins over the Stoner energy. This is likely to be the case for $3d$ transition metals as well, since $U_{3d}/(2l+1) \sim 1$eV, but it may not be as significant since I for $3d$ elements is larger.

We examine the energetics in more detail in Fig. 3.2, where ΔE for the AMF and FLL functional is plotted for every configuration for $N = 7$. The configurations fall into separate lines for each spin moment M, since E_{dc} depends only on N and M for both functionals. For the case of $J = 0$, all the states with a particular M value collapse to a single energy value (the orbital index loses any impact), this is shown with the open squares. A value of I was chosen so that the cancellation discussed in the previous paragraph is slightly broken.

If we examine the $J = 0$ case first (the large open squares in Fig. 3.2), we see that the separation of states in FLL is much larger than AMF (9 eV versus 3 eV), with $M = 7$ the lowest energy for FLL but highest for AMF. This is a direct consequence of the magnetic

penalty of AMF discussed previously. If I were increased above 1 eV (keeping the other parameters fixed), then AMF would begin to favor the $M = 7$ state by a small amount.

Once J is turned on, the degeneracy is split, and the configurations with a particular M spread out around the $J = 0$ value. The spread is especially large for the highly degenerate $M = 1$ value (from -5 to 8 eV), so that even if I were larger than the typical LSDA value (in which case, with $J = 0$ AMF would favor a high spin state) the large spread of $M = 1$ values would cause the low-spin states to be favored in AMF. This spread is entirely coming from the E_I term and is independent of the double-counting choice. Here we see for AMF a competition between J and I: J is actually preferring a low spin configuration, in contrast to the conventional wisdom that J increases the tendency for magnetism. We see this same tendency occurs in FLL, as for $J = 0$ the separation between $M = 7$ and $M = 1$ states is 9 eV, but with $J = 1$ this separation is reduced to 4 eV. Since in FLL the Hubbard U does not penalize magnetic states the way AMF does, the presence of J is not able to compete with I. This makes it clear why FLL is generally accepted to perform better for systems known to have high-spin states (*e.g.* Eu and Gd). Conversely, FLL may be less successful at modeling low-spin states.

As mentioned previously, it is fairly common for theoretical studies to replace U and J with effective parameters $\tilde{U}$ and $\tilde{J}$. For any double-counting term chosen, using these effective parameters will lower the energy of the high-spin state relative to the low spin state as compared to using U and J directly. With orbitals that are not highly localized, such as $3d$ or $5f$ states it may be the case with FLL that the reduction of the energy separation between high-spin and low-spin caused by using U and J would allow for significant competition between magnetism and kinetic energy in LSDA+U.

We now have seen why and how FLL and AMF perform differently in assigning a magnetic moment. This may be of particular interest for studies of pressure-induced changes in magnetic moment, such as that seen in MnO[34] without changes in orbital M occupancy. Applications of LSDA+U are more thoroughly discussed in Sec. 3.7.1.

Shown in Fig. 3.3 are scatter plots of the energies of all possible states for a given

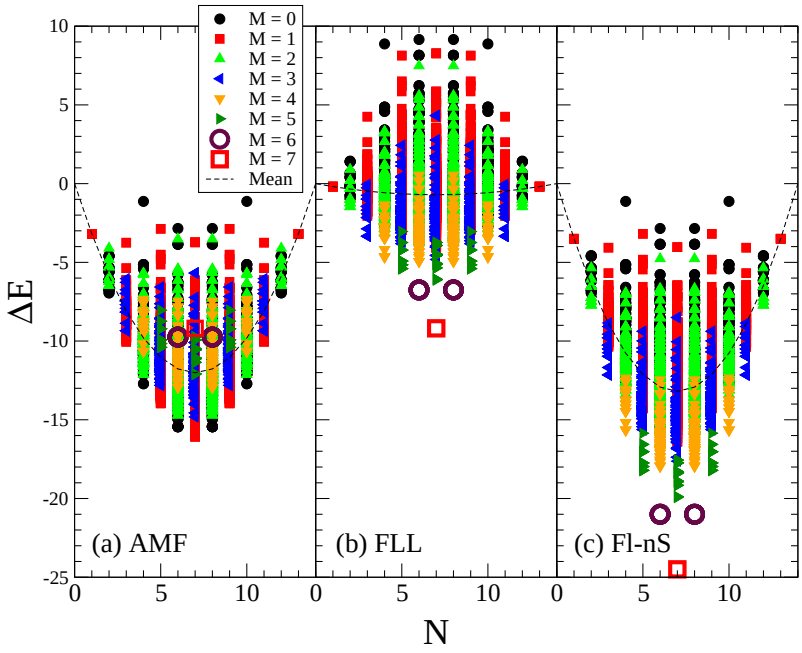

Figure 3.3: (Color online) Scatter plot of all energies ΔE for all states in the (a) AMF(Fl-S), (b) FLL and (c) Fl-nS double-counting schemes, for $U = 8$, $J = 1$, and $I = 0.75$ (FLL and AMF only). Spin-orbit is neglected here. For AMF, low spin states (black circles and red squares) appear as lowest energy configurations for N near 7, but this is not the case for FLL or Fl-nS. The dashed lines indicate the mean energy over configuration for each N; note that the variation with N is much less for FLL than for the other two functionals.

number of f electrons with integer occupations. SO is neglected, as it makes very minor changes to this picture by splitting some degeneracies. The particle-hole symmetry of each functional is apparent. In Fl-nS and FLL, the ground state energy for $N = 7$ is roughly 3 eV lower than the next level, which are the (degenerate) ground states for $N = 6$ and 8. This is almost entirely due to the term depending on M^2 (either the J term in (3.8) or the Stoner term in FLL), because M is large and at its maximum with 7 spins aligned. In AMF low spin states can be seen at the low end of the range for configurations at each N; the high spin states for N=6 and 7 are disfavored by 6-7 eV. We see that the trend where AMF favors low-spin configurations and FLL favors high-spin configurations shown for $N = 7$ in Fig. 3.2 is present for all N. The large spread of values for low spin configurations (black circles, red squares) is seen clearly for AMF as they appear in both

the lowest energy positions and the highest energy positions. The high-spin configurations (large open symbols and triangles) are in the middle of each distribution for N. For e.g. $N = 5$, counting from the lowest energy, $M = 1$ configurations are found first, followed by $M = 3$ configurations then the $M = 5$ configurations are found (with the trend reversing counting up to the highest energy states). In FLL, the lowest energy configurations for $N \neq 7$ are still the configurations with maximum spin for a given N, and states with lower spins are found in succession. Again using $N = 5$ as an example, the $M = 5$ configurations are lowest in energy, and then $M = 3$ configurations are seen at energies lower then $M = 1$ states.

3.7 Discussion

In this paper we have tried to clarify the various functionals that are used in the LSDA+U method, we have compared the functionals formally in certain limits, we have presented the orbital potentials that arise, and we have analyzed the total energy corrections that LSDA+U functionals apply to LSDA total energies, given a set of occupation numbers. The Fl-nS functional which was originally introduced strongly favors spin-polarized states as does the commonly used FLL functional. The other most commonly used functional besides FLL, Fl-S (AMF), has characteristics that tend to *suppress* moment formation or reduce the magnitude of the moment. When analyzed, this AMF functional shows positive energy penalties to magnetism that compete with the magnetic tendencies of the LSDA functional, and when $J > 0$ non-magnetic solutions become even more likely to win out.

When LSDA+U is applied to correlated insulators in the strong coupling regime, it provides a very good picture of the system at the band structure (effective one-electron) level. The initial successes include the $3d$ transition metal monoxides MnO, FeO, CoO, and NiO, for which the LSDA description is very poor. Other early successes included the insulating phases of the layered cuprates that become high temperature superconductors when doped, and the unusual magnetic insulator $KCuF_3$, which was the first case where

important orbital ordering was reproduced. LSDA+U is not a satisfactory theory of single particle excitations of such systems, but nevertheless provides a realistic picture of the underlying electronic structure.

The more interesting cases now lie between the strongly correlated limit of wide-gap magnetic insulators and weakly correlated regime that is well described by LSDA. Some of these are metals, some are unconventional insulators, and many lie near the metal-insulator borderline. It is for these intermediate cases that it becomes essential, if applying the LSDA+U approach, to understand what the method is likely to do, and especially to understand the tendencies of the various choices of functional. This is what we have tried to clarify in this paper. As a summary, we will provide an overview of certain results that have appeared in the literature for systems that lie somewhere in the intermediate correlation regime.

3.7.1 Examples of LSDA+U behavior from applications

Strongly correlated insulators.

Cuprates. The insulating phase of the cuprate class of high temperature superconductors comprised the "killer app" that served to popularize[30, 46] the LSDA+U method, and in the intervening years it has been applied too many times to cite. Simply put, in this system it produces the Cu d^9 ion and accompanying insulating band structure.[46, 47] The hole resides in the $d_{x^2-y^2}$ orbital and is strongly hybridized with the planar oxygen p_σ orbitals, as much experimental data was indicating.

MnO. Experimentally, MnO shows at room temperature a moment collapse from $M = 5$ to $M = 1$ (or less), a volume collapse, and an insulator-to-metal transition, near 100 GPa; this is the classic Mott transition. Within LSDA, the moment decreases continuously with decreasing volume,[48] from the high spin (HS) state to a low spin (LS) state. The insulator-to-metal transition occurs at much too low a pressure (without any other change). A volume collapse is predicted, although the pressure is significantly overestimated (150

GPa).

The application of LSDA+U in its FLL flavor has been applied and analyzed in detail,[34] and provides a different picture in several ways. The ambient pressure band gap is improved compared to experiment. The volume collapse transition occurs around 120 GPa and is accompanied by a moment collapse from $M = 5$ to $M = 1$. The nature of this (zero temperature) transition is insulator to insulator, while the experimental data indicate an insulator-to-metal transition at room temperature. The zero temperature transition might indeed be insulator-to-insulator; such a phase transition would be a type that LSDA+U should work well for. It is also possible that the static mean-field approximation underlying LSDA+U, which favors integer occupations and hence insulating solutions, has too strong a tendency and fails to describe this transition. This question could be settled by studying experimentally the Mott transition at low temperature

Even more unexpected than the insulator to insulator aspect is the LSDA+U prediction is that the low spin state has an unanticipated orbital occupation pattern,[34] being one in which every $3d$ orbital remains singly occupied (as in the high spin state). but spin in two orbitals antialign with those in the other three orbitals. This state is obtained simply from the $M = 5$ HS state by flipping the spins of two of the orbitals. The resulting density remains spherical, but the spin density exhibits an angular nodal structure leading at the same time to a high degree of polarization of the spin-density but a low total moment ($M = 1$). This solution (being the high pressure ground state in LSDA+U) can be traced back to the interplay between symmetry lowering due to the antiferromagnetic order (cubic lowered to rhombohedral) and the anisotropy part of the interaction Eq. 3.20). The symmetry lowering lifts the cubic grouping (t_{2g} and e_g manifolds), thus allowing a higher number of allowed occupation patterns.

The anisotropic part of the interaction is responsible[34] for Hund's second rule ordering of states, which has the tendency to increase the mutual distance of each pair of electrons. If the all-over energetics (band broadening and kinetic effects) reduce the gain of energy due to spin-polarization, then Hund's first rule may become suppressed and the result is a

low spin state. The anisotropic interaction however, is not influenced by this suppression, since it is a local term proportional to a parameter J. It will enforce a Hund's second rule like separation of the electrons under the low spin condition, which can be shown to result exactly in the occupation pattern observed for MnO. In a sense the low spin state is an example of Hund's second rule without Hund's first rule.

FeO, CoO, NiO. Together with MnO, these classic Mott (or 'charge transfer') insulators have been prime applications of the LSDA+U method.[49, 50, 51, 52]. The behavior of the open $3d$ shell in these compounds has not been analyzed in the detail that was done for MnO, however.

Metals

Correlated metals involve carriers that can move, hence they invariably involve fluctuations, in occupation number, in magnetic moment, in orbital occupation, etc. It cannot be expected that a self-consistent mean field treatment such as LSDA+U can answer many of the questions raised by their behavior. However, there is still the question of whether LSDA+U can provide a more reasonable starting point than LSDA alone in understanding these metals. In our opinion, this remains an open question, one for which some evidence is available.

The Fe-Al system has provided one platform for the application of LSDA+U to moderately correlated metals. The systems treated include the Fe impurity in Al (Kondo system, experimentally), and the compounds Fe_3Al, FeAl, and $FeAl_3$. The behavior is too complex to summarize here. The LSDA+U result will, generally speaking, be likely to give a good picture of a Kondo ion when it produces an integer-valent ion with a large value of U. Both FLL and AMF functionals have been applied,[53, 54] with substantially differing results, leading one to question whether either is more realistic than simple LSDA. Results are also sensitive to volume, *i.e.* whether using the experimental lattice constant or the calculated equilibrium value, and the calculated equilibrium is different from LSDA and LSDA+U. One result was that, for moderate $U_{Fe} \sim$ 3-4 eV, AMF strongly reduces the

magnetic moment, while FLL does not.[54] Another application found that the magnetism disappeared within a certain range of intermediate values of U_{Fe}, that is, it was magnetic around small U_{Fe} and also again at large coupling,[53] but non-magnetic between.

Moderately strongly interacting oxides.

Trying to address seriously the electronic structure of intermediate coupling oxides, which are often near the metal-insulator transition, is a challenge that has begun to be addressed more directly. The peculiar Na_xCoO_2 system, which becomes superconducting when hydrated (water intercalates between CoO_2 layers) is one example. One set of studies showed no appreciable difference between FLL and AMF,[55] with both predicting charge disproportionation on the Co ion for x=$\frac{1}{3}$ and $\frac{1}{2}$ for $U \approx$ 2.5-3 eV. It is likely that this compound presents a case where the interplay between LSDA and U has effects that are not fully understood. Also, it is unclear why there is so little difference between the FLL and AMF functionals.

The compound Sr_2CoO_4 is another example. Both functionals show a collapse of the moment[56] around U = 2.5 eV, related to the metal-half metal transition that occurs, but the result for the moments (M(AMF) < M(FLL)) bears out the tendency of AMF to penalize magnetic moments.. The fixed spin-moment calculation in Fig. 9 in Ref. [56] is interesting too, showing the competition between LSDA magnetic energy and AMF magnetic penalty. Also it shows the creation of local minima around M = integer values that LDA+U introduces.

f electron materials.

4f systems. These metals often display the correlated electron physics of a magnetic insulator at the band structure level: background conduction bands provide the metallic nature, while the correlated states have integer occupation. The LSDA+U method seems to be a realistic method for placing the f states closer to where they belong (away from the Fermi level). Gd is a good example, which has been studied at ambient pressure and

compared to photoemission data[50] and magnetic dichroism data.[57, 58] The LSDA+U method has also been applied up to extremely high pressure to assess where the 'Mott transition' in the $4f$ bands is likely to occur. The LSDA+U method has also been applied to heavy fermion metals, for example Cu and U compounds,[59] $PrOs_2Sb_{12}$,[60] and $YbRh_2Si_2$ [61]. In such systems the LSDA+U method may even provide a good estimate of which itinerant states at the Fermi level are most coupled to the localized f states, *i.e.* the Kondo coupling matrix elements. These $4f$ systems may become heavy fermion metals ($YbRh_2Si_2$) or novel heavy fermion superconductors ($YbAlB_4$), or they may remain magnetic but otherwise rather uninteresting metals (Gd).

$5f$ *systems.* A variety of application of the LSDA+U method to $5f$ systems, and especially Pu, have been presented.[62, 63, 64, 65, 66] Given the complexity of the phase diagram of elemental Pu, together with claims that dynamic correlation effects must be included for any realistic description of Pu, a more critical study of Pu would be useful.

3.8 Acknowledgments

We have benefited from discussion on various aspects of this work with M. Johannes, J. Kuneš, A. K. McMahan, I. I. Mazin, and G. Sawatzky. This project was supported by DOE through the Scientific Discovery through Advanced Computing (grant DE-FC02-06ER25794) and by DOE grant DE-FG02-04ER46111.

3.9 Calculation of the Stoner I for $3d$ and $4f$ Shells

The Stoner parameter I is a well established quantity. For metals its value is obtained by a second order expansion of the LSDA xc-energy around the non-magnetic solution, resulting in a Fermi surface averaged integral of the radial wave functions with the xc-kernel.[67] LSDA+U is usually applied to describe insulating states, where the Fermi surface vanishes. In the context of discussing the LSDA contribution to the energy of a correlated d- or f-shell it is more natural to consider the energy contribution from the localized shell. This

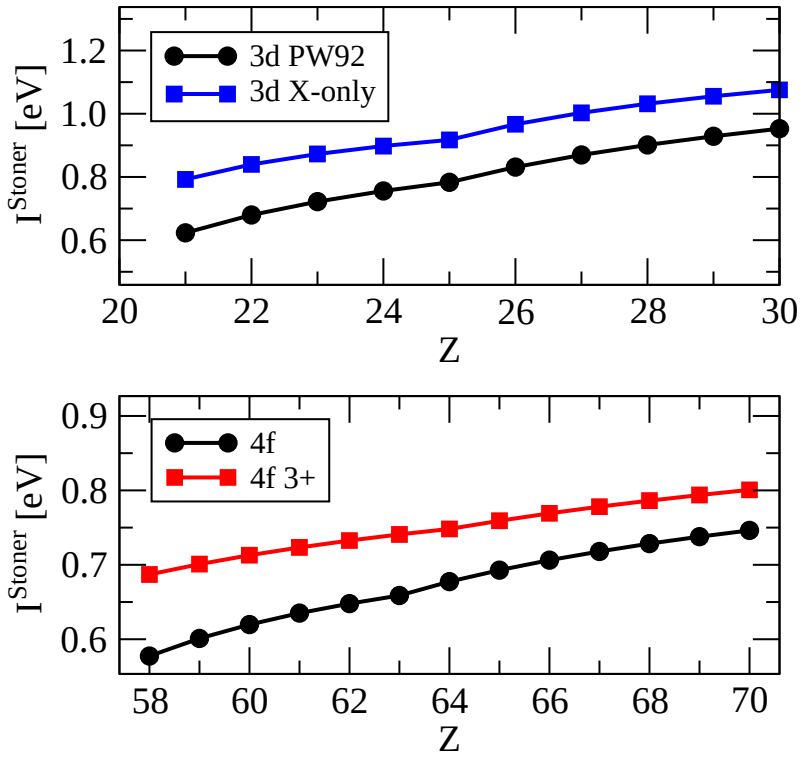

Figure 3.4: Shell-Stoner integrals for the $3d$ and $4f$ atoms. For explanations see text.

leads to a derivation of the Stoner-I similar to the formulation of Janak but adapted to atom-like situations.

Seo presented[68] the second order perturbation theory of the spin polarization in DFT, which results in explicit expressions for the shell exchange parameter I_{nl} that are applicable to atom like situations. In this work a numerical estimate for I_{nl} was derived indirectly from exchange splittings and spin polarization energies taken from DFT calculations. The idea behind this perturbation theory, the expansion the xc-energy around the spherically averaged non-magnetic density of the shell under consideration, was also discussed in the appendix of Kasinathan *et al.*[34] and leads to $\Delta E_{xc} \approx -\frac{1}{4} I_{nl} M^2$ with the shell-Stoner integral

$$I_{nl} = -\frac{1}{2\pi} \int K_0 \left(r\right) \left[R_{nl} \left(r\right)\right]^4 r^2 dr \tag{3.29}$$

$$\begin{aligned} K_0 \left(\vec{r}, \vec{r}'\right) &= \left. \frac{\delta^2 E_{xc}}{\delta m \left(\vec{r}\right) \delta m \left(\vec{r}'\right)} \right|_{n^{\text{spher}}, m=0} \\ &\rightarrow K_0(\vec{r}) \delta(\vec{r} - \vec{r}'). \end{aligned} \tag{3.30}$$

The last expression applies for a local approximation (*viz.* LSDA) to E_{xc}. $K_0(\vec{r}, \vec{r}')$ is a magnetization-magnetization interaction, directly analogous to the second functional derivative of the DFT potential energy with respect to $n(\vec{r})$, which is the Coulomb interaction $e^2/|\vec{r} - \vec{r}'|$ plus an 'xc interaction' arising from E_{xc}.

For a more detailed discussion of the parameter I_{nl} we performed LSDA calculations for free atoms and ions and explicitly calculated I_{nl} from Eq. (3.29). It turns out that $\Delta E_{xc}(M)$ given above is by far the largest M-dependent term of the energy expansion. The spin polarization energy of isolated atoms/ions with spherical M is well described by this estimate with an error smaller than $5 - 10\%$. The resulting shell-Stoner integrals I_{nl} have very similar values compared to the ones obtained from the theory for the metallic situation. (Note, however, that there is a factor of 2 difference in the definition of the

Stoner I in some of the publications.)

For the $3d$ transition element series we get values I_{nl} ranging from 0.62 eV for Sc to 0.95 eV for Zn (see Fig. 4). These values increase across the series by ≈ 0.15 – 0.20 eV, when the exchange only LSDA is used, pointing to a reduction due to (LDA-type) correlation effects when the full xc-kernel is used. For the $4f$ series the shell-Stoner integrals vary from 0.58 eV for Ce to 0.75 eV for Yb. The LDA correlation effects amount to 10% of these values. The values obtained depend on the choice of the reference system, which serves as zeroth order in the functional expansion. For instance for the 3^+-ions of the $4f$-series I_{4f} is increased by $6 - 20\%$ with respect to the neutral atoms.

Chapter 4

Dynamical Mean Field Theory

4.1 Introduction

In recent years, Dynamical Mean Field Theory (DMFT) has gained popularity as a method for studying correlated electron systems. There are many examples where LSDA+U fails to adequately model materials. In DMFT, one constructs separate crystal and impurity problems and solves them self-consistently. In the impurity problem, the electrons interact with an effective bath, or mean field, of conduction electrons determined by the crystal problem. The crystal problem is solved with a Green's function approach using the self-energy from the impurity problem. The impurity problem can be solved by any of a number of many-body techniques designed for that purpose. There are many extensive and detailed reviews of the DMFT method in the literature which discuss both general DMFT and several different impurity solvers that can be used. [69, 70, 71]

4.2 Cavity Method Derivation

There are several different approaches for deriving the DMFT equations. Here I will provide a derivation of DMFT using the cavity method, following closely the approaches taken in Refs. [70] and [72].

The partition function from the path integral formalism of quantum mechanics is

$$Z = \int \prod_{i\sigma} dc^\dagger_{i\sigma} dc_{i\sigma} e^{-S}, \tag{4.1}$$

where the integration variables are Grassman variables, and S is the action. Consider for concreteness, the action for the Hubbard model

$$S = \int_0^\beta d\tau \left[\sum_{i\sigma} c^\dagger_{i\sigma}(\tau) \left(\frac{\partial}{\partial \tau} - \mu \right) c_{i\sigma}(\tau) - \sum_{ij\sigma} t_{ij} c^\dagger_{i\sigma}(\tau) c_{j\sigma}(\tau) + \sum_i U n_{i\uparrow}(\tau) n_{i\downarrow}(\tau) \right]. \tag{4.2}$$

(Hereafter the τ argument to the Fermion operators will be left off for brevity, except where necessary.) The exact nature of the interaction term is unimportant for this derivation, except that it only contains intrasite interactions, and there are no intersite interactions.

The approach taken in the cavity method is to pick a particular site labeled with p, and 'remove' it from the lattice. By integrating out the lattice degrees of freedom, we calculate an effective action for the impurity, satisfying

$$\frac{1}{Z_{\text{eff}}} e^{-S_{\text{eff}}} = \frac{1}{Z} \int \prod_{i \neq p, \sigma} dc^\dagger_{i\sigma} dc_{i\sigma} e^{-S}. \tag{4.3}$$

To start with this we separate the action into the contributions S_p, containing only site p, $S^{(0)}$, coming from the lattice with the cavity, and ΔS which connects the lattice to site p. These contributions are

$$S_p = \int_0^\beta d\tau \left[c^\dagger_{p\sigma} \left(\frac{\partial}{\partial \tau} - \mu \right) c_{p\sigma} + U n_{p\uparrow} n_{p\downarrow} \right] \tag{4.4}$$

$$\Delta S = -\int_0^\beta d\tau \left[\sum_{i\sigma} t_{ip} c^\dagger_{i\sigma} c_{p\sigma} + \text{h.c.} \right] \tag{4.5}$$

$$S^{(0)} = \int_0^\beta d\tau \left[\sum_{i \neq p, \sigma} c^\dagger_{i\sigma} \left(\frac{\partial}{\partial \tau} - \mu \right) c_{i\sigma} - \sum_{i,j \neq p, \sigma} t_{ij} c^\dagger_{i\sigma} c_{j\sigma} + \sum_{i \neq p} U n_{i\uparrow} n_{i\downarrow} \right]. \tag{4.6}$$

Then we rewrite the partition function

$$Z = \prod_{\sigma} \int dc^{\dagger}_{p\sigma} dc_{p\sigma} \exp(-S_p) \int \prod_{i \neq p} dc^{\dagger}_{i\sigma} dc_{i\sigma} \exp(-S^{(0)} - \Delta S) \tag{4.7}$$

The second exponential is expanded to give

$$\exp(-S^{(0)} - \Delta S) = \exp(-S^{(0)}) \left(1 - \Delta S + \tfrac{1}{2!}\Delta S^2 - \dots\right) \tag{4.8}$$

where if one writes $\Delta S = \int_0^{\beta} \Delta S(\tau)$, then powers of ΔS are evaluated with expressions like

$$\Delta S^2 = \int_0^{\beta} \int_0^{\beta} d\tau_1 d\tau_2 \, T \Delta S(\tau_1) \Delta S(\tau_2) \tag{4.9}$$

where T is the time-ordering operator.

Now if the expansion (4.8) is put into (4.7) this gives

$$Z = \prod_{\sigma} \int dc^{\dagger}_{p\sigma} dc_{p\sigma} \exp(-S_p) \int \prod_{i \neq p} dc^{\dagger}_{i\sigma} dc_{i\sigma} \exp(-S^{(0)}) \left[1 - \Delta S + \frac{1}{2!}\Delta S^2 - \dots\right] \tag{4.10}$$

$$Z = \prod_{\sigma} \int dc^{\dagger}_{p\sigma} dc_{p\sigma} \exp(-S_p) \left[1 - \langle \Delta S \rangle^{(0)} + \frac{1}{2!} \langle \Delta S^2 \rangle^{(0)} - \dots\right] \tag{4.11}$$

where the integration over the lattice variables is reduced to average over the action of the lattice with the cavity of powers of ΔS. The first-order term in this expansion is

$$\langle \Delta S \rangle^{(0)} = -\int_0^{\beta} d\tau \sum_{i\sigma} \left[t_{ip} \langle c^{\dagger}_{i\sigma} \rangle^{(0)} c_{p\sigma} + t^{\dagger}_{ip} c^{\dagger}_{p\sigma} \langle c_{i\sigma} \rangle^{(0)} \right] = 0 \tag{4.12}$$

since the averaging over the lattice variables does not include averaging over site p. Similarly, all odd terms in the expansion (4.11) are zero because they average odd numbers of

Fermion operators. The second-order term is

$$\begin{aligned}\langle \Delta S^2 \rangle^{(0)} &= \int_0^\beta \int_0^\beta d\tau_1 d\tau_2 \sum_{i,j\neq p,\sigma} t_{ip} t_{pj}\, c^\dagger_{p\sigma}(\tau_1)\, \langle T c_{i\sigma}(\tau_1) c^\dagger_{i'\sigma}(\tau_2)\rangle\, c_{p\sigma}(\tau_2) \\ &= \int_0^\beta \int_0^\beta d\tau_1 d\tau_2 \sum_{i,j\neq p,\sigma} t_{ip} t_{pj}\, c^\dagger_{p\sigma}(\tau_1)\, G^{(0)}_{ij}(\tau_1-\tau_2)\, c_{p\sigma}(\tau_2). \end{aligned} \tag{4.13}$$

This, and all higher order terms in the expansion (4.7), contain unconnected Green's functions, meaning they can be written as products of lower-order (single particle) Green's functions. The linked cluster theorem allows us to compute the effective action [70, 72]

$$\begin{aligned} S_{\text{eff}} = S_p + \sum_{n=1}^{\infty} \sum_{i_1,\ldots,i_n} \sum_{j_1,\ldots,j_n} \int & d\tau_{i_1} \cdots d\tau_{j_n} t_{i_1 p} \cdots t_{i_n p} t_{p j_1} \cdots t_{p j_n} \\ & \times c^\dagger_{p\sigma}(\tau_{i_1}) \cdots c^\dagger_{p\sigma}(\tau_{i_n}) c_{p\sigma}(\tau_{j_1}) \cdots c_{p\sigma}(\tau_{j_n}) \\ & \times G_{i_1 \cdots j_n}(\tau_{i_1} \cdots \tau_{j_n}). \end{aligned} \tag{4.14}$$

Here we apply the DMFT approximation, by scaling the number of dimensions d to infinity. In order to do this properly, one must also scale the hopping coefficients $t_{ij} \to t_{ij}/\sqrt{d}$. This will keep the kinetic energy on the same scale as the potential energy. The one particle Green's function G_{ij} scales as $(t_{ij})^{|i-j|} \propto d^{-|i-j|/2}$. The two particle Green's function G_{ijkl} scales as $d^{-(|i-j|+|i-k|+|i-l|)/2}$. For the term with the single particle Green's function, the factors of t_{ij} give a contribution proportionate to d^{-1} and the Green's function will give a contribution of d^{-1}. The sums over i and j will give factors of d^2, so the first order term is of order 1. The second order term with i, j, k, l all different will have four factors of t, so that contribution is proportionate to d^{-2}, and four sums give a contribution of d^4, but the differences $|i-j|$, $|i-k|$, $|i-l|$ will all be at least 2, so the net contribution will be

d^{-1} or smaller. All other terms vanish similarly, so the effective action is

$$S_{\text{eff}} = -\int_0^\beta d\tau_i \int_0^\beta d\tau_j c^\dagger_{p\sigma}(\tau_i)\, \mathcal{G}_0^{-1}(\tau_i,\tau_j)\, c_{p\sigma}(\tau_j) + \int_0^\beta d\tau U n_{p\uparrow} n_{p\downarrow} \quad (4.15)$$

$$\mathcal{G}_0^{-1}(\tau_1-\tau_2) = -\left(\frac{\partial}{\partial\tau}-\mu\right)\delta_{\tau_1,\tau_2} - \sum_{ij} t_{ip} t_{pj} G^{(0)}_{ij}(\tau_1-\tau_2) \quad (4.16)$$

where $\mathcal{G}_0$ is the so-called Weiss function.

4.3 Method

Here I will describe the basic method, as implemented in many DMFT codes and by me in FPLO. The self-consistent cycle for DMFT is illustrated in Fig. 4.1. The basic steps followed are:

1. Guess an initial self energy $\Sigma(\omega)$. Generally, $\Sigma(\omega) = 0$ is an adequate initial guess.
2. Compute the crystal Green's $G_{\text{crys}}(\omega)$, the occupation for the correlated orbitals and adjust the chemical potential μ until the desired number of electrons is found.
3. Compute the bath Green's function $\mathcal{G}_0$ to be used as input for the impurity solver.
4. Run the impurity solver, which produces a new interacting Green's function $G_{\text{imp}}(\omega)$.
5. Compute a new self-energy from $G_{\text{imp}}(\omega)$.
6. If the self-energy has not converged, then go to step 2.

The crystal Green's function for a single band model is defined by

$$G_{\text{crys}}(\tau) = \langle c(\tau) c^\dagger(0)\rangle \quad (4.17)$$

$$= \frac{1}{Z}\sum_\psi \langle\psi| e^{-\beta\mathcal{H}_0} e^{-\tau\mathcal{H}_0} c e^{\tau\mathcal{H}_0} c^\dagger |\psi\rangle \quad (4.18)$$

where $\mathcal{H}_0 = \sum_{\mathbf{k}} \varepsilon_{\mathbf{k}} c^\dagger_{\mathbf{k}} c_{\mathbf{k}} - \mu \sum_{\mathbf{k}} c^\dagger_{\mathbf{k}} c_{\mathbf{k}}$ is the non-interacting grand canonical Hamiltonian and $\tau = it$ is the imaginary time. After Fourier transforming to frequency space, the result

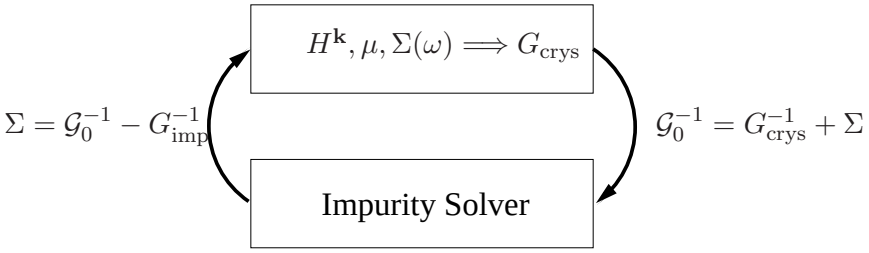

Figure 4.1: Schematic of the DMFT cycle.

is

$$G_{\text{crys}}(i\omega_n) = \sum_{\mathbf{k}} \frac{1}{i\omega_n + \mu - \varepsilon_{\mathbf{k}} - \Sigma(i\omega_n)} \tag{4.19}$$

where $i\omega_n$ are the Matsubara frequencies, which are given by the poles of the Fermi function: $\omega_n = (2n+1)\pi T$ with n running over all integers. $\Sigma(i\omega)$ is the self-energy. The summation $\sum_{\mathbf{k}}$ indicates an average over the Brillouin zone. This result can be generalized to the multiband case

$$G_{\text{crys}}(i\omega_n) = \sum_{\mathbf{k}} \frac{1}{i\omega_n + \mu - H_{\mathbf{k}} - \Sigma(i\omega_n)} \tag{4.20}$$

with $H_{\mathbf{k}}$ as an appropriate single-particle Hamiltonian for the lattice of interest.

In order to find the chemical potential, one needs to be able to calculate the particle count N. In the multiorbital case, the particle count is given by $N = \text{Tr}_\alpha c_\alpha^\dagger c_\alpha$ where Tr_α indicates a sum over basis states. This can be calculated directly from the Green's function in imaginary time, since $\langle c_\alpha^\dagger c_\alpha \rangle = 1 - \langle c_\alpha c_\alpha^\dagger \rangle = 1 - [G_{\text{crys}}(0^+)]_{\alpha\alpha}$. The Fourier transform of $G_{\text{crys}}(i\omega_n)$ gives the orbital occupations,

$$N_\alpha = T \sum_{n=-\infty}^{\infty} G_{\text{crys}}(i\omega_n)\, e^{i\omega_n 0^+}. \tag{4.21}$$

Equation (4.21) must be evaluated with care, due to the discontinuity in G_{crys} at $\tau = 0$. Details on proper evaluation of N_α are given in Sec. 5.2.3.

The crystal Green's function G_{crys} is the fully interacting local Green's function. In order to compute a new self-energy, the impurity solver must have the noninteracting Green's function as input. The noninteracting, or bath Green's function $\mathcal{G}_0$ is computed via the Dyson equation

$$\mathcal{G}_0^{-1}(\omega) = G_{\text{crys}}^{-1}(\omega) + \Sigma(\omega). \tag{4.22}$$

The impurity solver then computes a Green's function $G_{\text{imp}}(\omega)$ for the impurity site, and a new self-energy is computed again from the Dyson equation

$$\Sigma(\omega) = \mathcal{G}_0^{-1}(\omega) - G_{\text{imp}}^{-1}(\omega). \tag{4.23}$$

The convergence criteria for DMFT is that

$$G_{\text{crys}}(i\omega_n) = G_{\text{imp}}(i\omega_n), \tag{4.24}$$

so that all local properties computed in either the impurity or the crystal are equivalent. The condition (4.24) is equivalent to convergence of the self-energy, since for a single iteration

$$\Sigma_{\text{in}} = \mathcal{G}_0^{-1} - G_{\text{crys}}^{-1} \tag{4.25}$$

$$\Sigma_{\text{out}} = \mathcal{G}_0^{-1} - G_{\text{imp}}^{-1}, \tag{4.26}$$

so if the interacting Green's functions are equal then the self-energy will be converged.

4.4 Hubbard I Impurity Solver

4.4.1 Vanilla HI

Hubbard I (HI) is the simplest impurity solver that contains many of the features of the true solution to the impurity problem. However, since HI neglects the DMFT bath,

it cannot reproduce the Kondo physics that is seen in more accurate Quantum Monte Carlo calculations. The main advantage of HI however is that its Green's function can be computed analytically without too much difficulty, so a numerical implementation of DMFT(HI) is very computationally inexpensive.

The Hubbard I Hamiltonian is,

$$H = \frac{1}{2}U\sum_{i\neq j} n_i n_j - \sum_i (\mu - \varepsilon_i) n_i. \tag{4.27}$$

For the remainder of this section, we will assume all the energy levels ε_i are equal to the same value, ε, to simplify expressions. This assumption should be relaxed if there is a strong crystal field present or spin-orbit coupling; in these cases one might assume that there is a set of energy levels with some degeneracy factor, e.g. for a d-subshell one might have three orbitals with energy $\varepsilon_{t_{2g}}$ and two with energy ε_{e_g}. This assumption could also be dropped entirely, but the analytic expressions become very unwieldy, and one must then compute the impurity Green's function and self-energy numerically.

If we define the energy function as

$$E(N) = \tfrac{1}{2}UN(N-1) + (\varepsilon - \mu)N \tag{4.28}$$

then the grand partition function is

$$Z = \sum_{N=0}^{L} \binom{L}{N} e^{-\beta E(N)}. \tag{4.29}$$

The Green's function in imaginary time is calculated as

$$\begin{aligned} G_{ij}(\tau) &= \sum_{\psi} \langle c_i(\tau) c_j^\dagger(0)\rangle & (4.30)\\ &= \frac{1}{Z}\sum_N \sum_{\psi_N} \langle \psi_N | e^{-\beta H} e^{\tau H} c_i e^{-\tau H} c_j^\dagger | \psi_N \rangle & (4.31) \end{aligned}$$

where ψ_N is a wavefunction with N particles, and $\tau = it$ is the imaginary time. We have dropped the usual convention of including the time-ordering operator, because we are taking $\tau \in (0, \beta)$. The above can be simplified to

$$G_{ij}(\tau) = \frac{1}{Z}\sum_N e^{-\beta E(N)} e^{\tau E(N)} \sum_{\psi_N} \langle \psi_N | c_i e^{-\tau H} c_j^\dagger | \psi_N \rangle. \tag{4.32}$$

We will write $c_j^\dagger|\psi_N\rangle = |\psi_{N+1}\rangle(1-n_j)$, with the impliation that n_j is the occupation of the j-th state in the wavefunction ψ. The notation $|\psi_{N+1}\rangle$ is justified because the end result of the inner product will depend only the number of particles, not which particular orbitals are filled. The exponential can then be removed from inside the inner product, because $[H, n_i] = 0$ in this representation so the application of H will not mix orbital occupations. Then we see that G_{ij} will also be diagonal. Thus we have

$$G_{ii}(\tau) = \frac{1}{Z}\sum_N e^{-\beta E(N)} e^{\tau E(N)} e^{-\tau E(N+1)} \sum_{\psi_N} (1 - n_i(\psi_N)). \tag{4.33}$$

Now the summation on the right can be evaluated by looking at it as a probablility problem. In order for $c_i^\dagger|\psi_N\rangle$ to be non-zero, the i-th state must be unoccupied. Put another way, if we take the i-th bin to be unoccupied, how many wave functions have N particles arranged in the other bins? The answer is $\binom{L-1}{N}$. Then we have

$$G(\tau) = \frac{1}{Z}\sum_N \binom{L-1}{N} e^{-\beta E(N)} e^{\tau E(N)} e^{-\tau E(N+1)} \tag{4.34}$$

where the orbital indices on G have been dropped since the result is the same for all orbitals. Also, written this way, the sum over N goes from 0 to $L-1$ particles. The term which has L particles (every orbital filled) does not contribute because a creation operator acting on such a state always gives zero.

The Fourier transform to imaginary frequency we evaluate as

$$G(i\omega_n) = \int_0^\beta e^{i\omega_n \tau} G(\tau) d\tau \tag{4.35}$$

$$= \sum_{N=0}^{L-1} \frac{1}{Z} \binom{L-1}{N} \frac{e^{-\beta E(N+1)} + e^{\beta E(N)}}{i\omega_n + \mu - \varepsilon - UN} \tag{4.36}$$

where we have used the facts that $e^{i\omega_n \beta} = -1$ and $E(N+1) - E(N) = UN + \varepsilon - \mu$.

If we write the HI Green's function as

$$G(i\omega_n) = \sum_{N=0}^{L-1} \frac{A_N}{i\omega_n + \mu - \varepsilon - UN} \tag{4.37}$$

$$A_N = \frac{1}{Z} \binom{L-1}{N} \left[e^{-\beta E(N+1)} + e^{\beta E(N)} \right] \tag{4.38}$$

then we see that $\sum_N A_N = 1$. This is a general property of the HI Green's functions, regardless of the details of the interaction. This is required for the correct high frequency behavior of the imaginary part, $\operatorname{Im} G(i\omega_n) = 1/(i\omega_n)$.

The self-energy is calculated via the Dyson equation,

$$\Sigma(i\omega_n) = i\omega_n + \mu - [G(i\omega_n)]^{-1}, \tag{4.39}$$

where we have taken the bath Green's function $\mathcal{G}_0$ for the isolated atom, $\mathcal{G}_0^{-1}(i\omega) = i\omega + \mu$. At high frequencies, the Green's function and self energy go as

$$G(i\omega_n) = \frac{1}{i\omega_n} + \frac{1}{\omega_n^2} \left[\mu - U \sum_N A_N N \right] \tag{4.40}$$

$$\Sigma(i\omega_n) = U \sum_N A_N N = \frac{L-1}{L} UN. \tag{4.41}$$

The high frequency value of Σ is the paramagnetic Hartree-Fock value.

4.4.2 HI with exchange

HI (U-J) is an attempt to include magnetic effects into the impurity solver.

$$H = \frac{1}{2} \sum_{m\sigma \neq m'\sigma'} (U - J\delta_{\sigma,\sigma'}) n_{m\sigma} n_{m'\sigma'} + \sum_{m\sigma} (\varepsilon_\sigma - \mu) n_{m\sigma} \tag{4.42}$$

where m and m' run over orbital indices, and σ and σ' are spin indices. The energy function depends on the populations of the different spin species, $N_\uparrow$ and $N_\downarrow$. Of course, $N = N_\uparrow + N_\downarrow$.

$$E(N_\uparrow, N_\downarrow) = \frac{U}{2} N(N-1) - \frac{J}{2} \sum_\sigma N_\sigma (N_\sigma - 1) - \mu N + \sum_\sigma \varepsilon_\sigma N_\sigma \tag{4.43}$$

This gives a grand partition function of

$$Z = \sum_{N=0}^{L} \sum_{N_\uparrow = N^-}^{N^+} \binom{\frac{L}{2}}{N_\uparrow} \binom{\frac{L}{2}}{N_\downarrow} e^{-\beta E(N_\uparrow, N_\downarrow)} \tag{4.44}$$

with $N^- = \max(0, N - \frac{L}{2})$ and $N^+ = \min(\frac{L}{2}, N)$.

Computation of the Green's function via the same method as in the previous section gives the result

$$G_\sigma(i\omega_n) = \sum_{N=0}^{L-1} \sum_{N_\sigma = N^-}^{N^+} \frac{A_{N,N_\sigma}}{i\omega_n + \mu - UN + JN_\sigma - \varepsilon_\sigma} \tag{4.45}$$

with the transition weights defined as

$$A_{N,N_\sigma} = \frac{1}{Z} \binom{\frac{L}{2}}{N_{-\sigma}} \binom{\frac{L-1}{2}}{N_\sigma} \left[e^{-\beta E(N+1, N_\sigma + 1)} + e^{-\beta E(N, N_\sigma)} \right]. \tag{4.46}$$

This Green's function will favor magnetic solutions, however if ε_σ is taken as zero, then the it will be identical for both spins. So this impurity solver will not give any spin splitting.

4.4.3 Connecting the Crystal Problem with the Impurity Problem

Since HI neglects the bath Green's function, the usual connection between the lattice problem and impurity problem is broken. Additionally, because the bath is neglected, the impurity solver does not have enough parameters to meet the condition (4.24). Thus, an alternate way to connect the impurity problem with the lattice is needed. Since the only input to the impurity problem in HI (aside from U) is the chemical potential, then the connection has to be made by a particular choice of the chemical potential for the impurity problem. There are two methods used that I am aware of.

Equal Chemical Potential

The approach used by Savrasov is to require that the Green's function at high frequency for the crystal and impurity problem be equal. This uses the same chemical potential for both the crystal and impurity problem. Then equating the first few terms in the high frequency expansion of Green's functions results in $\varepsilon_i = \sum_{\mathbf{k}} (H_{\mathbf{k}})_{ii}$, the LDA on-site energy level of the correlated orbital.

Equal Particle Count

The approach used by Andy McMahan *et al.* is to select a chemical potential so that the particle number of the impurity problem is the same as the occupation of the correlated orbitals in the crystal. This approach may be most appropriate for systems which are expected to be in a mixed valent state, such as Yb. This is equivalent to the condition

$$\sum_n G_{\mathrm{loc}}(i\omega_n) = \sum_n G_{\mathrm{imp}}(i\omega_n). \tag{4.47}$$

In this approach one must iterate the chemical potential for the atomic problem. The iteration procedure is as follows. First an atomic chemical potential μ_{at} is chosen to generate a self-energy, which is then inserted into the crystal problem to compute the number of electrons in correlated orbitals. In this way both the atomic electron count n_{at}

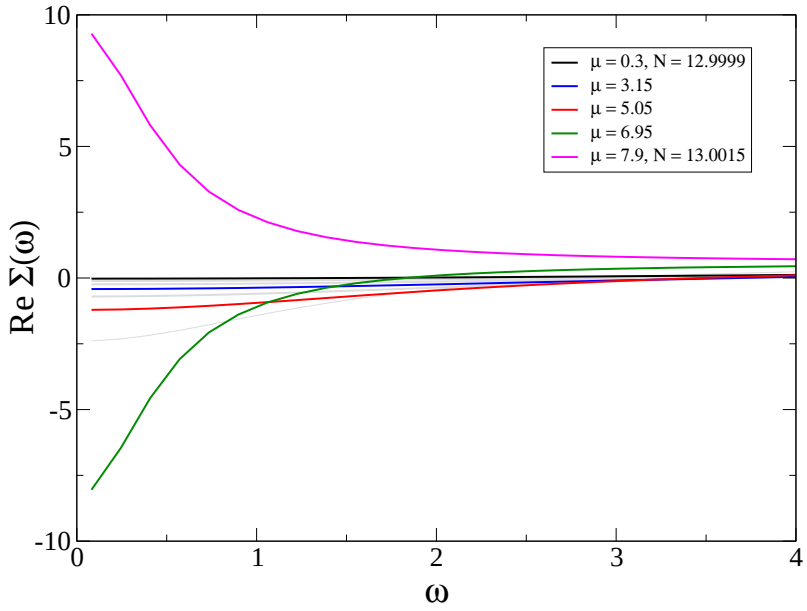

Figure 4.2: Plot of $\Sigma(\omega)$ for various values of the chemical potential μ, at $T = 300$ K and $U = 8$ eV for 14 orbitals. The occupation number $n_{\rm at}$ is 13 for all values of μ used, except where noted. A 'double-counting' value of $12U$ has been subtracted from Σ and μ for clarity. Note the very large response to small changes in N in the small ω region of $\Sigma(\omega)$.

and the occupation of the correlated orbitals in the crystal n_f are functions of $\mu_{\rm at}$. (n_f is of course a function of the crystal chemical potential μ, but μ is fixed by the total electron count in the crystal.) One then iterates $\mu_{\rm at}$ until the condition

$$n_{\rm at}(\mu_{\rm at}) - n_f(\mu_{\rm at}) = 0 \tag{4.48}$$

is satisfied.

This approach has a few limitations. If one downfolds the Hamiltonians to just the correlated orbitals (or uses a model Hamiltonian without uncorrelated bands, such as the Hubbard model), then $n_f = N_{\rm elec}$ will not be a function of $\mu_{\rm at}$. If n_f is fixed to an integer value, then there is a range of $\mu_{\rm at}$ for which $n_{\rm at} = n_f$. Several self-enegies are plotted in Fig. 4.2, several of which (black, blue, red, green curves) have the same $n_{\rm at}$ to three decimal places, but their self-energy is different. There are several values of $\mu_{\rm at}$ which

satisfy the condition (4.48) but they will all have different spectra. Thus, the presence of an extra uncorrelated band in the Hamiltonian into which charge can be transfered from the correlated orbitals is important for this method. This issue may not be quite so bad if one solves the impurity problem allowing each orbital to have its own site energy ε_i, as in (4.27).

To examine a second possible issue with this method, we refer again to Fig. 4.2, if $\Sigma(\omega) < 0$ at low frequencies, the self-energy will behave as an attractive potential, and if $\Sigma(\omega) > 0$ then the self-energy will be repulsive. The most significant contribution to the crystal occupation matrix will come from the low frequency regions of the self-energy, since at high frequencies $\mathrm{Re}\, G_{\mathrm{crys}}(i\omega_n) = \mathrm{Re} \sum_{\mathbf{k}} [i\omega_n + \mu - H_{\mathbf{k}} - \Sigma(i\omega_n)]^{-1}$ will be dominated by the ω_n^{-2} behavior. Small changes in μ near integer occupations can result in a dramatic change in the low frequency behavior of $\Sigma(\omega)$, going from being a strongly attractive potential at $\mu = 6.95$ eV, $N = 13.0000$ to a strongly repulsive potential at $\mu = 7.9$ eV, $N = 13.0015$. If one examines a pole-expansion of the Hubbard I self-energy (described in Sec. 5.3) this large change in the low frequency behavior is due to a pole moving across the $\mathrm{Re}\, \omega = 0$ axis as the chemical potential is increased. If the converged value of n_{at} is not an integer, then the spectrum will always have a Hubbard band pinned near the Fermi energy. For example, taking δ as a small number, at $n_{\mathrm{at}} = 13 + \delta$ the upper Hubbard bands will appear just above the chemical potential, but for $n_{\mathrm{at}} = 13 - \delta$ the lower Hubbard bands will be just below the chemical potential.

4.5 Hirsch-Fye Quantum Monte Carlo Impurity Solver

Quantum Monte Carlo (QMC) methods are very commonly used as DMFT impurity solvers because they provide an essentially exact calculation of the partition function and Green's function for the system. QMC methods stochastically sample the Hilbert space by generating random configurations. There are several different QMC methods used in condensed matter physics today. The method given by Blankenbecler *et al.* [73] is com-

monly used on lattices, and the Hirsch-Fye algorithm [74] is commonly used as an impurity solver for DMFT. Here I will discuss the basics of the Hirsch-Fye method, in the context of DMFT.

Consider a single-band Hamitonian $\mathcal{H} = \mathcal{T} + \mathcal{U}$ which is separable into a kinetic part $\mathcal{T}$ and an interaction part $\mathcal{U}$. $\mathcal{T}$ must be quadratic in Fermion operators, and $\mathcal{U}$ must take the form of a density-density interaction

$$\mathcal{V} = \sum_{mm'} U_{mm'} n_m n_{m'} \tag{4.49}$$

where the indices m, m' may be a combined orbital-spin index. The partition function for this system may be written

$$Z = \operatorname{Tr} e^{-\beta\mathcal{H}} = \prod_{l=1}^{L} e^{-\Delta\tau(\mathcal{T}+\mathcal{V})} \approx \prod_{l=1}^{L} e^{-\Delta\tau\mathcal{T}}\, e^{-\Delta\tau\mathcal{V}} \tag{4.50}$$

with $\Delta\tau = \beta/L$. The breakup of the exponentials in (4.50) is the only source of systemic error introduced into the algorithm. The first term in the error in $\ln Z$ is related to the commutator $[\Delta\tau\mathcal{T}, \Delta\tau\mathcal{V}] \propto \Delta\tau^2$, so we see that as L gets large, the error will be proportionate to L^{-2}, going to zero as L goes to infinity.

The Fermion operators in V can be decoupled by introducing auxillary spin fields $\sigma^l_{mm'}$ with the identity

$$\exp\left(\Delta\tau U_{mm'}\left(n_m n_{m'} - \tfrac{1}{2}(n_m + n_{m'})\right)\right) = \exp(\lambda_{mm'}\sigma^l_{mm'}(n_m - n_{m'})) \tag{4.51}$$

$$\cosh(\lambda_{mm'}) = \exp(-\Delta\tau U_{mm'}/2) \tag{4.52}$$

These auxillary spins may take values of ± 1, so they are often thought of as Ising spins. One such spin is introduced for every coupling m, m' at every time slice. With this decoupling

the Hamiltonian at each time slice l can be written as

$$\mathcal{H}^l = \sum_{\alpha\beta} H^l_{\alpha\beta} c^\dagger_\alpha c_\beta. \tag{4.53}$$

If we then define the matrix

$$B_l = e^{\Delta\tau H^l} \tag{4.54}$$

then the partition function can be written as the determinant of an $NL \times NL$ matrix

$$Z = \det G^{-1} = \det \begin{bmatrix} 1 & 0 & 0 & & B_1 \\ -B_2 & 1 & 0 & \cdots & 0 \\ 0 & -B_3 & 1 & & 0 \\ & \vdots & & \ddots & \\ 0 & 0 & 0 & -B_L & 1 \end{bmatrix}. \tag{4.55}$$

and with a matrix identity, (4.55) can be reduced to an $N \times N$ matrix,

$$Z = \det(1 + B_L B_{L-1} \cdots B_2 B_1). \tag{4.56}$$

The QMC procedure proceeds by making flips of single Ising spins $\sigma^l_{mm'}$ and accepting or rejecting these moves based on their relative probability. When a spin is flipped at at time slice l, this results in a change in the B matrix

$$B_l = e^{\Delta\tau H^l} \longrightarrow B_l e^{\Delta\tau \Delta H^l} \equiv B_l \Xi_l \tag{4.57}$$

where Ξ_l is the identity matrix, except for an element $(1+D)$ at the position the H_l matrix changed when the spin flipped (henceforth denoted as γ). The probability for accepting the spin flip is related to the ratio of the new partition function to the old one

$$R = \frac{Z_{\text{new}}}{Z_{\text{old}}} = \det\left[(1 + B_{l-1}B_{l-2}\cdots B_1 B_L \cdots B_l)^{-1}(1 + B_{l-1}B_{l-2}\cdots B_l \Xi_l)\right]. \tag{4.58}$$

The actual probability when a thermal bath is present (always the case in DMFT) is $Z_{\text{new}}/(Z_{\text{old}} + Z_{\text{new}}) = R/(1+R)$.

Once a spin flip is accepted, the Green's function can be updated with

$$G_{\text{new}} = (1 + (1 - G)(\Xi_l - 1))^{-1} G. \tag{4.59}$$

Since $\Xi_l - 1$ is a matrix with a single non-zero element, the update equation can be reduced to

$$G^{\text{new}}_{\alpha\beta,ll'} = G_{\alpha\beta,ll'} - \frac{X_{\alpha\gamma,ln}\, \Delta H^n_{\gamma\gamma}\, G_{\gamma\beta,nl'}}{1 + X_{\gamma\gamma,ll'} \Delta H_{\gamma\gamma}} \tag{4.60}$$

where Greek letters inidate spacial or orbital indices, Roman letters indicating time slice indices, and γ and n respectively indicate the site(orbital) and time slice indices where the spin flip occurred. The matrix X is defined by $X = 1 - G$.

4.5.1 Analytic Continuation

The QMC algorthim calculated $G(\tau)$, the Green's function on the imaginary time axis. This can be easily transformed to $G(i\omega_n)$ where $i\omega_n$ are the imaginary Matsubara frequencies. Generally one is interested in the real frequency spectral function $A(\omega) = -\frac{1}{\pi} \operatorname{Im} G(\omega)$. The imaginary time Green's function can be calculated from $A(\omega)$ with the relation

$$G(\tau) = \int_{-\infty}^{\infty} \frac{e^{-\tau\omega}}{1 + e^{-\beta\omega}} A(\omega)\, d\omega, \tag{4.61}$$

however this relation is difficult to invert numerically due to the exponential decay in the Kernel. In any case, $G(\tau)$ can be Fourier transformed to $G(i\omega_n)$, and in this case the relation (4.61) becomes

$$G(i\omega_n) = \int_{-\infty}^{\infty} \frac{A(\omega)}{i\omega_n - \omega}\, d\omega. \tag{4.62}$$

There are several different methods for constructing $A(\omega)$ from $G(\tau)$ [75, 76, 77], but the most successful method in recent years is the Maximum Entropy (MaxEnt) Method [78, 79]. Here I will describe the MaxEnt method, following the nomenclature used by

Silver *et al.* in Ref. [78]. The basic idea behind it is that since the relation (4.61) cannot be inverted accurately for noisy data, we construct the best $A(\omega)$ we can (based on statistical arguments) which gives the correct $G(\tau)$.

The statistical argument is based around the Baynes theorem which states

$$P[X,Y] = P[X|Y]P[Y] = P[Y|X]P[X] \tag{4.63}$$

where $P[X,Y]$ is the joint probability of X and Y, and $P[X|Y]$ is the probability of X given Y. In the application to QMC data, X and Y become $G(\tau)$ and $A(\omega)$. Ultimately, the algorithm seeks to maximize the posterior function $P[A(\omega)|G(\tau)]$, calculated via

$$P[A(\omega)|G(\tau)] = P[G(\tau)|A(\omega)] \cdot P[A(\omega)] \cdot \frac{1}{P[G(\tau)]}. \tag{4.64}$$

$P[G(\tau)]$ does not need to be considered here, as the probability of measuring the $G(\tau)$ that has already been measured will not be relevant for finding the $A(\omega)$ for that $G(\tau)$. $P[G(\tau)|A(\omega)]$ is termed the likelihood function, as it indicates the probability of measuring the measured Green's function given that the spectral function is $A(\omega)$. To calculate the likelihood function some assumption must be made about the error in the measured data points for $G(\tau)$. Generally one assumes that distribution for each of the data points $G(\tau_l)$ is a Gaussian distribution with standard deviation σ_l. (This is generally a good assumption, however care must be taken for τ-points where the measured $G(\tau)$ is close to zero, because $G(\tau)$ in the range $(0,\beta)$ is a non-negative function, so the data measurements at these τ-points will not likely be Gaussian distributed.) In this case, one calculates the fitted Green's function $G_f(\tau_l)$ using the relation (4.61) and the likelihood function is then calculated as

$$P[G(\tau)|A(\omega)] \propto \exp\left[-\frac{1}{2}\chi^2\right] \tag{4.65}$$

$$\chi^2 = \sum_l \frac{1}{\sigma_l^2}\left[G_f(\tau_l) - G(\tau_l)\right]. \tag{4.66}$$

The function $P[A(\omega)]$ is called the prior probability; it represents the probability of $A(\omega)$ as a spectral function before making any QMC measurements. The prior probability should enforce any constraints on $A(\omega)$ (for instance, $P[A(\omega)]$ should be zero for if $A(\omega) < 0$ for any ω). The method for calculating the prior probability is what gives this method its name:

$$P[G(\tau)|A(\omega)] \propto \exp[\alpha S] \tag{4.67}$$

$$S = \int d\omega \left[A(\omega) - M(\omega) - A(\omega) \ln \frac{A(\omega)}{M(\omega)} \right] \tag{4.68}$$

where S is the entropy taken from information theory. $M(\omega)$ is called the default model, and it is used as a starting guess for $A(\omega)$. If the statistical data on $G(\tau)$ is good then the choice of the default model should not have an impact on the resulting $A(\omega)$.

4.5.2 Orbital Susceptibility

The $\mathbf{q}$-dependent orbital susceptibility can be calculated as follows.

We use a Dyson-like equation to compute the $\mathbf{q}$-dependent susceptibility,

$$\chi_{\mathbf{q}} = \chi^0_{\mathbf{q}} + \chi^0_{\mathbf{q}} \Gamma \chi_{\mathbf{q}} \tag{4.69}$$

where the vertex function Γ has to be calculated from the impurity solver [80] and the bare susceptibility is given by

$$\left(\chi^0_{\mathbf{q}}\right)_{ij,lm} = T \sum_{\mathbf{k}} G^{\mathbf{k}}_{il} G^{\mathbf{k}+\mathbf{q}}_{mj} \tag{4.70}$$

where v_{kl} is an arbitrary potential applied to the orbitals. By choosing v in different ways, one obtain get the magnetic susceptibility, orbital susceptibility, etc. In fact all (frequency-independent) susceptibilities can be obtained as linear combinations of the matrix elements of $\chi_{\mathbf{q}}$.

The vertex function must be calculated within the QMC algorithm. Since it is momen-

tum independent, evaluating on the impurity site is done with an equation of the same form as (4.69), however the **q** dependent susceptibilities are replaced by local susceptibilities. [81]

$$\chi_{loc} = \chi^0_{loc} + \chi^0_{loc}\Gamma\chi_{loc} \tag{4.71}$$

The two-particle function χ_{loc} can be calculated from one particle Green's functions using the Wick theorem

$$\begin{aligned}(\chi_{loc})_{ij,lm} &= \langle c_i c_j^\dagger c_l c_m^\dagger \rangle \\ &= \langle c_i c_j^\dagger \rangle \langle c_l c_m^\dagger \rangle - \langle c_i c_m^\dagger \rangle \langle c_l c_j^\dagger \rangle \end{aligned} \tag{4.72}$$

where the time arguments on the Fermionic operators have been suppressed for clarity. The bare local susceptibility is trivially calculated using the QMC local Green's functions $(\chi^0_{loc})_{ij,lm} = (G_{loc})_{il}(G_{loc})_{mj}$.

There is no self-consistency to this procedure. Once the DMFT(QMC) calculation has converged, one needs only to calculate the vertex function and then the full susceptibility (4.69) can be calculated for any **q**-point desired.

Chapter 5

Charge Self-Consistent Implementation of LDA+DMFT

5.1 Local Orbital Basis

The FPLO code uses a local orbital basis, the details of which are described elsewhere [22]. For our purposes here it is important to realize that the basis functions are non-orthogonal. The on-site atomic orbitals are orthogonal, but Bloch basis functions are not orthogonalized. This necessitates the use of the overlap matrix $S_{\mathbf{k}}$ in DFT or DMFT formalisms. Some care must be made in defining creation and annihilation operators.

Throughout this section, it will be necessary to refer to the square root or inverse of a matrix. This will be done with the notation $S^{1/2}$, and a reference to matrix elements will be $S^{1/2}_{ab}$ which means the a,b element of the matrix $S^{1/2}$. A matrix element is raised to a power will be clarified with parenthesis, e.g. $(S_{ab})^{1/2}$.

5.1.1 Nonorthogonal Basis

First, we examine the properties of a non-orthogonal basis. We will use roman characters to denote states in a non-orthogonal basis and greek characters to denote states in an

orthogonal basis. The overlap matrix is defined by

$$\langle b|a\rangle = S_{ba}. \tag{5.1}$$

We will define an orthogonal basis using a Löwdin transformation,

$$|\beta\rangle = \sum_b S^{-1/2}_{b\beta}|b\rangle \tag{5.2}$$

$$\langle\beta| = \sum_b S^{-1/2}_{\beta b}\langle b|. \tag{5.3}$$

It is straightforward to show that $\langle\beta|\alpha\rangle = \delta_{\beta,\alpha}$. There is a one-to-one correspondance between the states in the orthogonal basis and the states in the non-orthogonal basis, so indices on the S matrix can be mixed without ambiguity. It is necessary, of course, that even though S has many possible square roots, the matrix $S^{1/2}$ must be chosen in a way that is consistent throughout this paper. The matrix $S^{-1/2}$ may not be an arbitrarily chosen square root of S^{-1}; it must be the inverse of the chosen $S^{1/2}$.

The inverse transformations to (5.2) and (5.3) can be found as

$$|b\rangle = \sum_\beta S^{1/2}_{\beta b}|\beta\rangle \tag{5.4}$$

$$\langle b| = \sum_\beta S^{1/2}_{b\beta}\langle\beta|. \tag{5.5}$$

The completeness relation can be written in terms of the non-orthogonal basis states as

$$1 = \sum_\alpha |\alpha\rangle\langle\alpha| = \sum_{ab} |a\rangle S^{-1}_{ab}\langle b| \tag{5.6}$$

5.1.2 Second Quantization

Now we can relate the creation and annihilation operators for the non-orthogonal basis to the operators for the orthogonal basis. We will only consider Fermions here. Annihilation operators will be denoted with a letter c, and creation operators with the letter d. As we

shall see shortly, for the non-orthogonal basis these are not adjoints of one another. (This relation is, of course, still true for the orthogonal basis, ie. $d_\beta = c_\beta^\dagger$.) The annihilation operator can be found by expanding in operators for the orthogonal states. This expansion gives

$$c_b|b\rangle = \sum_\beta A_\beta c_\beta \sum_\alpha S_{\alpha b}^{1/2}|\alpha\rangle \tag{5.7}$$

$$= \sum_\beta A_\beta S_{\beta b}^{1/2}|0\rangle = |0\rangle \tag{5.8}$$

where $|0\rangle$ is the vacuum state. We have used the fact that $c_\beta|\alpha\rangle = \delta_{\beta,\alpha}|0\rangle$. The solution here is clearly that $A_\beta = S_{b\beta}^{-1/2}$. Then we have our annihilation operator as

$$c_b = \sum_\beta S_{b\beta}^{-1/2} c_\beta \tag{5.9}$$

Interestingly, $c_b^\dagger$ is not an operator which creates a particle in state b. Instead, its action on the vacuum state gives

$$c_b^\dagger|0\rangle = \sum_\beta S_{\beta b}^{-1/2}|\beta\rangle \tag{5.10}$$

which is not the state $|b\rangle$. In order to get a creation operator, we must find it by solving $d_b|0\rangle = \sum_\beta A_\beta d_\beta|0\rangle = |b\rangle$. Doing so gives the result

$$d_b = \sum_\beta S_{\beta b}^{1/2} d_\beta. \tag{5.11}$$

The action of the conjugate of d_b is $d_b^\dagger|a\rangle = S_{ba}|0\rangle$. It's then straightforward to show that the following anti-commutation relations hold,

$$\{c_b, c_a^\dagger\} = S_{ba}^{-1} \tag{5.12}$$

$$\{d_b, d_a^\dagger\} = S_{ab} \tag{5.13}$$

$$\{c_b, d_a\} = \{c_b^\dagger, d_a^\dagger\} = \delta_{ab} \tag{5.14}$$

and all anti-commutators with other combinations of c, $c^\dagger$, d, $d^\dagger$ give zero.

Now we can consider how operators can be expressed in second quantization notation. Consider a general single-particle operator $\mathcal{H}$, with matrix elements $H_{\alpha\beta}$ in the orthogonal basis. The matrix elements in the nonorthogonal basis are

$$\langle a|\mathcal{H}|b\rangle = \sum_{\alpha\beta} S_{a\alpha}^{1/2} H_{\alpha\beta} S_{\beta b}^{1/2}, \tag{5.15}$$

which is easily obtained by inserting identity operators in the orthogonal basis. To write the operator $\mathcal{H}$ in the nonorthogonal basis, first write $\mathcal{H}$ in the orthogonal basis, and then use the relations (5.9) and (5.11) to expand. This gives

$$\begin{aligned} \mathcal{H} &= \sum_{ab} (S^{-1/2} H S^{1/2})_{ab}\, d_a c_b \\ &= \sum_{ab} d_a c_b \sum_c S_{ac}^{-1} H_{cb}. \end{aligned} \tag{5.16}$$

5.2 LDA+DMFT

5.2.1 Double Counting

Correcting for the double counting of the Coulomb energy is done in the same way as in LDA+U. There are two functionals that are commonly used in LDA+U, the Fully Localized Limit (FLL) and the Around Mean Field (AMF) scheme. The LDA+U function

is generally written as

$$E_{\text{LDA+U}} = \frac{1}{2} \sum_{mm'\sigma\sigma'} U^{\sigma\sigma'}_{mm'} n_{m\sigma} n_{m'\sigma'} - E_{DC}. \tag{5.17}$$

The two double-counting terms used are

$$E^{FLL}_{DC} = \frac{1}{2}UN(N-1) - \frac{1}{2}J\sum_{\sigma} N_\sigma(N_\sigma - 1) \tag{5.18}$$

$$E^{AMF}_{DC} = \frac{1}{2}UN^2 - \frac{U+2lJ}{2(2l+1)}\sum_{\sigma} N^2_\sigma \tag{5.19}$$

where l is the orbital angular momentum.

In the application of double counting to DMFT, we must apply these as orbital potentials. So by differentiating the double counting energies with respect to orbital occupations we get

$$V^{FLL}_{\sigma} = U\left(N - \tfrac{1}{2}\right) - J\left(N_\sigma - \tfrac{1}{2}\right) \tag{5.20}$$

$$V^{AMF}_{\sigma} = \frac{2l}{2l+1}(U-J)N_\sigma + UN_{-\sigma}. \tag{5.21}$$

For application in DMFT, one of these functionals is chosen and the potential is subtracted from $\Sigma(i\omega)$ for each correlated orbital.

An orbital potential that is independent of frequency could be applied in the DMFT formalism by simply choosing $\Sigma(\omega) = \text{const}$. This is essentially what LDA+U does. The self-energy calculated from the impurity solvers differs from a constant value only at low imaginary frequency (on the imaginary frequency axis). However, the low frequency behavior of G_{crys} plays a significant role in determining orbital occupations, so it is not clear that the double-counting schemes used in LDA+U would have the same applicability in LDA+DMFT. It does not appear that the details of double-counting in LDA+DMFT have been studied in detail at all.

5.2.2 DMFT Interface with FPLO

FPLO is organized to implement the Kohn-Sham DFT formalism. This involves constructing the K-S Hamiltonians from the density, diagonalizing them to produce orbital occupations, forming a new density, and repeating until the density converges. A single step of this iteration is completed in the `fplo_step` function defined in the `fplostep.f90` file. This function initially does some work to optimize the basis functions and set up the Kohn Sham calculation, and then calls the function `calc_KS_states` to perform the actual diagonalization of the LDA Hamiltonians. After that `fplo_step` computes the output density and does some basic analysis of it. Mixing of the density appears to be done at a level outside this function.

To implement DMFT, I replace the call to `calc_KS_states` to a call to my own function `dmft_driver`. This is done with appropriate conditional statements to the application of DMFT can be turned on/off with a switch in the input file. The function `dmft_driver` then performs the entire DMFT calculation, and fills the appropriate output variables for computing the density.

5.2.3 Calculation of Local Orbital Occupation Values

Details on the FPLO basis set can be found in Ref. [22] and will not be presented here, except where necessary. It is worthwhile to mention that the on-site orbitals on an atom are orthogonal, that is $\sum_{\mathbf{k}} S_{\mathbf{k}} = I$, the identity matrix. Provided the crystal under study has inversion symmetry, then for all local quantities the block corresponding to a group of orbitals on a single atom will be diagonal (there may be off-diagonals if there are multiple atoms in the unit cell). Off-diagonal elements in the bath Green's function (due to multiple atoms or numerical precision) would be neglected with an impurity solver other than Hubbard I. Currently only Hubbard I is implemented.

The crystal Green's function for a non-orthogonal basis is defined on the imaginary

frequency axis by (4.20)

$$G_{\mathbf{k}}(i\omega_n) = [(i\omega_n + \mu)S_{\mathbf{k}} - H_{\mathbf{k}} - \Sigma(i\omega_n)]^{-1} \quad (5.22)$$

$$G^{\text{net}}_{\text{crys}}(i\omega_n) = \sum_{\mathbf{k}} G_{\mathbf{k}}(i\omega_n) \quad (5.23)$$

where $i\omega_n$ are the Matsubara frequencies, μ is the chemical potential, $H_{\mathbf{k}}$ is the LDA Hamiltonian and $\Sigma(i\omega)$ is the self-energy. The $H_{\mathbf{k}}$ and $S_{\mathbf{k}}$ matrices are of dimension $N_{\text{orb}} \times N_{\text{orb}}$, and they are Hermitian but not sparse. The $\Sigma(i\omega_n)$ matrix is also of dimension $N_{\text{orb}} \times N_{\text{orb}}$, but it has non-zero values only on the subset of the orbitals which are treated as correlated and (usually) is diagonal. $\Sigma(i\omega_n)$ is a complex symmetric matrix and is not Hermitian. It should also be noted here that the summation $\sum_{\mathbf{k}}$ indicates an average over $\mathbf{k}$.

In the FPLO basis, (5.23) actually corresponds the on-site Green's function (called 'net' in FPLO terminology), which when summed over $i\omega_n$ gives only the on-site contributions to the occupation. To calculate the total occupation, one computes the gross Green's function

$$G^{\text{gross}}_{\text{crys}}(i\omega_n) = \sum_{\mathbf{k}} G_{\mathbf{k}}(i\omega_n) S_{\mathbf{k}} \quad (5.24)$$

The CPU time for evaluating this is linear in the number of Matsubara frequencies and $\mathbf{k}$-points, so very little can be done to reduce the cost in this respect. The matrix inversion is somewhat costly, scaling as $O(N^3_{orb})$. This cost can be mitigated somewhat by using a geometric series expansion for high frequencies,

$$G^{\text{net}}_{\text{crys}}(i\omega_n \to \infty) = \frac{1}{i\omega_n} \sum_{\mathbf{k}} \left[S^{-1}_{\mathbf{k}} - \frac{1}{i\omega_n} S^{-1}_{\mathbf{k}} L_{\mathbf{k}} \right] \quad (5.25)$$

with $L_{\mathbf{k}} = \mu - S^{-1}_{\mathbf{k}} H_{\mathbf{k}} - S^{-1}_{\mathbf{k}} \Sigma(\infty)$. The product $S^{-1}_{\mathbf{k}} L_{\mathbf{k}}$ is independent of frequency, so in this way the matrix inverse at each frequency can at large frequencies be replaced by matrix addition operations which are $O(N^2_{orb})$.

The density matrix is calculated from $G_{\rm crys}$ by the following formula,

$$\rho^{\rm gross} = T\sum_n G^{\rm gross}_{\rm crys}(i\omega_n)e^{i\omega_n 0^+} \tag{5.26}$$

$$= T\sum_n G^{\rm gross}_{\rm crys}(i\omega_n) + \tfrac{1}{2}I_{N_{orb}} \tag{5.27}$$

where $I_{N_{orb}}$ is the $N_{orb}\times N_{orb}$ identity matrix. The density matrix can be calculated for both net and gross occupations, which is a useful when $\Sigma(i\omega_n)=0$ as check of the code against the LDA output, but the gross occupation is the physical number of electrons and μ must be adjusted so that $\mathrm{Tr}\,\rho^{\rm gross} = N_{\rm elec}$. Henceforth, the density matrix for gross occupations will simply be referred to as ρ, and $G^{\rm gross}_{\rm crys}$ will be referred to as $G_{\rm crys}$.

The extra term in (5.27) comes from the fact that we are using the Fourier transform $G_{\rm crys}(i\omega_n)$ to evaluate $\lim_{\tau\to 0^+} G_{\rm crys}(\tau)$. $G_{\rm crys}(\tau)$ is anti-periodic with a discontinuity at $\tau=0$. The jump in $G_{\rm crys}$ at $\tau=0$ is 1, coming from the Fermion commutation relation. It is well known that a Fourier series of a discontinuous function will converge to the average of the two values on either side of the discontinuity, that is

$$\sum_n G_{\rm crys}(i\omega_n) = \tfrac{1}{2}\left[G_{\rm crys}(\tau=0^+) + G_{\rm crys}(\tau=0^-)\right] \tag{5.28}$$

so the extra 1/2 must be added to give the correct value.

The sum over Matsubara frequencies formally must be carried out from $-\infty$ to ∞. Of course, this cannot be done in practice on a computer, so we use the following optimization. First, we can trim the sum from 0 to ∞ by noting that $G_{\rm crys}(-i\omega_n) = G^*_{\rm crys}(i\omega_n)$, so that

$$\rho = 2T\sum_{n=0}^{\infty} \mathrm{Re}\, G_{\rm crys}(i\omega_n) + \tfrac{1}{2}I_{N_{orb}}. \tag{5.29}$$

At large ω_n, $\mathrm{Re}\, G_{\rm crys} \propto \omega_n^{-2}$ so by fitting the line $\ln|\mathrm{Re}\, G_{\rm crys}| = A + B\ln\omega_n$ to find the A coefficient the high frequency terms can be summed to infinity analytically. Also the comparison of the B coefficient to -2 gives a measure of the quality of the assumption

of frequency being "high enough" to use this kind of fit. If the expansion in (5.25) is used, then the intercept A can be computed directly as $\sum_{\mathbf{k}} S_{\mathbf{k}}^{-1} L_{\mathbf{k}}$.

The sum of this tail function is

$$\sum_{n=-\infty}^{\infty} \frac{1}{\omega_n^2} = \beta^2 \sum_{n=-\infty}^{\infty} \frac{1}{[\pi(2n+1)]^2} = \frac{1}{4}\beta^2. \tag{5.30}$$

Then we compute the density as

$$\rho = \frac{1}{2} I_{N_{orb}} + 2T \sum_{n=0}^{N_\omega} \mathrm{Re}\, G_{\mathrm{crys}}(i\omega_n) + \frac{1}{4} AT - 2AT \sum_{n=0}^{N_\omega} \frac{1}{\omega_n^2}. \tag{5.31}$$

Here, we have taken the analytic sum from 0 to ∞ of ω_n^{-2}, added the sum of the Green's function over the Matsubara frequency range used in the calculation and subtracted the sum of ω_n^{-2} over those same Matsubara frequencies. The $\frac{1}{4}AT$ term is added to each element in the matrix, not just along the diagonal. We note that this correction is rather small, since summing only 128 (positive frequency) terms in (5.30) gives $0.249604\beta^2$, a value which is converged to 3 decimal places. The choice of the actual number of Matsubara frequencies used in the calculation is determined by the temperature; a value should be chosen so that $G_{\mathrm{crys}}(i\omega_n)$ at the highest calculated frequencies does not significantly deviate from ω_n^{-2} behavior. At present, having the highest frequency at around 6 Hartrees seems to be adequate. As a rule of thumb, one should choose N_ω so that its product with T measured in K is around 10^6.

To get meaningful results, one must adjust the chemical potential μ to satisfy $N_{elec} \equiv \mathrm{Tr}(\rho) = N_{proton}$. Since the calculation of ρ requires recomputation of G_{crys} at each frequency, this is fairly expensive. So we must perform the search for μ in as intelligent a manner as possible to minimize the number of iterations performed here.

First, the correct number of electrons must be bracketed by lower and upper values of the chemical potential, μ_L and μ_H. There is in general no clear way to do this, however we are saved in this case by the fact that $N_e(\mu)$ is a monotonically increasing function.

Once the correct electron number is bracketed, then μ must be iterated to get the correct value. There are three kinds of updates used.

1. Bisection

$$\mu^B_{\text{next}} = \frac{1}{2}\left(\mu_L + \mu_H\right) \tag{5.32}$$

2. Linear interpolation

$$m = (N_H - N_L)/(\mu_H - \mu_L) \tag{5.33}$$

$$\mu^L_{\text{next}} = \mu_L + (N_p - N_L)/m \tag{5.34}$$

3. Average

$$\mu^A_{\text{next}} = \frac{1}{2}\left(\mu^B_{\text{next}} + \mu^L_{\text{next}}\right) \tag{5.35}$$

4. Quadratic Interpolation

Details in Sec. 5.4

Linear or quadratic interpolation are generally the best, however if there is a gap in the electronic structure between the two brackets, then the both methods can spectacularly fail to find the correct chemical potential. If one of the brackets is in the gap, then interpolation schemes will continually pick points inside the gap and converge very slowly. In this case doing an averaging update for a single step does very well to move the lower bracket close to the target value, so that the linear interpolation will converge must faster.

5.2.4 Computation of Crystal Green's Function

The computation of the $G_{\text{crys}}(i\omega)$ is performed simply as a straight sum over **k**-points. This is done without regards to any crystal symmetries, so to get meaningful results, one must generate **k**-points in the entire Brillouin zone, not just the irreducible zone. If this calculation could be done in the irreducible zone, perhaps by using the symmetry

operations to symmeterize the resultant $G_{\rm crys}$ then this could speed up the calculation tremendously.

The difficulty here is in understanding how exactly to apply the symmetries to an orbital-basis matrix. Symmetries are typically written as 3×3 real space matrices, perhaps with a translation vector for non-symmorphic symmetries. How to apply this transformation in a general way to a matrix written in an orbital basis is non-trivial.

Convergency with respect to **k**-point sampling could likely be improved by implementing a tetrahedron algorithm for the summation over **k**. This is not done at the moment, but I don't forsee any difficulty above and beyond the implementation of the algorithm itself.

5.2.5 Mixing

Briefly here I will describe Anderson mixing as used in my DMFT implementation. Anderson mixing seeks to minimize the difference between averaged input and output vectors, defined at iteration n by

$$\begin{aligned} |\bar{I}^{(n)}\rangle &= (1-\gamma)|I^{(n-1)}\rangle + \gamma|I^{(n)}\rangle \\ |\bar{F}^{(n)}\rangle &= (1-\gamma)|F^{(n-1)}\rangle + \gamma|F^{(n)}\rangle. \end{aligned} \tag{5.36}$$

Then the function $\Delta^{(n)} = \langle \bar{I}^{(n)} - \bar{F}^{(n)} | \bar{I}^{(n)} - \bar{F}^{(n)} \rangle$ is minimized with respect to γ. This leads to the following definitions,

$$\begin{aligned} |M^{(n)}\rangle &= |F^{(n)}\rangle - |I^{(n)}\rangle \\ |N^{(n)}\rangle &= |M^{(n)}\rangle - |M^{(n-1)}\rangle \\ \gamma &= \frac{-\,\mathrm{Re}\,\langle M^{(n-1)}|N^{(n)}\rangle}{\langle N^{(n)}|N^{(n)}\rangle} \end{aligned} \tag{5.37}$$

The input for the next iteration is then taken as

$$|I^{(n+1)}\rangle = (1-\alpha)|\bar{I}^{(n)}\rangle + \alpha|\bar{F}^{(n)}\rangle \tag{5.38}$$

where α is a mixing parameter chosen empirically, and is analogous to the mixing parameter used in simple mixing. The algorithm could be expanded to mix in iterations previous to the $(n-1)$'th iteration by introducing extra mixing variables analogous to γ. However, the mixing as it stands is satisfactory, and it is not clear whether the convergence would be significantly improved by doing this enough to justify the extra coding effort and the increase in code complexity and required memory storage.

The evaluation of the inner products above can be done in any manner which is done consistently. Some care should be taken in choosing how to perform the inner product with self-energy matrices. Since the self-energy tends to a constant value proportional to N at high frequencies, a method should be chosen which will not place too much weight on this constant value. The form of the inner product used is

$$\langle A(i\omega_n)|B(i\omega_n)\rangle = \sum_{i,j,n} A^*_{ij}(i\omega_n)B_{ij}(i\omega_n)\frac{\omega_0^2}{\omega_0^2+\omega_n^2} \tag{5.39}$$

where ω_0 is chosen at some reasonable value where Σ has not yet reached its high frequency value.

5.2.6 Charge self-consistency

Most DMFT implementations do not complete the charge self-consistent loop. In some cases this is due to using an impurity solver which is very computationally expensive, such as QMC / Hirsch-Fye. The Hubbard I impurity solver is cheap enough that charge self-consistency can be implemented. The approach described in this section could be used for a general self-energy. However, the pole expansion described in section 5.3 provides a much more straightforward means of implementing charge self-consistency with Hubbard

I in FPLO.

The density in FPLO is divided up into contributions from core-core terms, valence-valence terms, and core-valence terms.

$$n_{vv} = \sum_{\mathbf{k}} w_{\mathbf{k}} V D_{\mathbf{k}} D_{\mathbf{k}}^{\dagger} V^{\dagger} \tag{5.40}$$

$$n_{vc} = - \sum_{\mathbf{k}} w_{\mathbf{k}} V D_{\mathbf{k}} D_{\mathbf{k}}^{\dagger} S_{vc} C^{\dagger} \tag{5.41}$$

$$n_{cv} = - \sum_{\mathbf{k}} w_{\mathbf{k}} C S_{cv} D_{\mathbf{k}} D_{\mathbf{k}}^{\dagger} V^{\dagger} \tag{5.42}$$

$$n_{cc} = \sum_{\mathbf{k}} w_{\mathbf{k}} C S_{cv} D_{\mathbf{k}} D_{\mathbf{k}}^{\dagger} S_{vc} C^{\dagger}. \tag{5.43}$$

$D_{\mathbf{k}}$ is stored in the code as the variable `kohnsham%p_ccvk`. In the Kohn-Sham formalism D is the eigenvectors of the Hamiltonian, obtained from the secular equation $H_{\mathbf{k}} D_{\mathbf{k}} = \varepsilon_{\mathbf{k}} S_{\mathbf{k}} D_{\mathbf{k}}$. The weights $w_{\mathbf{k}}$ are calculated from the tetrahedron integration scheme to properly perform the sum over k in the irreducible Brillouin zone. They are stored in the code in the variable `kohnsham%p_bweitk`.

In order to trick the density computation routines defined in `density.f90` into computing the correct density from the valence occupation matrix calculated in DMFT, we need to compute values of $w_{\mathbf{k}}$ and $D_{\mathbf{k}}$ such that $\sum_{\mathbf{k}} w_{\mathbf{k}} D_{\mathbf{k}} D_{\mathbf{k}}^{\dagger} = \rho$. The most trivial way to do this is to assume the elements of $D_{\mathbf{k}}$ are entirely real, and then compute the square-root of the density matrix, giving equal weights to all k-points. In this method, $D_{\mathbf{k}}^2 = \rho$ and $w_{\mathbf{k}} = 1/N_{\mathbf{k}}$.

This method is problematic if ρ should have negative eigenvalues, which can occur in a non-orthogonal basis. In this case there is no way to compute a matrix satisfying both $D^2 = \rho$ and $D = D^{\dagger}$ because D must have complex eigenvalues. One would normally expect the density matrix to be positive semi-definite, however because the basis functions are non-orthogonal, it is possible for orbital occupations in this basis to be below 0 or above 1, albeit by only a small amount. One possible resolution for this is to diagonalize ρ and fix any negative eigenvalues to zero. As it is most probably in a well converged

calculation that any negative eigenvalues will be very small, it is unlikely that this fix have a significant impact on the result, while allowing one to compute D from the squareroot of ρ.

There is no general solution to $DD^\dagger = \rho$ unless ρ is positive semi-definite. For a concrete example, let ρ be a 1x1 matrix with the single element -1. It is impossible to find a complex number z such that $zz^* = -1$. Conversely, for any matrix A, the matrix $AA^\dagger$ is always positive semidefinite.

There is an extra degree of freedom which has been ignored above, namely the weights $w_{\mathbf{k}}$. Through a suitable choice of $w_{\mathbf{k}}$ and $D_{\mathbf{k}}$ matrices, it should be possible to find a solution to $\sum_{\mathbf{k}} w_{\mathbf{k}} D_{\mathbf{k}} D_{\mathbf{k}}^\dagger = \rho$ for all possible ρ. However, a clear perscription for doing this is not obvious. Unless the number of $\mathbf{k}$-points is very small, then it is likely that there are many more degrees of freedom here than necessary. Since any solution should be acceptable, the key to using this approach is to find a solution which is numerically robust.

5.3 Pole Expansion of Self-Energy

Using a numerical representation of the self-energy is very computationally expensive as it requires a matrix inversion for every k-point, every Matsubara frequency at every chemical potential checked when searching for the particle number. A much faster algorithm can be developed if the self energy can be represented as a sum of poles, ie.

$$\Sigma_{ab}(\omega) = \Sigma_\infty + \sum_{i=1}^{N_{\text{pole}}} \frac{W_{ai}^\dagger W_{ib}}{\omega - P_i} \tag{5.44}$$

where W_{ai} applies an appropriate weighting factor. For this section, we assume Σ_∞ includes any necessary double-counting correction.

The problem can be linearized with respect to frequency by using the matrix inversion

identity

$$\begin{bmatrix} (\omega+\mu)S_{\mathbf{k}} - H_{\mathbf{k}} - \Sigma_\infty & W^\dagger \\ W & \omega - P \end{bmatrix}^{-1} = \begin{bmatrix} [(\omega+\mu)S_{\mathbf{k}} - H_{\mathbf{k}} - \Sigma(\omega)]^{-1} & \cdots \\ \vdots & \ddots \end{bmatrix} \tag{5.45}$$

where the matrix P is a diagonal matrix with the poles P_i along the diagonal. Because the left hand side in (5.45) is linear in frequency, rather than invert the matrix at each frequency we can solve an eigenvector problem to invert the matrix. If we define

$$L_{\mathbf{k}} = \begin{bmatrix} H_{\mathbf{k}} + \Sigma_\infty & W^\dagger \\ W & P \end{bmatrix} \tag{5.46}$$

$$O_{\mathbf{k}} = \begin{bmatrix} S_{\mathbf{k}} & 0 \\ 0 & I \end{bmatrix} \tag{5.47}$$

then solve the generalized eigenvalue problem $L_{\mathbf{k}}|\psi_{\mathbf{k}m}\rangle = \varepsilon_{km} O_{\mathbf{k}}|\psi_{\mathbf{k}m}\rangle$, then a transformation to the basis of eigenvectors can be done with the unitary matrix $c_{ij}^{\mathbf{k}} = (\psi_{\mathbf{k}i})_j$. Then the Green's function for the net population associated with the matrix $L_{\mathbf{k}}$ can be calculated via

$$G_{ij}^L(\omega) = \sum_{\mathbf{k}m} \frac{c_{im}^{\mathbf{k}*} c_{mj}^{\mathbf{k}}}{\omega + \mu - \varepsilon_{\mathbf{k}m}}. \tag{5.48}$$

Actually, there is no real need to calculate the Green's function directly. With the pole expansion, from Hubbard I the occupation matrix can be evaluated analytically, since $\sum_n [i\omega_n + \mu - \varepsilon]^{-1} = f(\varepsilon - \mu)$, the Fermi function. This way, the net occupation of the i-th orbital can be calculated as

$$N_{i,\text{net}} = \sum_{\mathbf{k}m} c_{im}^{\mathbf{k}*} c_{mi}^{\mathbf{k}} f(\varepsilon_{\mathbf{k}m} - \mu) \tag{5.49}$$

and the gross occupation is

$$N_{i,\text{gross}} = \sum_{\mathbf{k}mj} c^{\mathbf{k}*}_{im} (O_{\mathbf{k}})_{ij} c^{\mathbf{k}}_{mj} f(\varepsilon_{\mathbf{k}m} - \mu) \tag{5.50}$$

This formalism increases the size of the "effective Hamiltonian" $L_{\mathbf{k}}$ and the Green's function by the number of poles in the expansion. The elements in the $N \times N$ LDA Hamiltonian and its eigenvectors correspond to specific orbitals. The first N elements in the $L_{\mathbf{k}}$ and G^L matrices correspond to these same orbitals, however there are N_{pole} extra "orbitals" which correspond the poles that were added. These orbitals don't have any physical significance, so the section of the Green's function corresponding to these orbitals can be ignored. The increased size of $L_{\mathbf{k}}$ also means there will be extra bands, (each eigenvalue/vector pair corresponds to a band) but since the elements that correspond to the pole states don't have physical significance, each band will not contribute an integral number of electrons to the orbitals.

The implementation of this approach in FPLO provides a more straightforward means of implementing charge self-consistency than the numerical approach. The diagonalization of of $L_{\mathbf{k}}$ provides the right eigenvectors, and the code is already situated to handle eigenvectors for a differing number of bands than the number of valence orbitals.

5.4 Parabolic Guess for Chemical Potential

The purpose of this section is to briefly describe how to choose an input value for an algorithm based on a parabolic fit to three points given a target output value. The three points will be labeled with ordered (x_i, y_i) pairs, so that $x_i < x_(i+1)$.

First we define a coordinate system where a point is chosen to be the origin. For concreteness, this will be the $i = 0$ point, but there is no loss of generality in making this

choice. This local coordinate system is given by

$$s_i = x_i - x_0 \tag{5.51}$$

$$t_i = y_i - y_0. \tag{5.52}$$

We fit an equation of the form $t = as^2 + b's$ with the following matrix multiplication

$$\begin{pmatrix} a \\ b' \end{pmatrix} = \frac{1}{s_1^2 s_2 - s_1 s_2^2} \begin{pmatrix} s_2 & -s_1 \\ -s_2^2 & s_1^2 \end{pmatrix} \begin{pmatrix} t_1 \\ t_2 \end{pmatrix} \tag{5.53}$$

then an equation of the form $y = ax^2 + bx + c$ can be formed by calculating

$$b = b' - 2ax_0 \tag{5.54}$$

$$c = ax_0^2 - b'x_0 + y_0 \tag{5.55}$$

and a guess value for x given a target value y_t, can be calculated via

$$x = \frac{-b}{2a} \pm \frac{1}{2a}\sqrt{b^2 - 4a(c - y_t)}. \tag{5.56}$$

One of the two possible guess values is chosen based on whether or not it's between the two points which bound the target value.

Part II

Applications

Chapter 6

Wannier Functions in $LiNbO_2$

The work described in this chapter was done in collaboration with Warren E. Pickett and published in reference [26].

6.1 Introduction

The quasi-two-dimensional (2D) compound $LiNbO_2$ has become of interest in condensed matter studies in no small part due to the existence of superconductivity[82] in the delithiated phase Li_xNbO_2. This system consists of a triangular lattice of transition metal (niobium) ions separated by layers of O ions from 'blocking' (Li) layers, thus possessing structural similarities to high temperature superconducting cuprates. Important differences from the cuprates include the presence of a $4d$ rather than $3d$ ion, and of course the triangular rather than square lattice. The trigonal prismatic coordination of Nb with six O atoms causes the valence band to be composed solely of Nb d_{z^2} states. Other d states are well separated by a 2 eV gap, leaving only a single band per formula unit required for analysis. The comparative structural simplicity of $LiNbO_2$ makes it attractive for theoretical studies, especially as it requires modest computational time to characterize its properties.

This alkaliniobate is also of interest due to the increasing attention garnered by nio-

bates in recent years.[83] The three-dimensional $LiNbO_3$ is an important and well studied ferroelectric material.[84] Superconductivity at $T_c \sim 20$ K has been reported by a few groups[85, 86, 87] in the barium niobate system. The phase has not been positively identified but it has been suggested to be a nonstoichiometric $BaNbO_x$ cubic perovskite. Superconductivity in the 5-6 K range has been reported in the Li-intercalated layered perovskite system $Li_xAB_2Na_{n-3}Nb_nO_{3n+1}$ [A = K, Rb, Cs; B = Ca, Sr, Ba; $n = 3$ and 4].[88, 89] This system has clear structural motifs in common with the peculiar $Nb_{12}O_{29}$ system, where the 'single O^{2-} deficiency' (with respect to insulating $Nb_2O_5 = Nb_{12}O_{30}$) releases two carriers into the cell; one localizes and is magnetic while the other is itinerant and results in conducting behavior.[90, 91]

While there is good agreement as to structure type and lattice parameters of the stoichiometric phase $LiNbO_2$, there is some disagreement in the literature as to its electronic and magnetic properties. Originally it was reported as being paramagnetic with strong field dependence,[92] however calculations predict it to be a diamagnetic semiconductor. [93] Other experimental work suggests that it is diamagnetic, and strongly field-dependent paramagnetic properties are the result of impurities.[94] The values of the band gap are also in mild dispute. Extended Hückel calculations with a single isolated NbO_2 layer give a bandgap value of 1.4 eV, [93] and full potential linear muffin tin orbital calculations with the full crystal structure of $LiNbO_2$ give 1.5 eV.[95] Measured optical reflectance shows an onset at ~ 2 eV, which is suggested to be a direct bandgap responsible for the burgundy-red color of $LiNbO_2$.[94] Band structure calculations given here and by Novikov *et al.*[95] are in agreement that $LiNbO_2$ is a direct gap semiconductor.

Geselbracht *et al.*[82] first reported that the de-lithiated phases Li_xNbO_2 with $x = 0.45$ and $x = 0.50$ support superconductivity at temperatures below 5.5 K and 5 K, respectively. Moshopoulou, Bordet and Capponi[96] later reported samples with x ranging from 0.69 to 0.79 showing the onset of the Meissner effect at 5.5 K, but samples with $x = 0.84$ and above do not exhibit any superconducting transition down to 2 K. Superconductivity has also been reported in hydrogen-inserted H_xLiNbO_2, in which both samples reported had

the same $T_c = 5.5$ K for $x = 0.3$ and $x = 0.5$. [97]

Removal of Li has the effect of adding holes to the conduction band made up of Nb d_{z^2} states. As mentioned above, there does not appear to be any notable dependence[82, 96] of T_c on the concentration of Li in the range $0.45 < x < 0.8$. Such concentration independence has also been observed in the 2D electron-doped system[98, 99] Li_xZrNCl. For a phonon-paired superconductor with cylindrical Fermi surfaces this behavior is understood in terms of phase space restrictions on phonon scattering processes[100] in 2D. The independence of T_c on carrier concentration in this system is quite surprising however, since the density of states (DOS) plots presented here and by Novikov *et al.*[95] vary strongly with energy, whereas parabolic bands lead to a constant DOS in 2D. There has also been some work done investigating the ion mobility of $LiNbO_2$ to assess its potential usefulness as a battery material.[94, 101]

In this work we study the electronic structure and bonding of stoichiometric $LiNbO_2$ using density functional theory in the local density approximation (LDA). Density functional perturbation theory is used to obtain zone center phonons and Born effective charges. The structure contains a single parameter z that specifies the position of the O layers relative to the Li and Nb layers, and which seems to be of particular importance in understanding the electronic bonding and electron-phonon coupling in this compound. We investigate the corresponding Raman active vibrational mode (beating oscillation of the O planes) and the effect this has on the band structure. We obtain a tight-binding (TB) model that involves many neighbors and helps one to understand how this variation affects interactions between the Nb atoms. Many aspects of the electronic structure, such as chemical bonding and effective charges, can be seen to be interrelated by examining the Wannier functions of the valence bands.

6.2 Structure

Structural information of $LiNbO_2$ has been reported by several experimental groups, leading to the assignment of space group $P6_3/mmc$ (No. 194), with Li occupying sites 2a (0,0,0) with symmetry $\overline{3}m$, Nb occupying sites 2d $(\frac{2}{3}, \frac{1}{3}, \frac{1}{4})$ with symmetry $\overline{6}m2$, and O occupying sites 4f $(\frac{1}{3}, \frac{2}{3}, z)$ with symmetry $3m$. The O sites include an internal parameter z specifying their height relative to the Li layer along the c-axis. The Li sites are centers of inversion; the Nb sites have z-reflection symmetry in addition to the $3m$ triangular symmetry within the layer but do not lie at centers of inversion.

There is good experimental agreement on lattice parameters, $a = 2.90$Å, $c = 10.46$Å. [96, 94, 92] The distance a between Nb atoms is quite close to the nearest neighbor distance of 2.86 Å in elemental bcc Nb, suggesting that direct Nb-Nb coupling should be kept in mind. However, Nb^{3+} $4d$ orbitals will be smaller than in neutral Nb. In later sections, we will discuss details of the Nb-O interactions, and show that the electronic properties of $LiNbO_2$ are very sensitive to changes in the Nb-O distance. The vertical distance between Nb and O planes can be calculated by $(\frac{1}{4} - z)c$, and the distance between Nb and O atoms is given by $\sqrt{\frac{2}{9}a^2 + (\frac{1}{4} - z)^2 c^2}$.

Some disagreement exists about the value of z. A larger value of z indicates the O layers are closer to the Nb layers. Meyer and Hoppe[92] found $z = 0.1263$, Moshopoulou, Bordet and Capponi[96] report $z = 0.128$, Geselbracht, Stacy, Garcia, Slibernagel and Kwei[94] report $z = 0.12478$, Tyutyunnik, Zubkov, Pereliaev and Kar'kin[102] report $z = 0.1293$. These variations amount to a difference in O layer position of about 0.05Å.

Optimization of unit cell geometry within LDA leads to $a = 2.847$Å, $c = 10.193$ Å, $z = 0.1211$. This differs from the measured value by $\Delta a \approx -1.8\%$, $\Delta c \approx -2.5\%$, for a total volume discrepancy of $\Delta V/V \approx -6\%$. The calculated overbinding of the unit cell is somewhat larger than is typical in LDA calculations, perhaps due to the low (practically zero) valence electron density in the Li layer. In this regard, we note that our Nb pseudopotential does not include the $4p$ states in the valence bands, which may have

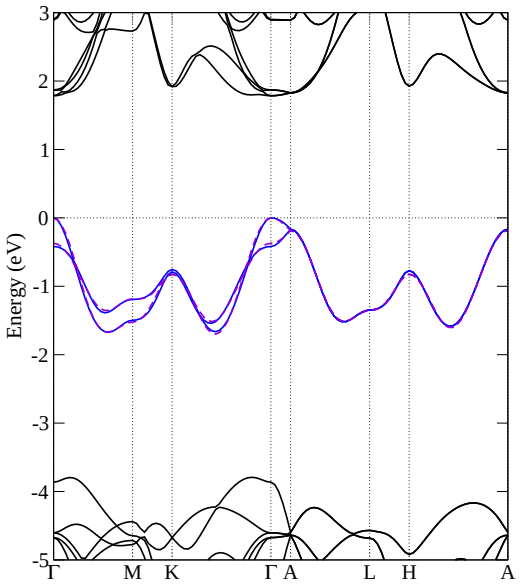

Figure 6.1: (Color online) Band structure for $LiNbO_2$ with O height $z = 0.1263$ typical of the slightly scattered experimental results. Two Nb bands (one per Nb layer) lie within a 5.5 eV gap between the O $2p$ bands below and the remaining Nb $4d$ bands above. The tight binding fit of Table 6.1 is shown with a dashed line.

some effect on structural properties. Optimization with respect to z, holding the lattice parameters a and c fixed at experimental values gives $z = 0.125$, which is very close to the value of Geselbracht *et al.*[94]

6.3 Electronic Structure Calculations

The present results have been obtained through the use of the ABINIT code.[103] The lattice constants and the parameter z given by Meyer and Hoppe[92] were used in the calculations in this section. Pseudopotentials used were LDA, Troullier-Martins type,[18] generated using the Perdew-Wang LDA exchange-correlation functional.[13] A self-consistent density was generated with 36 irreducible **k**-points, which was then used to calculate energies at 116 **k**-points along high symmetry directions to plot the band structure. The kinetic energy cutoff for the planewave basis was set to 40 Hartrees.

Figure 6.1 of the important region of the band structure shows the top of the O $2p$

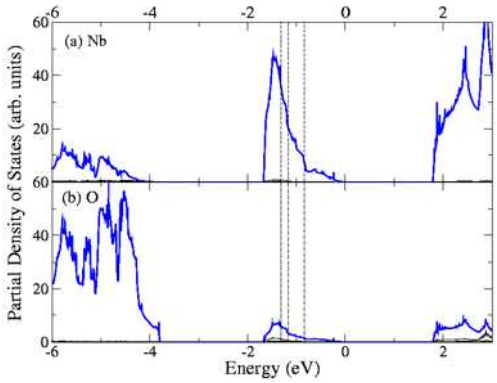

Figure 6.2: (Color online) Density of states for Nb and O atoms. For $LiNbO_2$, states are occupied up to energy $E = 0$. The dominant states in the valence band for Nb are $4d$-orbitals, and for O they are $2p$-orbitals. Dashed vertical lines are included to indicate the Fermi energy in the rigid band picture for Li_xNbO_2 for concentrations $x = 0$ (half-filled band), $x = 0.4$, $x = 0.8$ from left to right. The last two values of x roughly bracket the concentrations where superconductivity is observed.

bands, a 2 eV gap to two Nb $4d$ bands which are the highest occupied bands, and another 2 eV gap to the conduction bands. The band gap, direct at the Γ point, is 1.9 eV, somewhat higher than the 1.5 eV reported by Novikov *et al.* (also at the Γ point) using the full potential linear muffin-tin orbital method (FLMTO) with the same structural parameters.[95] LDA calculations often underestimate band gaps, so we conclude that it is most likely the experimental band gap is somewhat larger than 2 eV. Measured optical absorption suggests that the band gap should be around 2 eV,[94] which is consistent with the reported dark reddish color.[94, 92]

Projected density of states (DOS) calculations, presented in Fig. 6.2 were done using the tetrahedron method projecting to atomic spheres with radii of R(Li) = 1.7 a.u., R(Nb) = R(O) = 2.0 a.u. These calculations confirm that the uppermost valence bands are largely Nb $4d$ character, with roughly 15% contribution from O $2p$ states, and virtually none from Li states. These projected DOSs are consistent with those calculated by Novikov *et al.*[95] The trigonal crystal field splitting of the Nb $3d$ states results in the d_{z^2} orbital energy centered 4 eV below the other Nb $4d$ states (two e_g doublets, based on $\{xz, yz\}$ and $\{x^2 - y^2, xy\}$). The unit cell contains two symmetry-related Nb layers which result in the

presence of two Nb d_{z^2} bands in the band plot. The splitting of the bands along Γ-M-K-Γ reflects the strength of interaction between layers, as discussed below.

As a result of the large trigonal crystal field splitting, the Nb d_{z^2} state forms a single band, triangular lattice system of the type that is attracting renewed interest. The calculated DOS in Fig. 6.2 has only a vague resemblance to the nearest neighbor TB model (see for example Honercamp[104]) making it evident that longer range hopping must be important. We address this question in detail in section 6.6.

This general electronic structure, when hole-doped, is rather remarkable. It is a *bona fide* representation of a single band system on a triangular lattice, moreover the band is well isolated from other bands. Although single band models are widely used to investigate concepts and to model many-body effects, there are very few actual realizations in real solids. The value of the effective Coulomb on-site repulsion U for Nb^{3+} is not established, but with $W < 1.75$ eV it will not require a very large value to lead to correlated behavior. The hole-doped system Li_xNbO_2 provides a unique platform for the detailed comparison of single band models with experimental data, which for thermodynamic properties and for spectroscopic data below 2 eV should involve only the single active band.

6.4 Zone Center Wave functions

We can examine Kohn-Sham wavefunctions to gain insight into the electronic structure. Shown in Fig. 6.3 are isosurface plots of the Γ wavefunctions for the lower and upper valence bands. Both plots reveal the d_{z^2}-character of the bands on the Nb atoms, as well as $2p_z$ bonding contributions from the O atoms. For the upper band, the p-lobes have more weight away from the sandwiched Nb layer, indicating the weight of bonding with O is somewhat decreased. The change in sign between the two Nb layers in Fig. 6.3b indicates the presence of a nodal plane in the Li layer arising from the wavefunction's antibonding character (with respect to interlayer coupling).

The presence of an interesting triangular shape of the wavefunction around the waist

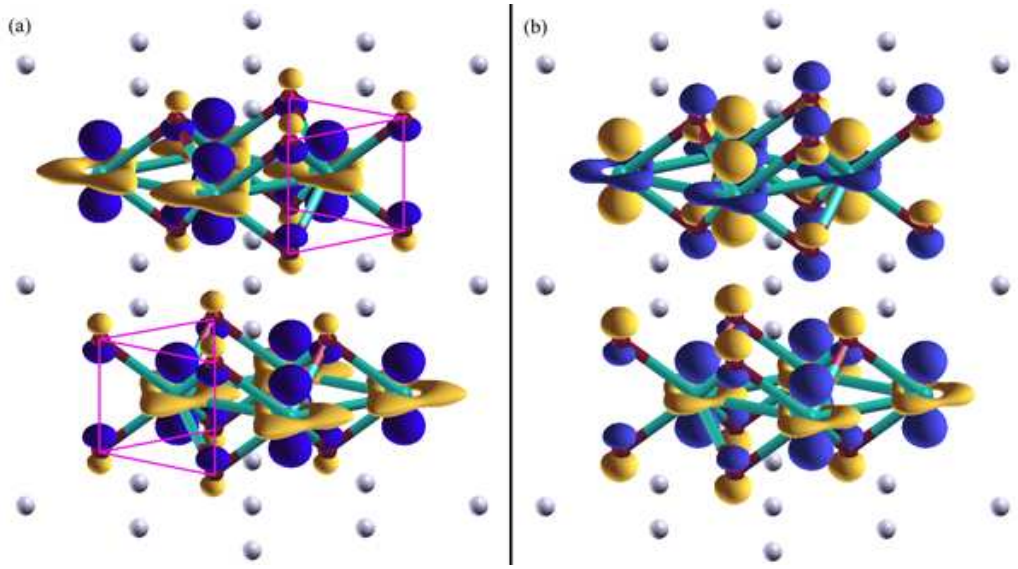

Figure 6.3: (Color online) Isosurface plot of the Γ-pt wavefunctions for $LiNbO_2$ for (a) the lower of the pair of valence bands, and (b) the upper valence band, made with XCrysDen.[105] Both wavefunctions are generated with the same isosurface value. Nb atoms are turquoise (grey), O atoms are dark red (dark gray), Li are light gray. Yellow and blue (light and dark) indicate opposite signs of the wavefunction. The z^2 symmetry around the Nb atom is apparent as well as the contribution to the bonding made by the O atoms. Trigonal prisms with O atoms at the corners and Nb atoms in the center have been outlined as a guide to the eye.

of the Nb atoms is more unexpected, being noticeably larger for the bonding function. The corners of these triangles do not point toward nearest neighbors, instead they point toward interstitial holes in the Nb layer which are not directly sandwiched between O atoms. This shape reflects either three-center Nb-Nb bonding, which would result in an increased density in this region, or antibonding character of direct Nb-Nb interactions that would decrease the density along the directions connecting Nb atoms. The character and origin of this triangular 'waist' around Nb atoms are clarified in the following section.

6.5 Wannier Function

A single isolated band also provides an unusually clean system for performing the transformation from reciprocal space (bands) to real space (bonds) to look at character and

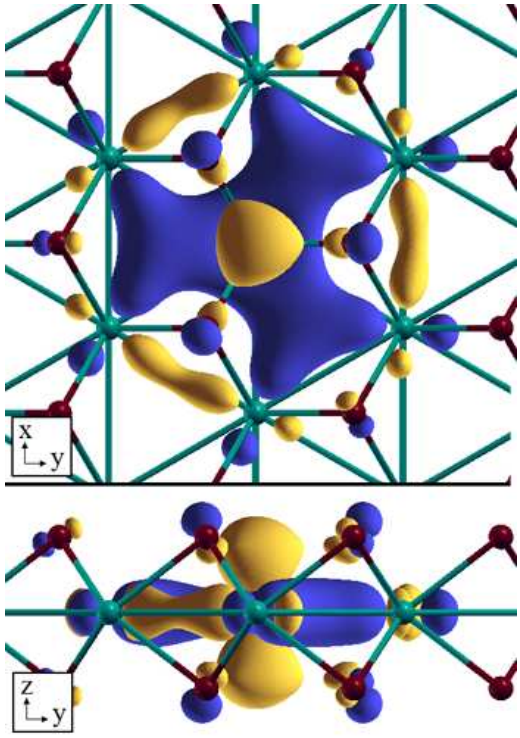

Figure 6.4: (Color online) Isosurface plot of the Wannier function for $LiNbO_2$, made with XCrysDen.[105] Niobium atoms are turquoise (gray), O atoms are dark red (dark gray), Li not pictured. Yellow and blue indicate opposite signs of the WF. The z^2 symmetry around the central atom is apparent, as well as the $xy/x^2 - y^2$ character around nearest neighbors, which maintains the orthogonality of WFs centered on different atoms.

strength of interatomic interactions from a local viewpoint. The straightforward way of doing this is to generate Wannier functions (WFs) defined by

$$|\mathbf{R}m\rangle = N_{\mathbf{k}}^{-1/2} \sum_{\mathbf{k},n} U_{mn}^{\mathbf{k}} e^{-i\mathbf{k}\cdot\mathbf{R}} |\mathbf{k}n\rangle \tag{6.1}$$

where $U^{\mathbf{k}}$ can be any unitary matrix, and $N_{\mathbf{k}}$ is the number of k-points used in the summation. The orthonormal Bloch states are denoted by $|\mathbf{k}n\rangle$. If there were only one NbO_2 layer per cell, hence only one band, $U(\mathbf{k})$ would be simply a complex number of unit modulus. Here it is a 2×2 matrix in the band space, which gives rise to very modest extra complexity. These WFs display orthonormality $\langle \mathbf{R}m|\mathbf{R}'m'\rangle = \delta_{\mathbf{R},\mathbf{R}'}\delta_{m,m'}$. Once a choice for $U^{\mathbf{k}}$ is made, this approach generates a basis set of identical WFs for each point

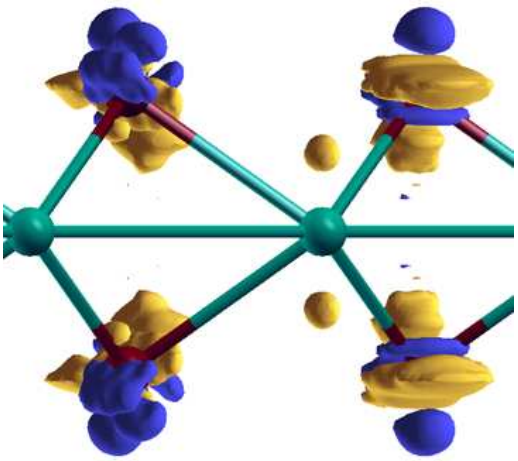

Figure 6.5: (Color online) Isosurface plot of the difference $|W_{z=0.1359}(\mathbf{r})| - |W_{z=0.1263}(\mathbf{r})|$, looking along the [010] cartesian direction. Yellow (light gray) is the positive isosurface and blue (dark gray) is negative, with Nb atoms in turquoise (gray) and O atoms in dark red (dark gray). As the O atoms are moved closer to the Nb layer, there is an increase in density above and below the Nb atom; in addition the contributions from the O-p orbitals appear to tilt more towards the central Nb atom.

in the Bravais lattice of the system being studied.

We have chosen the unitary matrix U such that $U = M(M^\dagger M)^{-1/2}$ with $M_{mn} = \langle \mathbf{k}n|S_m\rangle$ where $|S_m\rangle$ are a set of atom-centered functions with the desired d_{z^2}symmetry. This technique has been used previously in the study of magnetic ordering in cuprates.[25] Choosing $|S_m\rangle$ as hydrogenic $4d_{z^2}$ orbitals centered on the Nb atoms for the two entangled valence bands gives a pair of identical WFs for each Nb bilayer in the unit cell, based on the Nb d_z^2 symmetry that was also observed in the Γ-point wavefunction. An $8 \times 8 \times 4$ mesh totaling 256 k-points was used to generate the WF shown in Fig. 6.4. Increasing the size of the mesh does not change the visual appearance of the WF.

The WF naturally displays the prominent lobe along the $\pm\hat{z}$ axis that is characteristic of the $3z^2 - r^2$ function. It also contains p_σ contributions from the nearest O ions, as well as smaller but still clear $2p$ amplitude on the second neighbor O ions that is approximately p_π. Here p_σ denotes the combination of p_x, p_y, p_z functions oriented toward the reference Nb atom, while p_π is perpendicular. The p_σ lobe nearest the Nb ion has the same sign as

the $3z^2 - r^2$ lobes along the $\hat{z}$ axis.

The in-plane part of the WF reveals more about the bonding in $LiNbO_2$. The ring-structure of the $3z^2 - r^2$ function in the $x - y$ plane connects with combinations of xy and $x^2 - y^2$ functions on the three neighboring Nb ions to form a substantial in-plane windmill structure with three paddles, which are oriented between the z-projections of the neighboring O ions. A "$3z^2 - r^2$" symmetry WF has the full D_{3h} symmetry of the Nb site, which allows a contribution of an appropriate combination of $x^2 - y^2$ and xy atomic orbitals, and the windmill structure reflects the bonding of such functions on neighboring Nb ions. Thus the $4d$ character is not entirely d_{z^2}, which clarifies the threefold symmetric shape around the Nb waist in the $\mathbf{k} = 0$ wavefunction discussed in the previous section.

In addition, there is a 'hotdog' structure of opposite sign connecting pairs of nearest-neighbor Nb ions. Of the two types of Nb-Nb pairs, these hotdogs lie nearest to the first neighbor O ions. Small nearest-Nb "backbonds" in the $x - y$ plane of both the windmill arms and the hotdogs are also evident. As we note below, the WF contains information about the Nb-Nb hopping parameters. The more distant parts of the WF function are a direct reflection of the existence of such longer range interaction.

This Nb $4d_{z^2}$ WF is similar to that for Ta $5d_{z^2}$ in isostructural $TaSe_2$.[106] A difference is that the nearest neighbor O $2p$ orbitals contribute more significantly to the bonding in $LiNbO_2$, giving a larger nearest neighbor hopping. The d_{z^2} lobes above and below the transition metal appear to be somewhat more pronounced in $TaSe_2$. We also observe changes toward such appearance in this Nb WF as the O layer height (z) is increased, forcing the O atoms closer to the Nb layers and increasing t_1. Given in Fig. 6.5 is a plot of the *difference* in the magnitudes of the WFs taken for the two different z values of 0.1359 and 0.1263 (O displacements of roughly 0.1 Å.) There is an increase in the density of the d_{z^2} lobes above and below the transition metal as well as a tilting of the O orbitals toward the central site, as the Nb-O distance is reduced. Correlating this with the tight binding results from the next section suggests there is an increase in the role the O atoms play in the hopping to nearest neighbors as the Nb-O distance is decreased. The opposite effect

occurs when $z = 0.1167$; the O orbitals tilt to become oriented more along the z-direction, indicating the O atoms are interacting less strongly with Nb.

6.6 Tight Binding

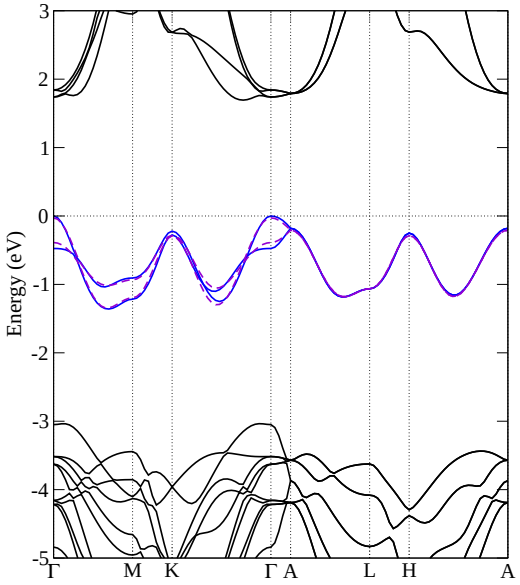

Figure 6.6: (Color online) Band structure for O layer position $z = 0.1167$, a larger Nb-O layer separation by 0.1 Å compared to the bands in Fig. 6.1. The band width is 25% smaller, and band gap is significantly less, compared to the experimental structure ($z = 0.1263$).

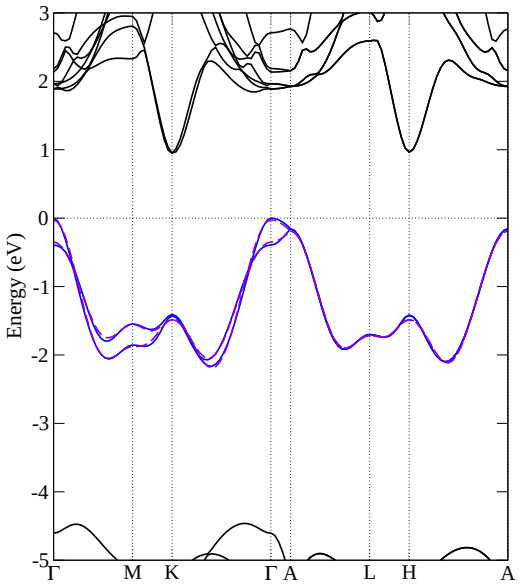

Figure 6.7: (Color online) Band structure for O layer position $z = 0.1359$, about 0.1 Å closer to the Nb layer than in experiment (Fig. 6.1). The bandwidth is 15% larger than for the experimental structure, and the peaks at M and K in the valence band are similar to the band structure calculation of $Li_{0.5}NbO_2$ shown by Novikov *et al.*,[95] suggesting that the underlying electronic structure of Li_xNbO_2 is determined by the position of O layers rather than the Li concentration.

z	d_{Nb-O}	Bandwidth	Band Gap	t_1	t_2	t_3	t_4	t_5	$t_1^\perp$	$t_2^\perp$	$t_3^\perp$	$t_4^\perp$	$t_5^\perp$
0.1167	2.178	1.36	1.69	19	**102**	10	-10	6	18	-23	-5	-7	-1
0.1263	2.116	1.67	1.78	64	**100**	33	-13	8	18	-21	-5	-6	-8
0.1359	2.056	2.17	1.89(0.95)	**122**	94	56	-17	9	18	-19	-3	-6	-8
2H-$TaSe_2$		1.9		38	**115**				29	23			

Table 6.1: Tight binding hopping parameters for three values of the O internal structural parameter z. Hopping parameters are reported in meV; bandwidths and band gaps are reported in eV. Distance between Nb and O atoms are reported in angstroms. The largest hopping coefficients are in boldface. Squeezing the O layers closer to the Nb layers ($z = 0.1359$) results in a dramatic increase in t_1, making it larger than t_2, and a large change in t_3 as well. For $z = 0.1359$, the band gap is indirect. The direct gap at Γ is listed followed by the indirect gap in parentheses. See figure 6.7. $t_3^\perp$ is slightly refined, to make the splitting at Γ agree with the DFT result better.

The valence bands seen in Fig. 6.1 are well isolated from bands above and below. These bands contain the superconducting electrons in de-lithiated Li_xNbO_2, so a simplified tight binding fit using only these bands would be useful in doing studies on simple models. The TB model to fit two bands corresponding to identical Nb d_{z^2}-O p hybridized Wannier functions on the two Nb atoms per cell gives dispersion relations from the roots of

$$0 = \begin{vmatrix} \varepsilon^{\parallel}_{\mathbf{k}} - \varepsilon_{\mathbf{k}} & \varepsilon^{\perp}_{\mathbf{k}} \\ \varepsilon^{\perp}_{\mathbf{k}} * & \varepsilon^{\parallel}_{\mathbf{k}} - \varepsilon_{\mathbf{k}} \end{vmatrix} \Longrightarrow \varepsilon_{\mathbf{k}} = \varepsilon^{\parallel}_{\mathbf{k}} \pm |\varepsilon^{\perp}_{\mathbf{k}}| \tag{6.2}$$

where $\varepsilon^{\parallel}_{\mathbf{k}}$ arises from the hopping processes within a plane of atoms and $\varepsilon^{\perp}_{\mathbf{k}}$ from hopping between planes. Within the plane of the triangular lattice, the nearest neighbor dispersion for the six nearest neighbors is

$$\varepsilon^{\parallel}_{\mathbf{k}} = 2t \left[\cos(k_x a) + 2\cos\left(\frac{1}{2}k_x a\right) \cos\left(\frac{\sqrt{3}}{2}k_y a\right) \right]. \tag{6.3}$$

We have found that a good fit to the Nb d_{z^2} bands requires several neighbors. Third and fifth neighbors in the plane can be included with this form by noticing odd neighbors just require a larger lattice constant. Second neighbors require a larger lattice constant and a 30° rotation. There are twelve fourth neighbors, which can be treated as two lattices with separate rotations.

First and second neighbors in adjacent layers can be included with terms of the form

$$\begin{aligned} \varepsilon^{\perp}_{\mathbf{k}} = 2\cos\frac{k_z c}{2} \Bigg\{ & 2t^{\perp}_1 \left[\cos\left(\frac{k_x a}{2}\right) e^{\frac{ik_y a}{2\sqrt{3}}} + e^{\frac{ik_y a}{\sqrt{3}}} \right] + \\ & 2t^{\perp}_2 \left[\cos\left(k_x a\right) e^{-\frac{ik_y a}{\sqrt{3}}} + e^{\frac{-i2k_y a}{\sqrt{3}}} \right] \Bigg\}. \end{aligned} \tag{6.4}$$

It is worth noting that on the zone surface (where $k_z = \pm\frac{\pi}{c}$), all terms in $\varepsilon^{\perp}_{\mathbf{k}}$, including further neighbors neglected from Eq. (6.4) are identically zero, resulting in exact degeneracy of the two valence bands at these zone surfaces.

Using the Wannier basis given in the previous section, the hopping parameters can be

directly calculated (rather than fit) as matrix elements of the LDA Hamiltonian:

$$t_{|R|,m} = \langle \mathbf{R}m|\hat{H}|\mathbf{0}m\rangle, \quad m = 1, 2; \tag{6.5a}$$

$$t^{\perp}_{|R|,m,m'} = \langle \mathbf{R}m'|\hat{H}|\mathbf{0}m\rangle. \tag{6.5b}$$

Using the definition of the WF along with orthogonality of the eigenfunctions, Eqs. (6.5) reduce to

$$t_{|R|,m} = N_{\mathbf{k}}^{-1} \sum_{\mathbf{k}n} \varepsilon_{\mathbf{k}n} |U^{\mathbf{k}}_{mn}|^2 e^{i\mathbf{k}\cdot\mathbf{R}} \tag{6.6a}$$

$$t^{\perp}_{|R|,m,m'} = N_{\mathbf{k}}^{-1} \sum_{\mathbf{k}n} \varepsilon_{\mathbf{k}n} (U^{\mathbf{k}}_{m'n})^* U^{\mathbf{k}}_{mn} e^{i\mathbf{k}\cdot\mathbf{R}}. \tag{6.6b}$$

where $\mathbf{R}$ is the difference in centers of the WFs. Deviation of a perfect representation of the bands arises only from approximation of the summation in Eq. (6) or neglect of further neighbors.

The results of the tight-binding calculation are presented in Table 6.1, as calculated from a $12\times12\times6$ Monkhorst-Pack grid of $\mathbf{k}$-points for various values of z, along with values for 2H-$TaSe_2$ as given in Ref. [106]. Remarkably, the *second* neighbor hopping integral t_2 is the dominant contribution for $z \leq 0.1263$. Also notable is the strong dependence of first and third neighbor hoppings, t_1 and t_3, on the Nb-O distance, which causes t_1 to become largest for z somewhat greater than 0.1263. The other parameters in the table are all relatively independent of the Nb-O distance. The third and beyond interplane hoppings may appear small, but they must be compared keeping in mind that there are twice as many third and fourth interplane neighbors as first and second. Since $t^{\perp}_1 \sim 2t^{\perp}_3 \sim 2t^{\perp}_4$, even these long distance hoppings are relevant. Indeed, it is not possible to get good agreement in the band splittings at the points Γ, M, K, and the minimum between K and Γ without five interplane hopping parameters (four for $z = 0.1167$).

The TB model for $z = 0.1167$ is strongly dominated by the second neighbor interactions between the Nb atoms, with other hoppings roughly an order of magnitude smaller. If t_2

were the only hopping parameter present, the system would consist of three disjoint sublattices and thus states would be threefold degenerate (although it would not be obvious on the standard band plot). Including t_1 as a perturbation would couple them weakly and remove degeneracies. In this case, the unit cell of the system could be taken as the second-neighbor lattice and the Brillouin zone would be folded back so that the K(H) point in the band plots shown is mapped onto the Γ(A) point. The result of this folding back (and the splitting that occurs because of non-zero t_1), is evident in Fig. 6.6, in that the eigenenergy of the H point is nearly the same as for the A point. The M(L) point is mapped onto itself, and the minimum between Γ(A) and M(L) is mapped onto the K(H) point, which results in a band structure that looks very much like a $\sqrt{3}$ larger triangular lattice with only nearest neighbor hopping. Similar dominance of 2nd neighbor hopping has been observed for 2H-$TaSe_2$. [106] Those authors relate their small value for t_1 to phase cancellation of Wannier functions centered at first nearest neighbors, whereas in-phase contributions at second-neighbors give a large t_2 matrix element.

For $z = 0.1359$, we find that the nearest neighbor interaction becomes dominant. From Table 6.1 and Fig. 6.5 we see that the increase in hybridization of the O anion p-state in $LiNbO_2$ as the Nb-O distance is decreased plays a significant role in first neighbor hopping, while at the same time this hybridization is rather insignificant in second neighbor hopping. This behavior suggests that a significant contribution to the hopping integrals comes from within the Nb planes, perhaps through the hotdog structure noted in the previous section. The band structure in this case looks similar to that of $Li_{0.5}NbO_2$, calculated by Novikov *et al.*,[95] especially in the magnitude of the variations around the M and K points, relative to the bandwidth. Their result shows some splitting of the bands occurring at the zone surface (along the lines A-L-H-A), which may arise from the two Nb sites becoming inequivalent due to the removal of one Li atom. If the Nb sites were kept equivalent as the Li is removed, such as in the virtual crystal approximation, then the similarities between the band structures suggest that the main impact on the electronic structure is captured by changing the Fermi energy and allowing the O layers to move closer to the Nb layers,

	Symmetry	Phonon frequency (meV)			α for TO			α for LO		
	Designation	Polarization	TO	LO	α_{Li}	α_{Nb}	α_{O}	α_{Li}	α_{Nb}	α_{O}
1	E_{2g}	x-y	9.4		0	0.38	0.12			
3	B_{2g}	z	18.5		0	0.39	0.11			
4	E_{2u}	x-y	28.8		0.50	0	0.01			
[1] 6	E_{1u}	x-y	29.9	33.5	0.48	0.03	0	0.46	0.04	0
[1] 8	A_{2u}	z	53.3	70.0	0.47	0.01	0.03	0.43	0.06	0.01
[2] 9	E_{2u}	x-y	58.8		0.01	0	0.49			
11	E_{1g}	x-y	59.4		0	0	0.50			
[1] 13	E_{1u}	x-y	64.4	71.6	0	0.12	0.38	0.02	0.10	0.38
15	B_{1u}	z	64.5		0.38	0	0.12			
[2] 16	E_{2g}	x-y	64.8		0	0.12	0.39			
[2] 18	A_{1g}	z	85.4		0	0	0.50			
[1] 19	A_{2u}	z	85.5	96.3	0.01	0.14	0.35	0.05	0.09	0.37
20	B_{1u}	z	89.5		0.13	0	0.38			
21	B_{2g}	z	94.8		0	0.11	0.39			

Table 6.2: Calculated zone-center phonon frequencies, with LO modes listed where they occur. See Appendix 6.7.1 for detailed descriptions of the atomic motions. All phonons with x-y polarization are doubly-degenerate, as required by the hexagonal symmetry. The last six columns show the calculated value of α_i, defined by equation 6.7 for both TO and LO modes.

decreasing the Nb-O distance.

Another point of interest we see in Figs. 6.6 and 6.7 is a significant change in how the valence band is situated in relation to the O $2p$ bands. Nb $4d$ states in the conduction band around the K point are significantly lowered in energy as the Nb-O distance is decreased so that the bandgap becomes indirect and much smaller. This change will have contributions from both a Madelung shift and from changes arising from the altered Nb-O interaction.

6.7 Zone Center Vibrational Modes

We have calculated the $3N - 3 = 21$ optical phonon eigenmodes with $\mathbf{q} = 0$. To our knowledge, experimental IR or Raman measurements have not been reported on $LiNbO_2$. However, we believe these results will be useful for comparison with electron-phonon calculations done on the de-lithiated Li_xNbO_2, which will be explored in future work. The frequencies are given in Table 6.2. Mode symmetries have been obtained with the use of

SMODES, part of the *Isotropy* package of Stokes and Boyer.[107] Masses of the ions used were 6.94 (Li), 92.91 (Nb), and 16.00 (O), all in amu. Also in Table 6.2 are given values of the isotope shift α, defined by

$$\alpha_i = -\frac{\partial \ln \omega}{\partial \ln M_i}, \tag{6.7}$$

where i runs over the different (types of) atoms in the crystal. The derivative was approximated with a centered difference, which, for a harmonic crystal with $\omega \propto M^{-1/2}$, introduces errors of order $(\frac{\delta M}{M})^2$. Using $\delta M = 1$ amu, this amounts to an error of about 2% for Li, and less for heavier elements. One would expect $\sum_i \alpha_i = \frac{1}{2}$ for a harmonic mode.

The dielectric tensor for a hexagonal system such as this will be diagonal with two distinct elements. For frequencies much higher than phonon frequencies but well below the gap, the static dielectric constants, calculated without ionic contributions, are found to be $\epsilon^x_\infty = 10.3$ and $\epsilon^z_\infty = 3.78$. One can then use the generalized Lyddane-Sachs-Teller relation, $\epsilon^\alpha_0 = \epsilon^\alpha_\infty \prod_m (\omega^\alpha_{\mathrm{LO},m}/\omega^\alpha_{\mathrm{TO},m})^2$ (where α runs over the cartesian directions, and the product is taken over all IR active modes with polarization in that direction) to include the ionic contribution for the low frequency dielectric constant. Doing so, we find for $LiNbO_2$ that $\epsilon^x_0 = 15.9$ and $\epsilon^z_0 = 8.27$. It is typical for LDA calculations to overestimate somewhat the dielectric constants, presumably due to the band gap being underestimated.

The eigenmodes fall into groups which are easily distinguishable by frequency. In the following discussion we include degeneracy in the numbering of modes. The first group, modes 1-3, are low frequency modes involving displacements of massive Nb-O layers against each other, with Li layers remaining fixed. The second group, modes 4-7, involve the lighter Li layers, and lie around 29 meV. The third group, modes 8-17 in the 53-65 meV range, involve motions where layers of atoms slide in the $x - y$ plane against adjacent layers of atoms, or groups of layers bounce against each other in the z direction. The last group of modes at 85-95 meV involves layers nearby each other bouncing against each other in

the z direction. A more detailed discussion of the individual modes is given in Appendix 6.7.1.

6.7.1 Phonon mode descriptions

Following is a descriptive list of the atomic motions for each mode given in table 6.2, grouped by their spectroscopic activity. Degeneracy is included in the numbering of modes.

Silent Modes

Modes 1-2: NbO_2 layers slide against each other in the x-y plane.

Mode 3: NbO_2 layers bounce against each other in the z direction.

Modes 4-5: LiO_2 layers slide against each other in the x-y direction. Li displacements are roughly an order of magnitude larger than O displacements, which results in the mass of the O atoms having very little effect on the frequency of this mode.

Modes 11-12: Adjacent O layers slide against each other, with Li and Nb layers remaining stationary.

Mode 15: LiO_2 layers bounce against each other in the z-direction. This is the one high frequency mode whose isotope shift α gets its major contribution from the Li atoms.

Mode 20: Out-of-phase Li layers beat against adjacent O layers in the z direction.

Mode 21: Out-of-phase Nb layers beat against adjacent O layers in the z direction.

IR Active Modes

Mode 6-7: In-phase Li layers sliding against NbO_2 layers. The main contribution to α comes from the light Li atoms, with the heavy NbO_2 layers making very little contribution. This mode is also IR active, with a small LO-TO splitting $\Delta\omega = \omega_{\mathrm{LO}} - \omega_{\mathrm{TO}} = 3.6$ meV.

Mode 8: The TO mode consists of Li layers bouncing against NbO_2 layers in the z direction, and can be thought of as the "z-polarized version" of modes 6 and 7. When the macroscopic electric field is included, the O displacements change sign and the mode becomes Li-O layers bouncing against Nb layers. $\Delta\omega = 16.7$ meV.

Modes 13-14: Li and Nb are in synchronized sliding against O layers. The metal layers are all in phase with each other, and out of phase with the O layers. This mode is IR active, with $\Delta\omega = 7.2$ meV.

Mode 19: The transverse mode consists of LiO_2 layers beating against Nb layers in the z-direction. The Li-O layers are all in phase. This mode is IR active, and once the macroscopic electric field is included, this mode can be characterized as having Nb layers bounce against adjacent O layers, where the Nb layers are out of phase. $\Delta\omega = 10.8$ meV.

Raman Active Modes

Modes 9-10: Out-of-phase Li layers slide in the x-y direction against adjacent O layers. The rest of the phonon modes from here on have the contribution to their isotope shift α dominated by O.

Modes 16-17: Out-of-phase Nb layers slide against adjacent O layers in the x-y plane.

Mode 18: The O layers beat against each other in the z-direction. This fully symmetricRaman active mode is of particular interest, as it corresponds to the variation of the internal structural parameter z. This mode has a significant impact on the electronic structure as discussed in previous sections, so we suspect that it may have particularly strong electron-phonon coupling in hole-doped Li_xNbO_2.

6.7.2 Clarifying Comments

The z-polarized A_{2u} IR active modes 8 and 19 have their eigenvectors affected by the inclusion of the macroscopic electric field. Without the electric field, the eigenmodes can be described as one where Nb layers bounce against Li-O units and one where Li layers bounce against Nb-O units. The application of the electric field causes these vectors to mix, and the descriptions change so that the latter one is replaced by a mode where Li and Nb bounce against O layers. The distinction between these two modes is the relative sign for Li and Nb displacements (negative for the former, positive for the latter.) It is not unusual to have modes mix to give different LO modes, as the non-analytic part of

	$LiNbO_2$			$NaCoO_2$		
	Li	Nb	O	Na	Co	O
Z^*_{xx}	1.10	2.26	-1.68	0.87	2.49	-1.68
Z^*_{zz}	1.69	1.31	-1.50	1.37	0.87	-1.12
Z^{Formal}	+1	+3	-2	+1	+3	-2

Table 6.3: Calculated Born effective charges for $LiNbO_2$, compared with those calculated for $NaCoO_2$ by Li, Yang, Hou and Zhu. [108] Note the disparity in the effective charges for the alkali metals and the transition metal in the z-direction. For O however, Z^* is not far from isotropic.

the dynamical matrix which incorporates the electric field can have eigenvectors differing from the analytic part of the dynamical matrix, resulting in a mixing of modes of the same symmetry. This is discussed in some detail by Gonze and Lee.[17] This complicates the association of LO modes with their corresponding TO mode, so we have chosen to pair the LO and TO modes such that $\omega_{\text{LO}} > \omega_{\text{TO}}$.

6.8 Effective charges

Born effective charge calculations have been carried out as described by Gonze and Lee.[17] The calculation was done using a planewave cutoff of 60 Ha and 200 **k**-points in the Brillouin zone to give effective charge tensors Z^* for each atom which are diagonal, and obey $Z^*_{xx} = Z^*_{yy}$, as required by symmetry for a hexagonal crystal. Results are given in Table 6.3 for the relaxed atomic structure. The effective charges of $NaCoO_2$ have been included in this table to illustrate the strong similarity between these two systems, which are similarly layered transition metal oxides but otherwise their electronic structures are quite different.

The effective charges of $LiNbO_2$ are rather different than those reported by Veiten and Ghosez[84] for $LiNbO_3$. There are structural and chemical differences responsible for this; the structure of $LiNbO_3$ has Nb coordinated in a distorted octahedral environment and thus has low symmetry. Perhaps more importantly, the formal charges of Nb are very different: Nb^{3+} in $LiNbO_2$, but Nb^{5+} in $LiNbO_3$, leaving the formal electronic configuration of Nb

in $LiNbO_3$ as d^0. The effective charges of such ions are known to sometimes be rather large, as is the case in $LiNbO_3$.

Z^*_{xx}(Li) is close to the formal charge of Li indicating ionic type response for in-plane motion. In fact, all ions have effective charge closer to the formal value for in-plane displacement than for $\hat{z}$ displacement. The charge tensor for Li shows similar anisotropy to that of Li in LiBC,[109] where it was inferred that Li is involved chemically in coupling between B-C layers. Similarly here, it can be expected that Li has chemical involvement in interlayer coupling between the electron rich Nb-O layers more so than Na does in Na_xCoO_2. This involvement is not strong enough to inhibit de-intercalation, however.

The smaller than formal charges for Nb indicates substantial covalent character to the bonding, which is especially strong in the $\hat{z}$ direction. This charge 'renormalization' may be related to the strong change in band structure due to change of the distance between the Nb and O layers, discussed in earlier sections.

6.9 Summary

In this work we have examined the electronic structure, the Wannier functions of the valence bands and their tight-binding parametrization, and several vibrational properties of the quasi-two-dimensional material $LiNbO_2$. These basic properties are important in providing the basis for understanding the behavior of the system when it is hole-doped by de-intercalation of Li.

Li_xNbO_2 seems to be a candidate for an insulator-to-superconductor transition, as it undergoes an insulator-to-metal transition and becomes superconducting, but doping studies are not systematic enough yet to shed light on this possibility. Phase space considerations in two-dimensional materials lead to superconductivity that is independent of doping level, at least when the Fermi level is not far from a band edge.[100] This property supports the possibility of an insulator-superconductor transition with doping, i.e. as soon as it becomes metallic it is superconducting.

The Wannier function, centered on and based on the occupied Nb d_{z^2} orbital, illustrates graphically not only how Nb bonds with neighboring O ions, but also that it couples with oxygens in adjoining layers. Inspection of the **k**-space wavefunction suggests there are direct Nb-Nb interactions within the d_{z^2} band as well as indirect coupling through O ions.

A tight-binding representation of the band, obtained by direct calculation (rather than fitting) using the Wannier function, reveals that several neighbors both in-plane and inter-plane are necessary to reproduce the dispersion. To model the interlayer interaction precisely requires four to five interlayer hopping parameters. For the experimental structure intralayer hopping is dominated by 2nd neighbor hopping, but the strength of both 1st and 3rd neighbor hopping is strongly modulated by varying the Nb-O distance. This electron-lattice coupling provides one possibility for the superconducting pairing mechanism in Li_xNbO_2.

Comparison with previous calculations of the band structure of $Li_{0.5}NbO_2$ suggests that the electronic structure of Li_xNbO_2 can be modeled in virtual crystal fashion, or perhaps even in rigid band fashion if that is convenient. The Nb d_{z^2} band is remarkably well isolated from neighboring bands by Madelung shifts and crystal field splitting. We suspect that the overriding importance of this system will result from its unique standing as a single band, triangular lattice system for which sophisticated studies on simple models may be directly comparable to experimental data.

6.10 Acknowledgments

The work described in this chapter was done in collaboration with W. E. Pickett. We have benefited from communication with K. E. Andersen and A. Simon. This work was supported by National Science Foundation Grant DMR-0421810.

Chapter 7

Gruneisen Parameters and Equation of State

The work in this chapter was done in collaboration with Phil Sterne from LLNL.

7.1 Introduction

Detailed information about the equation of state of materials is of considerable scientific and technological importance. New research facilities, such as the National Ignition Facility (NIF) at Lawrence Livermore National Labs (LLNL) have been recently developed which are capable of testing materials under extreme pressure and temperature conditions.

Many elements which are thought to be simple nearly free-electron-gas metals in ambient conditions have recently attracted a great deal of scientific interest due to reports unusual properties appearing under pressure. It was theoretically predicted that Li would be superconducting under pressure,[110] and later it was experimentally discovered to be superconducting up to 20 K around 48 GPa,[111] which at the time was the highest known superconducting transition for an element. This has recently been explained as BCS-type phonon mediated superconductivity with strong electron-phonon coupling.[112] Since then, Ca has been reported to be superconducting with $T_C = 25$ K[113, 114] under

pressure, which is currently the highest known T_C for an element. Metallic Y also shows a fairly high superconducting transition at 17K under pressure,[115] which has also been explained as strong electron-phonon coupling in a recent theoretical study.[116]

Aside from superconductivity, several other surprises have been discovered in the phase diagrams of elements under pressure. Above 32 GPa, Ca has been reported to exist in a simple cubic phase[117] which has been theoretically verified.[118] The existence of the simple cubic phase, especially under pressure, is quite surprising due to the low coordination and the tendency for group I and II metals to favor close-packed structures already at low pressures. The melting transition in the Na phase diagram has been seen to rise from 370K up to 1000K at ∼35 GPa and back down to 300K at 120 GPa.[119] Although it is not unusual to have a melt curve with a negative slope, the unusual characteristic seen in sodium is that the melting temperature drops 700K over three solid phases (bcc, fcc and $cI16$) of Na. The discovery of this transition has lead to considerable theoretical interest,[120, 121, 122, 123] particularly in the use of first principles molecular dynamics (FPMD) to model the melting.[120, 121, 122] In other group I metals (K and Cs), a bcc to fcc transition is observed, as well as decreases in the melting temperatures as solid-solid phase boundaries are approached, but these drops are relatively small, the largest being 100 K in fcc Cs.[124]

There are several elements which exhibit so-called correlated behavior. Lanthanides such as Ce, Pr and Gd have drawn considerable attention due to the presence of anomalous volume collapses when placed under pressure.[125] These materials require methods which can treat the f electrons on a more sophisticated footing than the local density approximation (LDA), such as Dynamical Mean Field Theory.[126, 127]

Considerable effort has been expended in attempting to map the phase diagram of carbon.[128, 129] Experimental measurements of the diamond melt curve are quite difficult, considering the very high temperatures required to melt diamond and that these types of experiments are usually done in a diamond anvil cell. The behavior of carbon under extreme pressures (which cannot be obtained via traditional laboratory methods) is of

considerable importance in geology and astrophysics. There are however significant impediments to this understanding; different theoretical models have difficulties agreeing with experiment or with other theoretical calculations on the diamond melt curve.[128, 129, 130]

Here we present a Density Functional Theory (DFT) study on three elemental systems, Al, Na and diamond-phase C. Our interest here is to demonstrate the suitability of this method for equation of state research, and to examine some simple rules for calculating melt curves from first-principles.

7.2 Theoretical Background

7.2.1 Grüneisen Parameter

The Helmholtz free energy F for a non-interacting phonon gas is given by

$$F(V,T) = \frac{1}{V_{BZ}} \sum_s \int_{\mathrm{BZ}} \left[\frac{\hbar\omega_{\mathbf{q},s}}{2} - kT \ln\left(1 - e^{-\beta\hbar\omega_{\mathbf{q},s}}\right) \right] d^3q, \tag{7.1}$$

where $\mathbf{q}$ is a vector within the first Brillouin zone, and s is a band index. We also define the dimensionless thermal Grüneisen parameter γ as

$$\gamma = \frac{V}{C_V} \left(\frac{\partial^2 F}{\partial T \partial V} \right) = \frac{\alpha V B}{C_V}, \tag{7.2}$$

where α is the coefficient of thermal expansion, B is the isothermal bulk modulus, V is the volume, and C_V is the heat capacity. It is straightforward that in the quasi-harmonic approximation, in which the phonon frequencies $\omega_{\mathbf{q},s}$ depend on volume and not temperature,

$$\gamma = \langle \gamma_{\mathbf{q},s} \rangle_{C_V} \tag{7.3}$$

where $\gamma_{\mathbf{q},s}$ is the mode Grüneisen parameter

$$\gamma_{\mathbf{q},s} = -\frac{\partial \ln \omega_{\mathbf{q},s}}{\partial \ln V}, \tag{7.4}$$

and the subscripted C_V indicates that the average over each mode is weighted by its contribution to the specific heat. In the quasi-harmonic approximation we have $\gamma_{\mathbf{q},s} = \gamma_{\mathbf{q},s}(V)$, while the averaging against specific heat gives γ its temperature dependence. At temperatures $T \gg \Theta_D$, all modes contribute equally to specific heat, so γ will be independent of temperature. For the systems studied here, this holds true even for $T < \Theta_D$, down to about $T \lesssim 100$K.

7.2.2 Melting Rules

The original theory of melting was proposed by Lindemann[131] where it was proposed that melting happens once the mean square deviation of atoms from their lattice positions reached some threshold value. Once the phonon frequencies $\omega_{\mathbf{q},s}$ and $\gamma(V)$ are known, one can calculate the melting temperature of the material using the Lindemann criteria [132],

$$\frac{d\ln T_m}{d\ln V} = -2\left[\gamma(V) - \frac{1}{3}\right]. \tag{7.5}$$

Integrating (7.5) and defining $\gamma = -\frac{d\ln\Theta_D}{d\ln V}$ (as is commonly done) gives

$$T_m = A\Theta_D^2 V^{2/3} \tag{7.6}$$

where A is an integration constant, which can be calculated in terms of physical constants and characteristics of the material under study,[132] however for this work we consider A to be a fitting parameter.

The author of Ref. [132] makes arguments based on the change in entropy that occurs during melting in order to effectively replace the characteristic temperature and volume in (7.6) to get

$$T_m = A\omega_0^2 V_{lm}^{2/3} \tag{7.7}$$

where the Debye temperature has been replaced by ω_0, the zero-th phonon moment, and the volume used is the volume of the liquid phase at melting. The phonon moments for

$n > -3$ are defined as follows,

$$\omega_n = \left[\frac{n+3}{3}\int_0^\infty \omega^n g(\omega)d\omega\right]^{1/n}, \qquad n \neq 0 \tag{7.8}$$

$$\omega_0 = \exp\left[\frac{1}{3} + \int_0^\infty \ln\omega \cdot g(\omega)d\omega\right]. \tag{7.9}$$

where $g(\omega)$ is the normalized phonon density of states. (A moment for $n = -3$ may also be defined, but that is not relevant for our purposes here.) The numerical factors are chosen for ease of comparison with a Debye model. For a normalized Debye density of states, ($g(\omega) = 3\omega^2/\omega_D^3$ for $\omega \leq \omega_D$, 0 otherwise) it is straightforward to show that all ω_n are equal to the Debye frequency. [132]

Certain phonon moments have specific physical interpretations, in particular the moment ω_{-2} scales the classical nuclear mean square displacement. [132] Considering the original spirit of the Lindemann criteria, that melting occurs when the mean square displacement of atoms reaches some threshold value, we suggest an alternate melting rule

$$T_m = A\omega_{-2}^2 V^{2/3}. \tag{7.10}$$

We investigate the quality of these melting rules in the next section. Since we do not have a good way to estimate V_{lm} from V, we simply use the volume of the solid at the melting temperature in (7.7) in the next section.

7.3 Method

All calculations were performed within Density Functional Theory (DFT) with a planewave basis, using the ABINIT code versions 4.4.4 and 4.6.5.[103] Pseudopotentials used were Troullier-Martins type [18], with three electrons for Al, one electron for Na and four electrons for C.

Phonon frequencies were calculated on a Monkhorst-Pack grid of **q**-points in the irre-

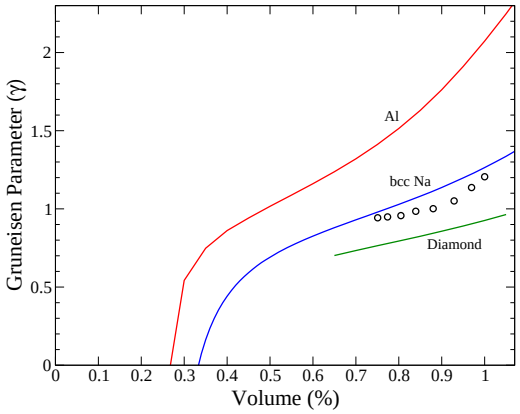

Figure 7.1: (Color online) Calculated Grüneisen parameter of the materials selected for this study.

ducible Brillouin zone. The **q** grid was unshifted so that Γ and zone boundary points were included. This is the most convenient approach to calculate dynamical matrices and to insure the acoustic sum rule is obeyed. Inclusion of Γ point phonons presents problems in calculating the numerical derivatives in (7.4), so the phonon frequencies were interpolated onto a shifted grid which does not include Γ for calculations of $\gamma(V)$.

For Al, the number of **k**-points used was increased as the volume was decreased, in order to maintain a high resolution of the Fermi surface. This same approach was attempted with Na, but we found it produced noticeable 'kinks' in the results around the volume where the number of **k**-points was changed.

7.4 Materials

We chose three elemental materials to test the theoretical methods presented in the previous sections. The first of these systems was Al, which was chosen because it is well known that Al is a rather free-electron like metal and treated well within present formulations of DFT. The Al pseudopotential used is a norm-conserving Troullier-Martins type [18], with three (3) valence electrons.

Sodium was chosen as the second system because the recent discovery of its unusual

melt curve [119] provides an opportunity to test the various melting rules from section 7.2.2 against each other on a system which is known to have a negative melt slope for an appreciable pressure range.

The diamond phase of carbon was chosen as the third system to study because it is an elemental system for which there are relatively few phase boundaries, as well as it is distinct from Na and Al in that it is an insulator, and there are two atoms per unit cell so optical modes must be considered. The melting transition of diamond is also of considerable interest in astrophysical research in understanding diamond-methane transitions which may occur in the core of gas giants. Calculations for diamond were not carried out below 60% of the equilibrium volume, as this has already reached a pressure of 1000 GPa.

We have calculated the volume dependent Grüneisen parameter for these three elemental systems over a large range of pressures from first principles. Shown in Fig. 7.1 is a plot of the Grüneisen parameter for Na, Al, and the diamond phase of C. The tendency for γ to go negative at large compressions ($V \lesssim 35\%$) is due to lattice instabilities from phonon modes going to zero frequency. In the DFT calculations, these instabilities eventually cause the phonon frequencies to become imaginary, so near these instabilities it becomes difficult to use finite differences to calculate the derivatives of $\omega_{\mathbf{q}}$ to evaluate (7.4).

7.4.1 Aluminum

Shown in Fig. 7.3a are plots of the phonon moments ω_n as defined by (7.8) for Al. For a given volume, ω_n for $n > -2$ is rather independent of n, indicating Al is very Debye-like even up to high pressure. The 'flatness' of these curves indicate that melt rules based on ω_{-2} and ω_0 will not give significantly differing results. Thus, in Fig. 7.2 we only show the melt curve generated from the Debye temperature. The agreement with experimental data points[133] as well with other theoretical calculations based on a more sophisticated approach involving calculation of anharmonic contributions and the free energy of the liquid phase[134] is quite good.

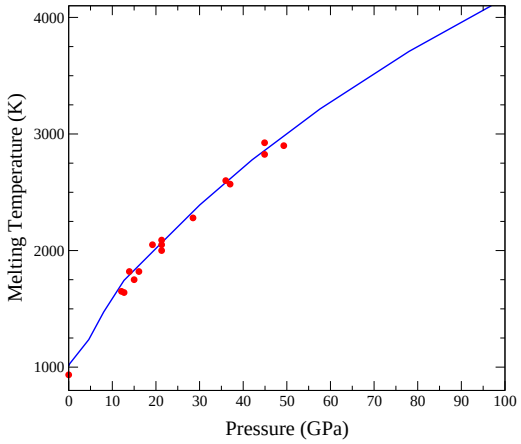

Figure 7.2: (Color online) Plot of melt curve of aluminum as calculated from (7.6), compared with experimental points, from ref. [133]. The agreement is very good.

7.4.2 Sodium

Calculations for Na were done both in the bcc and fcc phases. To test whether the pressures calculated using the pseudopotential method would be accurate due to the loss of interaction between the 2p semi-core states, total energies were calculated using the full-potential local orbital (FPLO) code. The total energy curves generated by ABINIT and FPLO were very similar, even at high pressures.

Sodium-BCC phase

Shown in Fig. 7.4 are the melt curves as calculated by (7.6), (7.7) and (7.10), compared to experiment[119] and first principles molecular dynamics (FPMD).[121] The Lindemann rule based on ω_{-2} gives significantly better agreement with experiment than the rules based off ω_0 or θ_D in the region where the melt curve has a negative slope ($P \gtrsim 20$ GPa), as well as the pressure at which the maximum occurs. The agreement with experiment in this phase is at least as good as the agreement between the FPMD calculation and experiment.

The source of the improvement upon using ω_{-2} is clear. Under high compression, the bcc to fcc lattice instability plays a role in softening phonons, to which ω_{-2} is much more

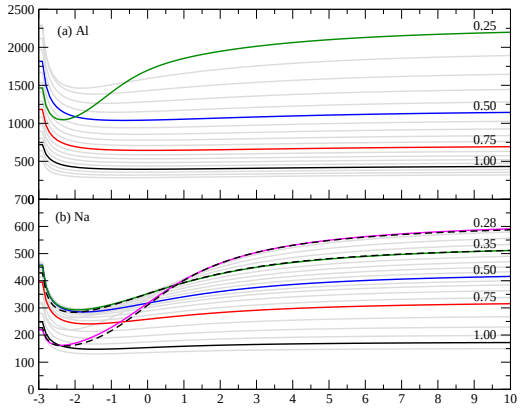

Figure 7.3: (Color online) Shown here are the phonon moments ω_n plotted vs. n (see eqn. 7.8) for (a) Al and (b) Na at selected volume percentages. A flat line indicates the frequency distribution is very Debye-like. Al phonons are very Debye-like, even at high compressions, but Na phonons become less Debye-like under pressure.

sensitive to than ω_0. In Fig. 7.3 we see this causes ω_{-2} to drop much more than ω_0 at high compressions. At lower pressures, the ω_n vs. n curve is rather flat, so the two moments of interest here have very similar values. This gives us a very simple physical picture of why there is a maximum in the melt curve and a drop in the melting temperature as pressure is increased – the bcc lattice is being driven to instability where the fcc lattice will become the stable phase. Intuitively speaking, as the bcc lattice becomes more unstable, atoms are 'less bound' to their crystallographic positions so less thermal energy is required for melting to occur. The lowest frequency modes dominate this displacement, because they are easiest to occupy. To first order in ω/T, the occupation of a mode with frequency ω is T/ω, so the root mean square displacement is roughly proportional to $\sqrt{T}/\omega$. As a mode softens under increasing pressure, its displacements get larger at constant temperature allowing melting to occur at a lower temperature. This effect is captured rather well here by the melting rule based on ω_{-2}.

Sodium-FCC phase

For the fcc phase of Na, there are only three experimental points from ref. [119], and the DFT-GGA calculations are not harmonically stable near 100 GPa, so we are unable

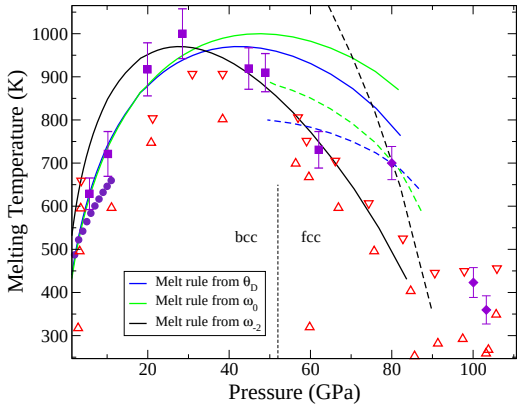

Figure 7.4: (Color online) Plot of the phase diagram sodium, as calculated from (7.6), (7.7) and (7.10), compared with experiment and *ab initio* molecular dynamics. Solid lines indicate melt curves calculated for bcc Na, and dashed lines indicate calculations performed for fcc Na. Solid symbols indicate experimental data, open symbols indicate molecular dynamics data. Solid squares are bcc phase melting temperatures, solid diamonds are fcc phase melting temperatures.[119] Solid circles are bcc melting temperatures from ref. [124]. Up triangles indicate simultations of solid phase, and down triangles indicate simulations of liquid phase.[121] The vertical dashed line indicates the bcc-fcc transition given by our calculation.

to draw very useful conclusions about the agreement of theory with experiment in this region. The fcc melting curves in Fig. 7.4 are stopped below 100 GPa due to these instabilities. There is a systemic underestimation of the stability of a phase with respect to pressure. Experimentally the bcc $\rightarrow$ fcc transition pressure should be 65-70 GPa, but our calculations predict this transition to occur at 52 GPa. We did not investigate the fcc-$cI16$ transition.

In the FPMD calculations it was found that there is a transition in the liquid above about 65 GPa where a pseudogap forms in the density of states for the liquid phase that does not appear in the fcc phase, and the coordination of atoms in the liquid becomes much more like that of the high pressure $cI16$ phase. It is most likely that the failure of the Lindemann melt rules in the fcc phase is related to the fact that this sort of structure in the liquid phase is ignored. Interestingly, the melt curve from (7.10) tracks the melting temperature of the FPMD calculations well into the fcc region.

If we compare the three curves from the melt rules, we see that the curves from ω_0

and θ_D look very similar; there is little to be concluded from comparing these two curves. The curve from ω_{-2} is quite unrealistic. It is somewhat surprising the the ω_{-2} curve performs unrealistically when it gives very good agreement with the bcc phase. It is a clear consequence of the results presented in Fig. 7.3 where we see that ω_n is rather insensitive to the phase transition from bcc to fcc, but the experimental melt curve shows a change in slope at the phase transition. In fact, the integration constant in any of the calculated fcc melt curves can be adjusted so that they lie on top of the calculated bcc melt curves. This actually would agree quite well with the FPMD calculations up to about 90 GPa. Above this, anharmonic effects may play a significant role in stabilizing the system, and if so, then this would have an impact on the melt curve and certainly cause the Lindemann criteria to be inadequate in this region.

7.4.3 Diamond

Shown in Fig. 7.5 is the melting curve for diamond calculated from (7.7) and (7.10) compared to results from a variety of other theoretical methods.[129, 130, 128] For each (7.7) and (7.10), two different values of the arbitrary constant are chosen to show agreement with calculations from ref. [130] (lower curves) and ref. [129] (upper curves). The agreement of the upper ω_{-2} melt curve with results from the *ab initio* molecular dynamics calculations[129] is rather good, although our melt curve does not show a maximum in this pressure range. The melt curve from ω_0 does not agree quite so well. Both the lower curves' agreement with calculations based on Brenner's bond order potential[130], is quite good up to 100 GPa, and the ω_{-2} melt curve performs slightly better in the 100-200 GPa range.

The agreement of our calculations of the Lindemann model with the other theoretical methods presented here is not significantly worse than the agreement between those other theoretical models. Discrepancies in the diamond melting curve are likely caused by several factors. A significant source of error is likely the anharmonicity from phonon-phonon interactions which becomes stronger at higher temperatures, which is the break

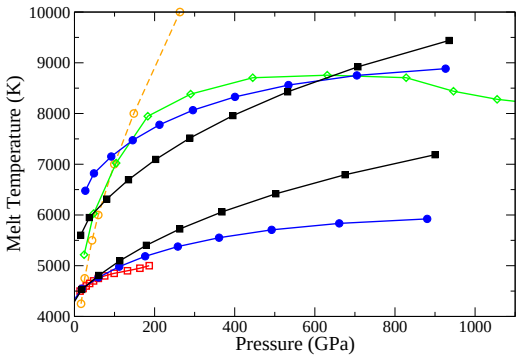

Figure 7.5: (Color online) Shown here is the melt curve calculated from ω_0 (black, solid squares) and ω_{-2} (blue, solid circles) compared with results from theoretical calculations in refs. [129] (green, open diamonds), [128] (orange, open circles) and [130] (red, open squares). Melt curves calculated in this study are shown for two different values of the integration constant for comparison with values from refs. [129] and [130].

down of the quasi-harmonic assumption. Also diamond likely undergoes an insulator to metal transition as it melts, further complicating things. Additionally, the liquid phase of diamond is unusually complex, with some groups speculating about the possible existance of a liquid-liquid phase change.[130]

7.5 Conclusion

We have seen here that DFT can provide an accurate equation of state for materials under a large range of pressures and temperatures. We have presented a method based on the Lindemann criteria for calculating the melting curve for simple elemental materials with only a single adjustable parameter, and we have seen here that this method can provide a reasonably accurate model for melting over a range of pressures. Unlike other approaches for calculating the melt curve, all calculations are based on $T = 0$ properties of the crystalline solids; no calculation of the thermodynamic properties of the liquid phase is necessary. For fcc-Al and bcc-Na, the Lindemann model provides excellent agreement with experimental melt curves, so we conclude that for these materials, the melting temperature's pressure dependence is mostly based on characteristics of the solid phase of the material.

In bcc-Na, we find that the accuracy of the Lindemann model can be improved by choosing a characteristic temperature which is directly related to the mean square atomic displacements. It is seen that the overturn in the melt curve is driven by phonons which are soft at high pressures, so they have high populations at melting temperatures and thus large atomic displacements, causing the melt curve to drop as these phonon frequencies soften. For fcc-Na the melt curve cannot be adequately modeled with the Lindemann model using the same characteristic temperature as is used for bcc-Na. It is likely that anharmonic effects play a significant role in this region which are not considered in this method.

For diamond, the melt curve gives some results which compare reasonably well with other theoretical calculations. Molecular dynamics calculations on carbon indicate that the liquid has unusual properties; atomic coordinations ranging from 2-fold to 5-fold are reported[130, 135] and a variety of bonds (sp and sp^3) are present.[135] These unusual characteristics of the liquid phase probably have an impact on the melting behavior which is not captured in this model. It is worth noting that there is significant disagreement between various theoretical methods on the melting curve of diamond; the approach presented here does little to help distinguish the previous calculations.

Chapter 8

DMFT applied to Yb Valence Transition

The work described in this chapter was done in collaboration with Andy K. McMahan from LLNL and Warren E. Pickett.

8.1 Introduction

It is well known that the lanthanides Yb and Eu behave rather differently from the other lanthanides in their elemental states, due to their unusual valence states. The majority of the lanthanide series is trivalent, however for Yb and Eu the 3+ valence state has a single hole in the f-subshell, and it can be favorable to fill this hole with a valence electron. This results in a number of anomalous properties, such as a larger molar volume (as compared to the trend the rest of the lanthanide series follows), and a lower bulk modulous.[136] They also exhibit anomalous behaviors in pressure or temperature dependent properties; for example Yb has a thermal expansion coefficient that is three times larger than most other lanthanides. [137] Yb exhibits a well known valence transition under pressure, where an f electron is gradually promoted to the valence band from 0-34 GPa. Equation of state fits based on a divalent and trivalent Yb ion do well at low and high pressures, respectively,

however the mixed-valent region between these pressures is difficult to fit well.[136]

There are a variety of *ab initio* methods developed to model the correlated behavior of electrons in systems involving ions such as Yb. The most commonly used method, LDA+U has had a great deal of success dealing with transition metals systems. It is somewhat less well suited to to the lanthanides, particularly Yb, as Yb's f-shell is nearly fully filled in LDA. In this paper, we examine the pressure and temperature dependence of the Yb valence transition using the LDA+DMFT method, which introduces an orbital dependent potential (similarly to LDA+U) but allows for that potential to be frequency dependent, in contrast to LDA+U. DMFT requires the choice of a impurity solver; here we compare and contrast the results from two impurity solvers, the computationally efficient Hubbard-I (HI) solver, and the highly accurate Quantum Monte Carlo (QMC) solver.

8.2 Calculations

Yb goes through several phase transitions under pressure, including a re-entrant fcc phase. Experimental evidence suggests that the valence transition in Yb is relatively insensitive to the phase, so all calculations performed in this work are done in the fcc phase. This is not unreasonable, since we believe the important physics is occuring in the highly localized f-orbitals, which play very little role in bonding, and the phases at both low and high pressure have high coordination numbers.

8.2.1 DFT-LDA calculations

The LDA/GGA equation of state calculations were done in the full potential LAPW scheme using the publicly available EXCITING code. [138] LDA calculations used as the starting point of LDA+DMFT calculations were done using the LMTO-ASA approximation and FPLO. [22]

8.2.2 All electron LDA+DMFT

In many DMFT calculations, the Hilbert space is downfolded to only the correlated bands in order to reduce the computation time required for expensive impurity solvers. We do not take this approach here; indeed since the valence transition of Yb is of principal interest here, it would be inappropriate to downfold the valence orbitals out of the basis. Thus, the LDA+DMFT calculations presented here retain the $6s$, $6p$, and $5d$ valence orbitals in the crystal, bath, and impurity Green's functions. We term this method "all-Electron LDA+DMFT" since no downfolding has been done. The self-energy is taken only to be non-zero on the f-orbitals, and it is composed of only two distinct (frequency-dependent) values, corresponding to the two relativistic $j = 5/2$ and $j = 7/2$ states.

The LDA calculation is done with an LMTO basis in an atomic sphere approximation. Because of the close-packed nature in the fcc phase this should be an adequate calculation. Two different impurity solvers are used in DMFT, the Hubbard I (HI) atomic solver and the Hirsch-Fye Quantum Monte Carlo (QMC) solver [74]. The QMC solver is highly accurate, but very computationally expensive. CPU time for QMC goes as $O(\beta^3)$ where $\beta = T^{-1}$ is the inverse temperature, giving a practical lower limit on temperature of about 630K in our calculations. The only systematic source of error in the QMC algorithm is the result of the discretization of imaginary time into L 'time slices.' We will examine the results for various values of L to get an idea of the magnitude of this error. Hubbard I treats the impurity as an isolated atom, neglecting the DMFT bath function, so all physics related to the Kondo effect are lost in this approximation.

The LDA+DMFT calculations presented here are not done with charge self-consistency. Performing a charge self-consistent calculation is a significant challenge for DMFT, particularly if the Hilbert space is downfolded, or computationally expensive impurity solvers are used. For Yb, charge self-consistency is likely to be important, because DMFT can significantly modify the orbital occupations. Charge self-consistent results are currently being explored and will be presented in a future publication.

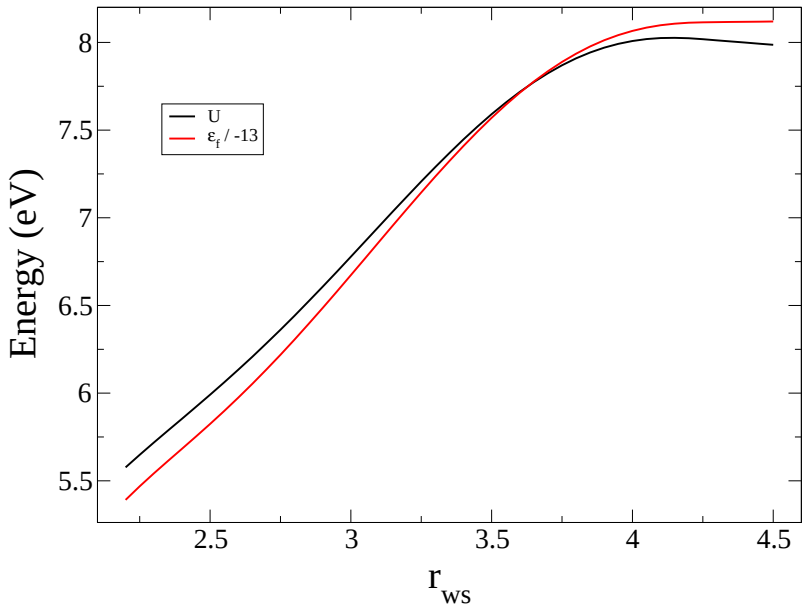

Figure 8.1: Plot of LDA+DMFT parameters U and ε_f used. $-\varepsilon_f/n_0$ (see text) is plotted for comparison with U.

8.2.3 Hubbard Parameters

In doing an all-electron LDA+DMFT calculation, since the interaction is applied only to the interacting states a double-counting energy must be subtracted because the LDA Hamiltonians already contain a mean-field description of the interaction. The approach used here is to simply modify the Hamiltonian used in the DMFT: $H_{\mathbf{k}} \rightarrow H_{\mathbf{k}} + \Sigma(\omega) - \varepsilon_f$, where the self-energy $\Sigma(\omega)$ and the double counting ε_f are applied along the diagonal of the f-orbital block. The double counting parameter for each volume is calculated from

$$\varepsilon_f = -\frac{W}{14}(7 - n_0) + U\left(n_0 - \tfrac{1}{2}\right) + \varepsilon_f^{\mathrm{LDA}} \tag{8.1}$$

where W is the f-state bandwidth and n_0 is the nominal f-electron count, 13 in the case of Yb and $\varepsilon_f^{\mathrm{LDA}}$ is the center of the f bands in LDA. This approach has been used previously by McMahan *et al.* [139]. The value of U is computed via constrained LDA calculations [140]. The values of U and ε_f are shown in Fig. 8.1.

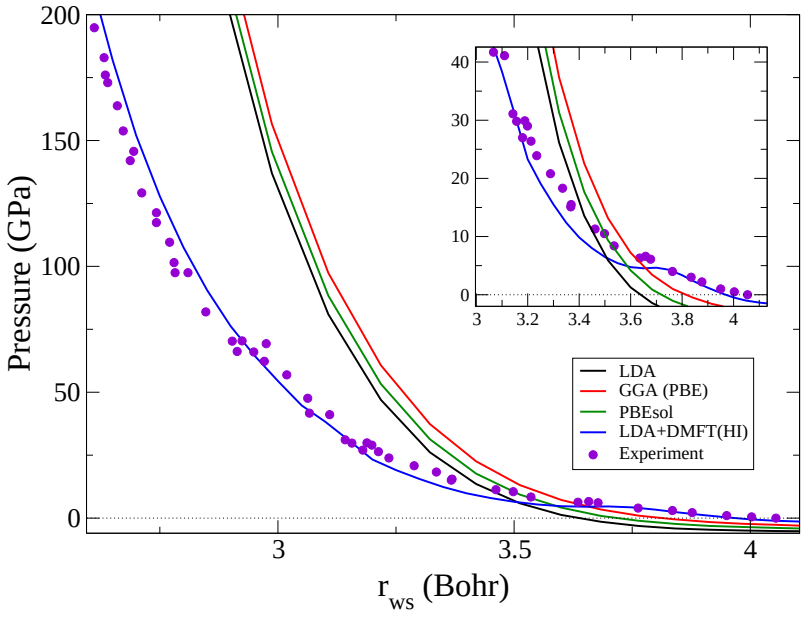

Figure 8.2: Plot of equation of state for Yb from experiment [141], various DFT functionals, and DMFT(HI). The inset shows a blow-up of the pressure region where the valence transition occurs. Even though LDA+DMFT(HI) shows a spurious volume collapse transition at 5 GPa, its predicted equation of state is much improved over LDA or GGA.

8.3 Equation of State

Results presented from here will generally be in terms of r_{ws}, related to the volume and lattice constant by $V = \frac{4}{3}\pi r_{\mathrm{ws}}^3 = \frac{1}{4}a^3$. Shown in Fig. 8.2 is the calculated pressure-volume curve LDA, GGA and LDA+DMFT(HI) compared to experimental values [141]. LDA+U results are not shown as they do not have a significant impact. This is largely due to the fact that the f orbitals are nearly fully filled, so LDA+U does not have a significant impact. LDA produces the worst equation of state (EOS), with $V_{\mathrm{LDA}}(P = 0) = 0.75V_0$, where V_0 is the experimental equilibrium volume. The two GGA functionals used provide some improvement of the $V(P = 0)$ prediction, but the overall shape of the P-V curve is unchanged and still unsatisfactory. The LDA equilibrium volume might be improved if the f electrons are frozen into the core and a divalent ion is forced in the calculation. Even if this approach provided reasonable accuracy for the LDA V_0 predcition, it would be unsatisfactory for calculating the equation of state over even a small pressure range

and would likely require adjustments based on empirical information about the valence transition.

LDA+DMFT(HI) shows a much improved equation of state. Equilibrium volume is roughly at $r_{\rm ws} = 3.97$, which is a slight over-binding of the unit cell from experiment, where the equilibrium volume is at $r_{\rm ws} = 4.05$. This is about a 6% smaller volume than experiment. Seen from the inset of Fig. 8.2, the error in the region near $V = V_0$ is relatively small, but since divalent Yb is fairly soft, P-V curve in the divalent region is not terribly steep, so this results in a seemingly large error in equilibrium volume. The major discrepancy in the LDA+DMFT(HI) equation of state is that it predicts a spurious volume collapse at around 5 GPa. This is most likely caused by DMFT(HI) producing the valence transition much faster than seen in experiment, discussed further in the next section. This spurious volume collapse could also be related to structural phase transitions to bcc and hcp that occur above 4 GPa, along with the fact that the fcc phase is re-entrant, but we believe this is unlikely since the intermediate phases still have a high coordination number. At $r_{\rm ws} < 3.75$, the DMFT(HI) EOS predicts lower pressures than experiment, down to approximately $r_{\rm ws} = 3.2$, where the valence transition is nearly complete. Below that volume the theoretical and experimental P-V curves agree quite well.

8.4 Orbital occupation

Shown in Fig. 8.3 is the f-orbital occupation n_f vs. r_{ws} at $T = 630$ K for both impurity solvers. DMFT(QMC) at $L = 80$ provides excellent agreement with experiment. There may be significant error from the imaginary time discretization, as seen by the differences in $L = 80$ and $L = 160$. In fact, the presence of this error may make the agreement with experiment *better* at $L = 80$ than at higher L. This is most likely due to the lack of charge self-consistency in the LDA+DMFT method. The removal of electrons by DMFT should lower the $4f$ potential in LDA, which will attact electrons back into the $4f$ orbitals in a charge self-consistent cycle, thus we should expect that an accurate LDA+DMFT(QMC)

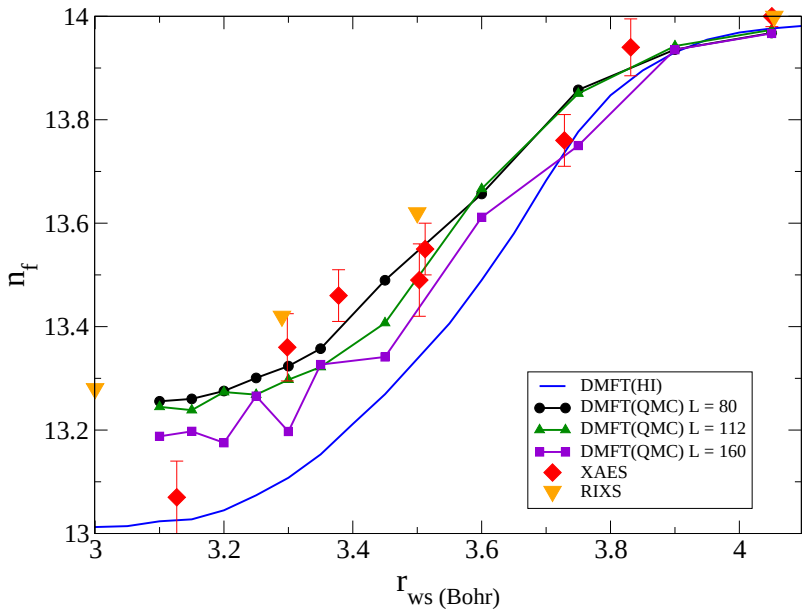

Figure 8.3: Plot of Yb f occupation vs. r_{ws} as calculated by LDA+DMFT with HI and QMC impurity solvers, compared to experimental data. X-ray absorption edge spectroscopy (XAES) data was taken from Ref. [142], and resonant inelastic x-ray scattering (RIXS) data taken from Ref. [143]. The DMFT calculations are performed at $T = 630$ K, and QMC calculations were done with three different imaginary time discretizations. The $L = 112$ and $L = 160$ QMC calculations are much more difficult to converge than at $L = 80$.

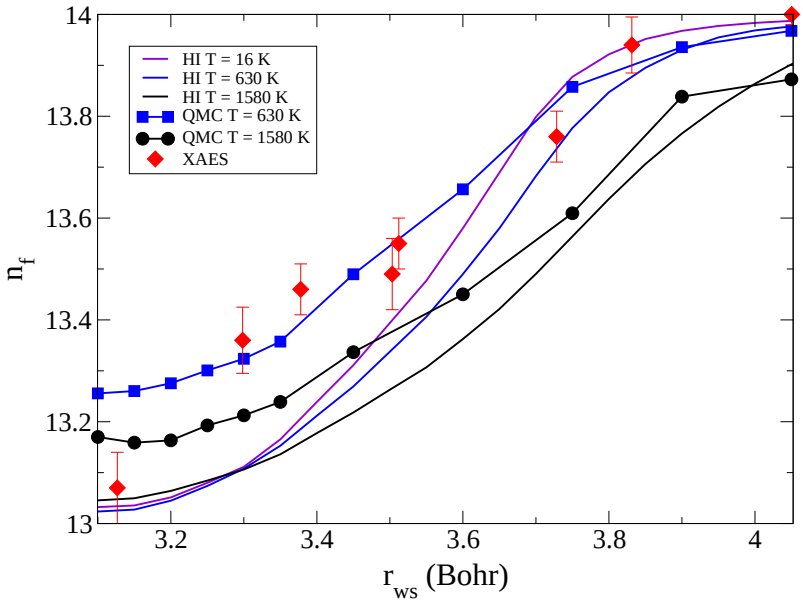

Figure 8.4: Plot of Yb f occupation vs. r_{ws} at temperatures 16 K, 630 K, and 1580 K. Room temperature experimental data is shown for comparison.

procedure without charge self-consistency would underestimate n_f. The calculations at larger L values have proved difficult to converge, for reasons discussed in Sec. 8.4.1.

DMFT(HI) provides the valence transition as expected, however there is a slight overestimation of the tendency for the hole to appear in the f states, as compared to experiment and DMFT(QMC). This is not too surprising, as under pressure one would expect a hole in the f states to be only partially localized, but DMFT(HI) does not allow any delocalization of the hole to occur. The DMFT(QMC) results closely match experiment over the entire pressure range of interest, except for the single point at $r_{\rm ws} = 3.13$. There is considerable noise in the experimental data taken at this pressure (34 GPa) in Ref. [142], and it doesn't agree well with the trend in the RIXS data, so we conclude that this disagreement is not significant.

Orbital occupation temperature dependence

The calculated n_f values show a significant temperature dependence in both DMFT(HI) and DMFT(QMC). The temperature dependent n_f values are shown in Fig. 8.4. The

lowest temperature accessible in DMFT(QMC) is 630K, and its agreement with room temperature data very satisfactory, although it is showing that the transition is not fully completed at 630 K. At 1580K the calculated n_f is lower at all volumes in than at 630 K, suggesting that the f^{13} state is favored at high temperature. Both QMC and HI agree on this trend. Also consistent with this trend, and shown in Fig. 8.4 is the n_f from DMFT(HI) at $T = 16$ K. This temperature is inaccessible in the QMC Hirsch-Fye algorithm, but we expect at least the qualitative trend to be the same in QMC and HI. At $T = 16$ K, the f^{13} state is less favored relative to the f^{14} state.

In DMFT(HI) the transition to the f^{13} state is never fully realized at very low temperature, although it is close, coming to a minimum value of 13.1 at around 40 GPa. As with the $T = 630$ K HI data, this is likely an underestimation of the true f occupation at low temperature, because the DMFT(HI) method overestimates the tendency for a hole to localize in the f-orbitals. Nevertheless, these results are at least qualitatively consistent with experimental temperature results. The strong temperature dependence of n_f in both DMFT(QMC) and DMFT(HI) is consistent with measurements of Yb valence done in Yb compounds, such as $YbAgCu_4$ [144], $YbInCu_4$ [145, 146]. Remarkably, in YbGaGe [147], and $YbAl_3$ [148], the measured valence of Yb is temperature independent. The characteristics in the electronic structure of those materials that causes the Yb valence to be temperature independent are not understood.

8.4.1 QMC Ergodicity

In the DMFT(QMC) calculations, we encountered significant difficulties with ergodic behavior in the Hubbard-Stratonovich field configurations. Such behavior has been seen in the past by Scalettar, Noak and Singh [149] in the Hubbard model with $U >> W$ where the Monte Carlo sampling became 'stuck' around configurations where there was a net spin moment, when in fact the average spin moment should be zero. This was solved by introducing global moves which flip all the Hubbard-Stratonovich fields at once.

Shown in Fig. 8.5 are the normalized sampling distributions of configurations as a

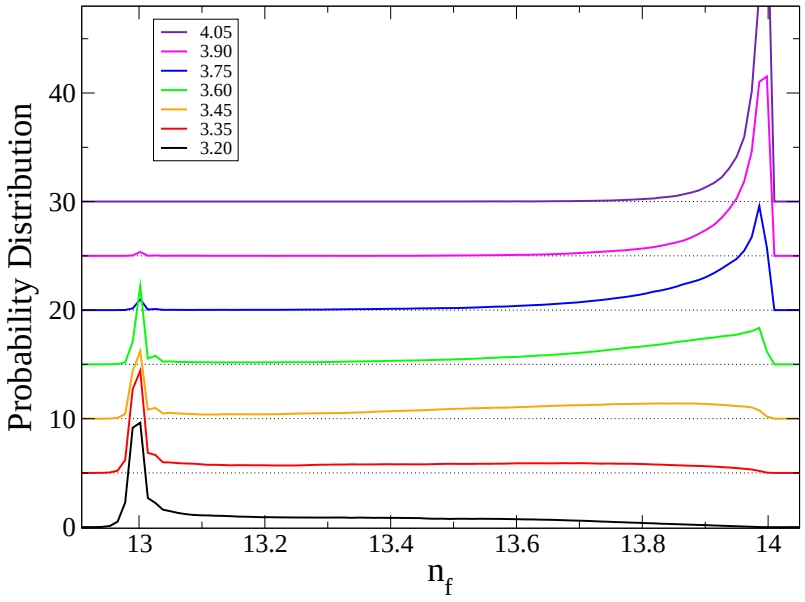

Figure 8.5: Plot of probability distribution of sampling Hubbard-Stratonovich field configurations in DMFT(QMC) of a given f-electron count n_f. Different curves correspond to different volumes, from $r_{ws} = 3.10$ at the bottom up to $r_{ws} = 4.05$ at the top.

function of n_f. Generally speaking, there are peaks near $n_f = 14$ and $n_f = 13$, and the relative ratios of their heights changes as a function of volume. The volumes which are most difficult to converge are $r_{ws} = 3.45$ and $r_{ws} = 3.60$, where there is significant weight in both the peaks around n_f equal to 13 and 14. At $r_{ws} \leq 3.35$, convergence is still difficult because the distributions still maintain a broad feature that extends almost up to $n_f = 14$. At $r_{ws} \geq 3.90$, convergence of the calculation is no problem as the distributions in this region are almost entirely centered around the $n_f = 14$ area with very little weight near $n_f = 13$.

The ergodicity problem here can't be easily solved by global moves, as it is nontrivial to derive a move for the Hubbard-Stratonovich fields which changes the occupation of a single orbital from 0 to 1, or vice-versa. Previous applications of global moves have been restricted to swapping the occupations of two orbitals, and the perscription for changing the Hubbard-Stratonovich fields is straightforward in that case. These results show another clear difference from ergodicity issues observed by other groups. In particular, at the

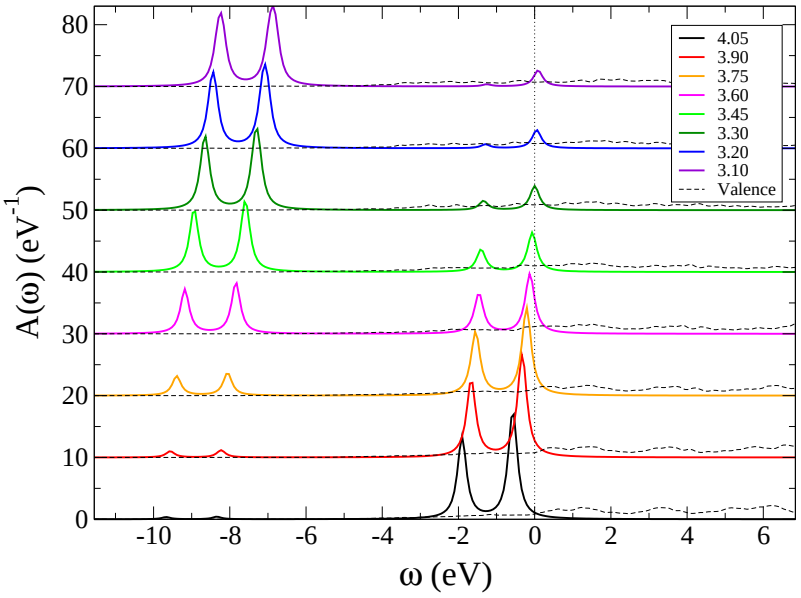

Figure 8.6: Plot of Yb spectral function $A(\omega)$ at $T = 630$ K calculated in LDA+DMFT(HI) for selected $r_{\rm ws}$ values, relative to the chemical potential. Spin-orbit split peaks corresponding to the $f^{14}spd^2$ state are near the chemical potential, while peaks corresponding to the $f^{13}spd^3$ state are around $-U(r_{\rm ws})$.

volumes where the ergodicity is most apparent, there is a non-vanishing sampling of states between the peaks at $n_f = 13$ and $n_f = 14$. This is an indication that the barrier to transitioning between integer occupations is not large, and perhaps a brute-force approach might be most applicable. This property is likely a consequence of Yb being a metal at all volumes, due to weak hybridization of the overlapping metallic *spd* orbitals with the *f* orbitals.

8.4.2 Spectral Function

Calculations of the spectral function $A(\omega)$ are presented in Fig. 8.6 for DMFT(HI). At low pressure, there is a clear two peak structure near the Fermi energy which is attributed to spin-orbit splitting of the *f*-states so that there is one each of $j = 5/2$ and $j = 7/2$ peaks. As the pressure is increased, the spectral weight of these f^{14} peaks decreases, and the f^{13} peaks appear below at about $-.6$Ry $\approx U$. Also, the upper peak ($j = 7/2$) becomes pinned to the Fermi energy. When the valence transition is fairly complete, the

$j = 7/2$ peak above the Fermi energy can be interpreted as the upper Hubbard band for the $4f$ states. From this we see how the Hubbard bands evolve with pressure; they don't gradually split (as with increasing U) but the lower Hubbard bands (f^{13}) gradually appear and the upper Hubbard bands gradually disappear and simultaneously move across the Fermi energy until there is only a single $j = 7/2$ state left above ε_F. This effect is clearly something that cannot be captured by a single-particle band theory such as LDA or LDA+U, because they can only produce bands which have integral weight. It is not impossible to get an f^{13} state in LDA+U; it can be done in certain chemical environments [61], but it is rather difficult to achieve for elemental Yb. The mixed valent state is also rather inaccessible for LDA+U, because LDA+U cannot create a Hubbard band for the f-states which has fractional occupation (which would be required to capture the gradual nature of this transition) without strong hybridization, which would not be reasonable for narrow band f states.

8.5 Conclusion

We have examined the valence transition and equation of state of elemental fcc Yb using LDA, GGA, LDA+U, and all-electron LDA+DMFT with impurity solvers that are either highly accurate or very computationally efficient. We have shown how and why LDA+U results can be suspect for a system containing Yb, particularly if Yb may be in a mixed valent state, and that LDA+DMFT corrects these deficiencies. LDA+DMFT(HI) provides good qualitative agreement with experiment, showing a full valence transiton to f^{13} over 35 GPa and the transition is gradual as seen in experiment. LDA+DMFT(QMC) improves on this by providing excellent quantitative agreement with experiment. We examined the temperature dependence of this valence transition, finding that both DMFT(HI) and DMFT(QMC) are consistent with experimental results for several Yb compounds over all temperature ranges studied.

8.6 Acknowledgements

I would like to thank Simone Chiesa, Jan Kunes, and Richard T. Scalletar for stimulating duscussions on DMFT, QMC and Yb.

Chapter 9

Orbital Ordering in RbO_2

9.1 Introduction

Correlated materials have generated a lot of interest recently in the literature. Typically these materials contained localized d or f electrons which are not accurately treated in density functional theory by the L(S)DA or GGA exchange-correlation approximations, although there are cases where p orbitals behave in correlated manners, and can show magnetic effects. SrN was recently predicted to show magnetism in N_2 dimers [150], and antiferromagnetism in RbO_2 has been known for at least 30 years [151].

Proper treatment of these materials requires methods which go beyond local approximations. Two commonly used methods are LDA+U and LDA+DMFT, which combine LDA's accurate treatment of the valence electrons, with a many-body orbital dependent treatment of the correlated subset of orbitals.

Since the identification of electrons in a solid as belonging to a particular atom or its s, p, d, etc. states is somewhat ambiguous, any treatment of correlations is going to somewhat depend on how these states are projected out of the Bloch states. This is typically not problematic, and most applications of both LDA+U and LDA+DMFT work quite well with an atomic orbital projection which may be different in different codes. At least, these methods don't typically fail to adequately describe a system of interest because of how the

projections are done. There are exceptions however. Generally, one should project states onto Wannier functions and use these as the orthonormal basis for a correlated method, and there are cases where the Wannier functions that need to be used are significantly different from atomic orbitals. RbO_2 is an interesting example because its valence bands are composed of O p states, and the O atoms are paired up in molecular units, so it is more sensible to think of this crystal as being a distorted rock salt structure with Rb^+ as the cation, and the hyperoxide ion O_2^- as the anion. An application of a LDA+U or LDA+DMFT to this material must use projections on O_2 *molecular* orbitals, rather than atomic orbitals which are not an acceptable approximation to Wannier functions.

The body-centered tetragonal (BCT) structure of RbO_2 is shown in Fig. 9.1. This is actually only the symmetrized structure. Below 194 K there are several phase transitions where the structure undergoes minor distortions from the BCT structure [152]. In this chapter we examine the ordering of the $2p$ antibonding π_x^* and π_y^* orbitals and how this ordering is frustrated, which is likely the cause of the complexity of the low T phase diagram.

9.2 Tight Binding Hamiltonian

DFT-LDA calculations were performed using the ABINIT code [103] and the FPLO code [22]. Abinit was used to do structural relaxation at each volume, using the PBE GGA functional [2], and FPLO with PZ LDA [3] was used with the relaxed parameters to produce band structures for tight-binding fits.

The LDA spin-unpolarized band structure and density of states for the experimental $P = 0$ volume V_0 are shown in Fig. 9.2. The conduction band character is composed primarily of the two O_2 π^* orbitals, and other bands are well separated. From a band structure point of view, RbO_2 is definitely a molecular solid. Spin-polarized calculations show a half-metallic ferromagnet, however this is in complete disagreement with experiment, where the material is insulating and antiferromagnetic with $T_N = 20K$. Supercell

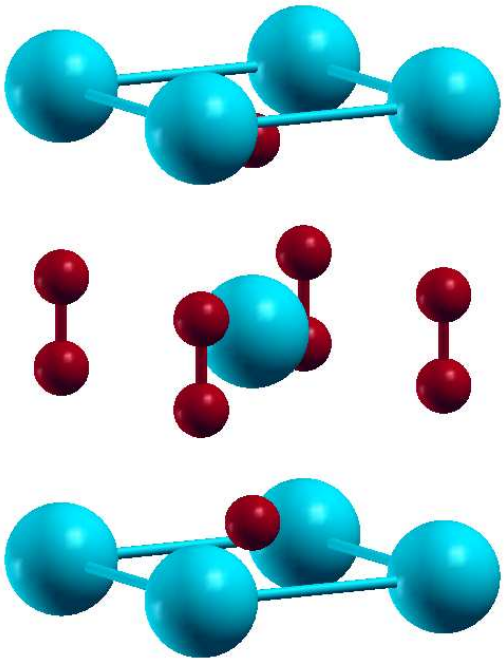

Figure 9.1: Structure of RbO_2. Red atoms are O, blue are Rb. The structure is body centered tetragonal.

calculations have been reported to reveal the antiferromagnetic nature of RbO_2 [153], however they are still metallic. At a compression of $V = 0.65V_0$, shown in Fig. 9.3, the π^* bands have broadened but their dispersion is not significantly altered. Notably, at this higher pressure the gap above the π^* bands has actually increased, and the π and σ bands below the conduction bands have become more dispersive. At compressions somewhat above this, the π^* bands begin to overlap the π bands and the tight-binding fit does not agree quite so well.

A schematic for the hopping channels used in the tight-binding model is shown in Fig. 9.4. To investigate orbital ordering, we construct the Hamiltonian in a cell whose base is $\sqrt{2}a \times \sqrt{2}a$. The lattice vectors for this cell are monoclinic, being $(a, a, 0)$, $(a, -a, 0)$, $(a/2, a/2, c/2)$. For convenience, we define the following $\mathbf{k}$-dependent tight-binding quan-

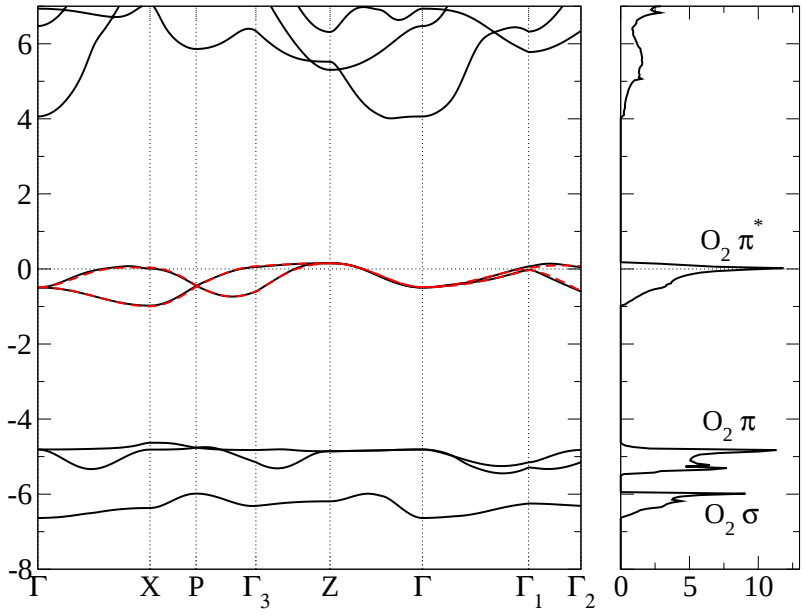

Figure 9.2: Band structure and density of states from spin unpolarized LDA calculation at $V = V_0$, the experimental $P = 0$ volume. Conduction electrons are composed of molecular O_2 anti-bonding π^* orbitals. The unoccupied bands above the gap are mostly O_2 σ^* and Rb $5s$ and $4d$ character. The tight binding fit of Table 9.1 is shown in dashed red, with excellent agreement.

tities:

$$H_z^{\pm}(\mathbf{k}) = -2t_z \cos\left(\frac{k_x a \pm k_y a}{2}\right) \cos\frac{k_z c}{2} \tag{9.1}$$

$$H_{xx}^{11}(\mathbf{k}) = -2t' \left[\cos(k_x a + k_y a) + \cos(k_x a - k_y a)\right] \tag{9.2}$$

$$H_{xx}^{12}(\mathbf{k}) = -2t_\sigma \cos(k_x a) - 2t_\pi \cos(k_y a) - 2t_{\pi 3} \cos(2k_y a) \tag{9.3}$$

$$H_{yy}^{12}(\mathbf{k}) = -2t_\sigma \cos(k_y a) - 2t_\pi \cos(k_x a) - 2t_{\pi 3} \cos(2k_x a) \tag{9.4}$$

$$H_{xy}^{11}(\mathbf{k}) = -2t_{xy} \left[\cos(k_x a + k_y a) - \cos(k_x a - k_y a)\right] \tag{9.5}$$

$$H_{xy}^{\pm}(\mathbf{k}) = -2t_{xy}^z \cos\left(\frac{k_x a \pm k_y a}{2}\right) \cos\frac{k_z c}{2}. \tag{9.6}$$

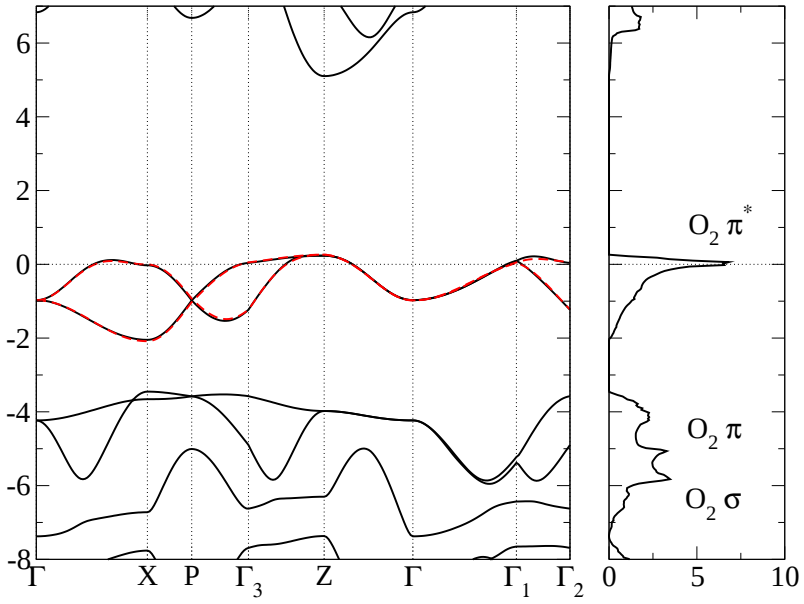

Figure 9.3: Band structure and density of states from spin unpolarized LDA calculation at $V = 0.65V_0$. Comparing with Fig. 9.2, bands are broadened, and the gap above the conduction band is increased. The tight binding fit of Table 9.1 is shown in dashed red, again with excellent agreement. The O_2 σ bands have gained considerable dispersion in the z direction, as seen along the Γ-Z line.

The 4×4 Hamiltonian for the supercell is then

$$H = \begin{bmatrix} \varepsilon_x + H_{xx}^{11} + H_z^+ & H_{xy}^{11} + H_{xy}^+ & H_{xx}^{12} + H_z^- & H_{xy}^- \\ H_{xy}^{11} + H_{xy}^+ & \varepsilon_y + H_{xx}^{11} + H_z^+ & H_{xy}^- & H_{yy}^{12} + H_z^- \\ H_{xx}^{12} + H_z^- & H_{xy}^- & \varepsilon_x + H_{xx}^{11} + H_z^+ & H_{xy}^{11} + H_{xy}^+ \\ H_{xy}^- & H_{yy}^{12} + H_z^- & H_{xy}^{11} + H_{xy}^+ & \varepsilon_y + H_{xx}^{11} + H_z^+ \end{bmatrix} \tag{9.7}$$

with ε_x and ε_y as the energy levels of the π_x^* and π_y^* orbitals (which are equivalent for the purposes of this discussion). The $\mathbf{k}$-dependence of the tight-binding quantities has been suppressed for clarity. The 2×2 Hamiltonian for the primitive unit cell H_p is

$$H_p = \begin{bmatrix} \varepsilon_x + H_{xx}^{11} + H_z^+ + H_{xx}^{12} + H_z^- & H_{xy}^{11} + H_{xy}^- + H_{xy}^+ \\ H_{xy}^{11} + H_{xy}^- + H_{xy}^+ & \varepsilon_y + H_{xx}^{11} + H_z^+ + H_{xx}^{12} + H_z^- \end{bmatrix}. \tag{9.8}$$

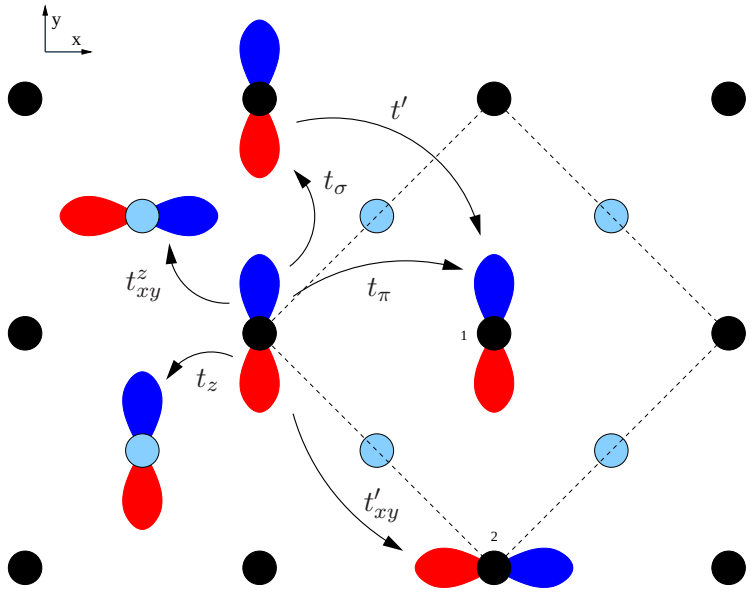

Figure 9.4: Schematic of tight-binding hoppings, looking down on the x-y plane. Black and light blue atoms are O_2 molecular centers, with the light blue atoms being positioned in planes at a distance of $c/2$ above and below the plane of black atoms. The orbitals pictured are π^*_x and π^*_y orbitals, which from top-down appear as p-orbitals. The hopping t'_z (not pictured) is in the z direction, of a distance c. The base of the $\sqrt{2} \times \sqrt{2}$ unit cell described in the text is shown with the dotted line, and the two atoms in the unit cell are marked 1 and 2.

The optimized cell parameters and hoppings are shown in Table 9.1, and the hoppings are plotted in Fig. 9.5. The bond length in the O_2 molecule is 1.21 Å, and in the peroxide ion O_2^{2-} (in hydrogen peroxide) 1.49 Å[154], and the O_2 bond length in RbO_2 is 1.35 Å at ambient pressure, giving the confirmation of the charge state of the O_2 ion as -1. The largest hopping is t^z_{xy}, which represents hopping between layers and from π^*_x to π^*_y orbitals. There are 8 neighbors which participate in this hopping, compared to 2 each for t_σ and t_π, thus since $8|t^z_{xy}| >> 2|t_\sigma| + 2|t_\pi|$, this would suggest that the strongest AFM coupling is between layers. It is not known what type of AFM ordering actually takes place in RbO_2.

	Structure			Tight Binding						
V	a	c/a	d_{O-O}	t^z_{xy}	t_σ	t_π	t_z	t'	t_{xy}	t'_z
0.6	3.409	1.782	1.307	136	-94	-84	77	59	59	20
0.65	3.508	1.772	1.316	130	-86	-86	78	61	56	16
0.7	3.602	1.762	1.323	114	-77	-73	69	49	45	12
0.75	3.693	1.752	1.330	102	-71	-59	61	42	38	11
0.8	3.780	1.743	1.334	92	-66	-50	55	35	32	9
0.85	3.863	1.735	1.338	83	-61	-42	50	30	27	8
0.9	3.943	1.727	1.341	76	-57	-36	46	26	23	6
0.95	4.019	1.721	1.344	70	-53	-32	43	23	20	6
1	4.092	1.717	1.346	64	-50	-28	40	21	17	5
1.05	4.159	1.717	1.348	59	-47	-26	37	19	15	4
1.1	4.189	1.760	1.350	53	-47	-27	34	20	14	3

Table 9.1: Optimized cell parameters and tight binding coefficients. Volume is expressed as fraction of the experimental $P = 0$ volume. Units for a and the O_2 bond length are Å. Units for tight-binding parameters are meV.

9.3 Poor Man's LDA+U method

Since standard electronic structure codes use atomic projections for correlations, they cannot be used to perform LDA+U using the molecular orbitals of RbO_2. Given the tight-binding fit of the previous section, we can construct a poor man's LDA+U method which acts on the Wannier functions we have constructed. We construct a new energy functional as

$$E_{\rm tot} = \sum_{\mathbf{k}n} \varepsilon_{\mathbf{k}n} + E_U \tag{9.9}$$

$$E_U = U \sum_{i,\alpha} n_{i\alpha\uparrow} n_{i\alpha\downarrow} + U' \sum_{i\sigma\sigma'} n_{ix\sigma} n_{iy\sigma'} \tag{9.10}$$

where i is a site index and $\alpha = x, y$ is an orbital index. U and U' are Hubbard parameters introduced here. The physical regime is expected to be where $U > U'$ at all volumes. The orbital potential obtained from $\partial E_{\rm tot}/\partial n_{i\alpha\sigma}$ is then

$$V_{i\alpha\sigma} = U n_{i\alpha,-\sigma} + U' \sum_{\sigma} n_{i,-\alpha,\sigma} \tag{9.11}$$

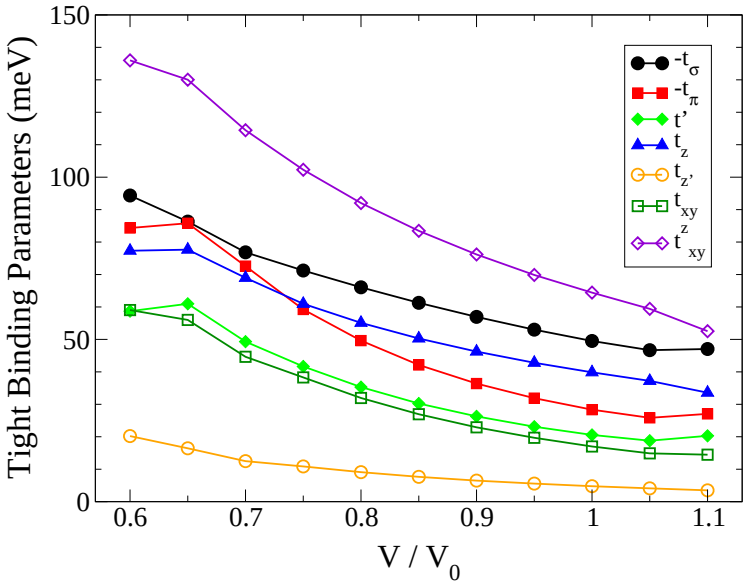

Figure 9.5: Plot of tight-binding parameters vs. volume. Note that the magnitude of t_σ and t_π are plotted. The largest parameter at all volumes is t^z_{xy}, the nearest neighbor hopping between π^*_x and π^*_y orbitals. The change in trend at $V < 0.65V_0$ is the result of the interaction between the π^* and π bands as the gap between them closes, and the tight-binding fit becoming less accurate.

where $-\alpha$ is used to denote 'the other orbital' on site i and σ denotes the spin projection. One then takes the $n_{i\alpha,-\sigma}$ as mean-field variables, and iterates the eigenvectors of the Hamiltonian $H = H_{\mathrm{TB}} + V$ to convergence, recomputing the n values after each iteration to reconstruct the potential matrix for the next iteration. Two considerations must be taken into account in practice, (1) double counting of the potential, and (2) the tendency to reach a local minimum rather than the desired absolute minimum. The potential ends up being double counted because the application of the potential V changes the eigenvalues, so one must subtact $\mathrm{Tr}(Vn) = 2E_U$ from (9.9). To properly find a global minimum, one must converge this method several times, using different starting guesses for the orbital occupations, and then compare the total energies that come out of each result to see which is lowest.

The general trend for U in $4f$ and $3d$ atomic orbitals is for U to get smaller as l gets smaller. A typical value of U for $3d$ orbitals is 5-6 eV, so a reasonable U for $2p$

orbitals might be around 2-3 eV. Molecular π^* orbitals are not as localized as atomic p orbitals, so a reasonable value of U would be around 1-2 eV. Since the bandwidth of the π^* orbitals in RbO_2 is about 1 eV, it is reasonable to expect correlated behavior here. The phase diagrams for this LDA+U method for U and U' from 0 to 2 eV at three selected volumes are shown in Figs. 9.6. Two different kinds of orbital ordering were actually found, they are termed XY and XX ordering. XY ordering is composed of the holes in each plane occupying orbitals π_x^* on one atom, and π_y^* on all neighboring atoms (in the plane). This minimizes the Coulomb repulsion between orbitals in the plane, but frustrates the interaction between planes (the intraplane interaction is between the black and light blue atoms in Fig. 9.4). The XX ordering is where the holes occupy π_x^* orbitals on every O_2 molecule. (YY ordering would be equivalent to XX ordering, so no distinction is made between them.) This eliminates the frustration between the planes at the cost of frustrating the orbitals in the plane. This ordering should not be too surprising, because the the nearest neighbors of each O_2 molecule are the ones above and below in separate planes. There are eight nearest neighbors, compared to four second neighbors. So the cost for unfrustrating these eight bonds will be comparable to the cost of frustrating two of the four second neighbor bonds, and with the right parameter choices the XX ordering will show up. One must be careful about overly trusting the XX/XY distinction. Along the line $U = U'$, the two orderings are degenerate, and away from this line the energy difference between these two phases is on the order of 1 meV = 12 K. This is coincident with the temperature scale of the several minor structural phase changes that occur at low temperatures. It is likely that these phase changes are occuring as a result of this frustration.

Since the physically realistic parameters are estimated to be 1-2 eV with $U > U'$, this model predicts that RbO_2 will be an antiferromagnetic insulator with XX ordering. As volume is decreased, the bandwidth W increases and one might also expect U and U' to decrease as the Wannier functions become less localized. Thus, as pressure is applied RbO_2 is expected to go first through a metal-insulator transition to become metallic and then

a magnetic transition from AFM to FM ordering might occur. Whether RbO_2 becomes a half-metal or not will be somewhat sensitive to the parameters U and U', and the possibility of the magnetic transition being from AFM to PM is not excluded.

Shown in Fig. 9.7 are several plots of the density of states for the poor man's LDA+U method for selected parameters. Fig. 9.7a shows the DOS of an XY ordered antiferromagnet. The unoccupied spin-up states are the π_x^* orbital on one molecule, and the unoccupied spin-down states are the π_y^* orbital on the other. In this phase the magnetic ordering is intimately tied to the orbital ordering. This is true for the XX antiferromagnet, shown in Fig. 9.7b. In the XX AFM phase, the π_y^* orbitals form normal band states, but the π_x^* orbitals split into Hubbard bands. There is a similar effect in the XY AFM phase, however there a particular pair of π_x^* and π_y^* orbitals form band-like states, and the other pair forms Hubbard bands. The 'beginning' of this behavior is seen in Fig. 9.7e, where the U and U' parameters are large enough for orbital ordering, but not large enough to create an insulating state. Here the π_x^* and π_y^* orbitals that are partially occupied split in a manner consistent with creating an XY insulator, so one can imagine that as the parameters are turned up the DOS will smoothly evolve into that of Fig. 9.7a. The beginnings of AFM ordering are seen too, as the π_x^* and π_y^* orbitals are a little bit spin split in opposite directions. Fig. 9.7f shows how this looks once AFM ordering has set in, but the system is not yet insulating. There is clear orbital ordering as well as antiferromagnetism, but no gap.

The graphs in Fig. 9.7 that have not been discussed so far all show metallic solutions. Fig. 9.7c shows the half-metallic phase that spin-polarized LDA produces. In this region, the Hubbard U is essentially acting as the effective Stoner I of LSDA. Fig. 9.7d shows the FM metal, just before half-metallic state sets in. Fig. 9.7g shows the 'orphaned' XX ordered metallic phase seen in the lower right of Fig. 9.6a. This phase is distinct from both its XY-ordered neighbors in Figs. 9.7e and 9.7f, and it's also distinct from its XX-ordered cousin shown in Fig. 9.7b. The XX insulator has π_x^* states above the gap, and π_y^* states below the gap, but for the XX metal all states near the Fermi energy are π_x^* states.

9.4 Conclusion

We have examined the ground-state U-U' phase diagram of LDA+U applied to an effective tight-binding Hamiltonian for RbO_2. Several magnetic and orbital-ordered phases are seen. Two kinds of orbital ordering are seen, depending on which of U and U' is larger. Since the physical regime is where $U > U'$, this model predicts that XX ordering will be dominant over XY ordering. These two orderings are nearly degenerate, reflecting the frustration of the orbital ordering. AFM magnetic ordering is seen at reasonable values of the parameters.

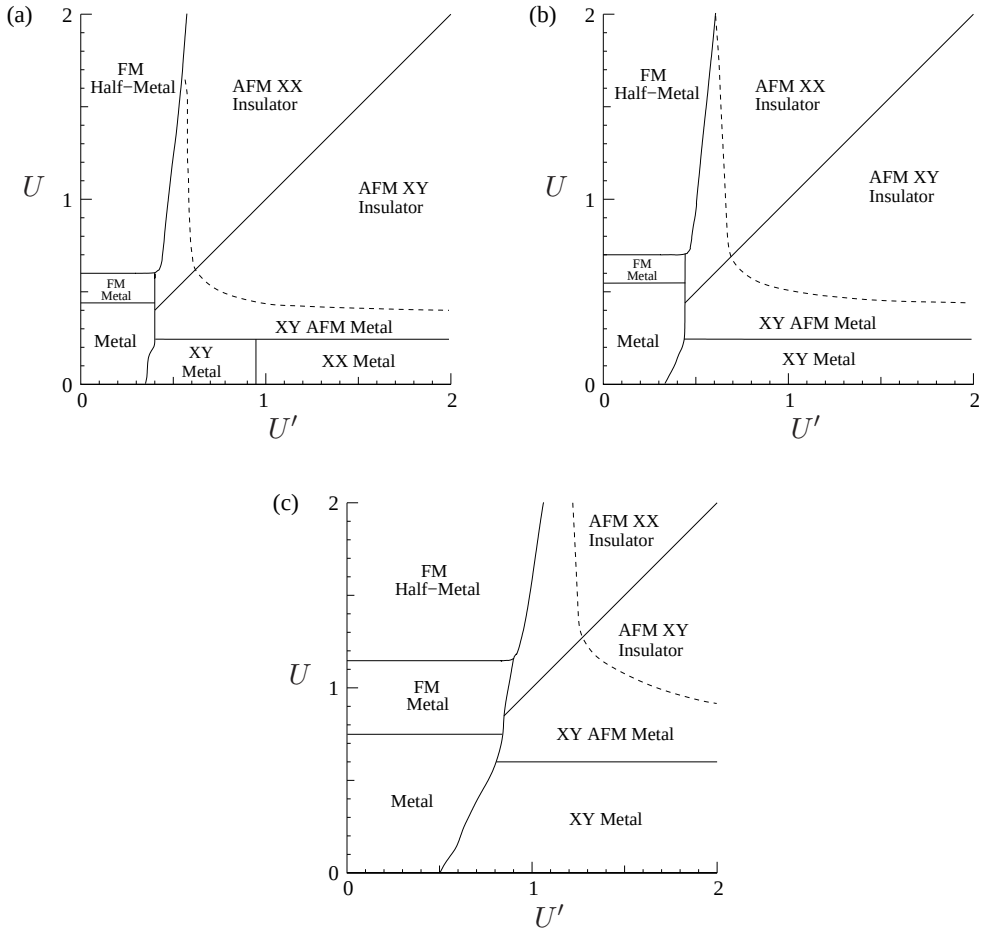

Figure 9.6: U-U' phase diagram produced by the LDA+U method described in text for volumes (a) $1.1V_0$ (b) V_0 and (c) $0.65V_0$. The dashed line indicates where the gap is 0.1 eV, where the gap increases in the upper right direction. The unmarked phase to the left of the dashed line and to the right of the FM half-metallic phase in an XX ordered metal, at all volumes.

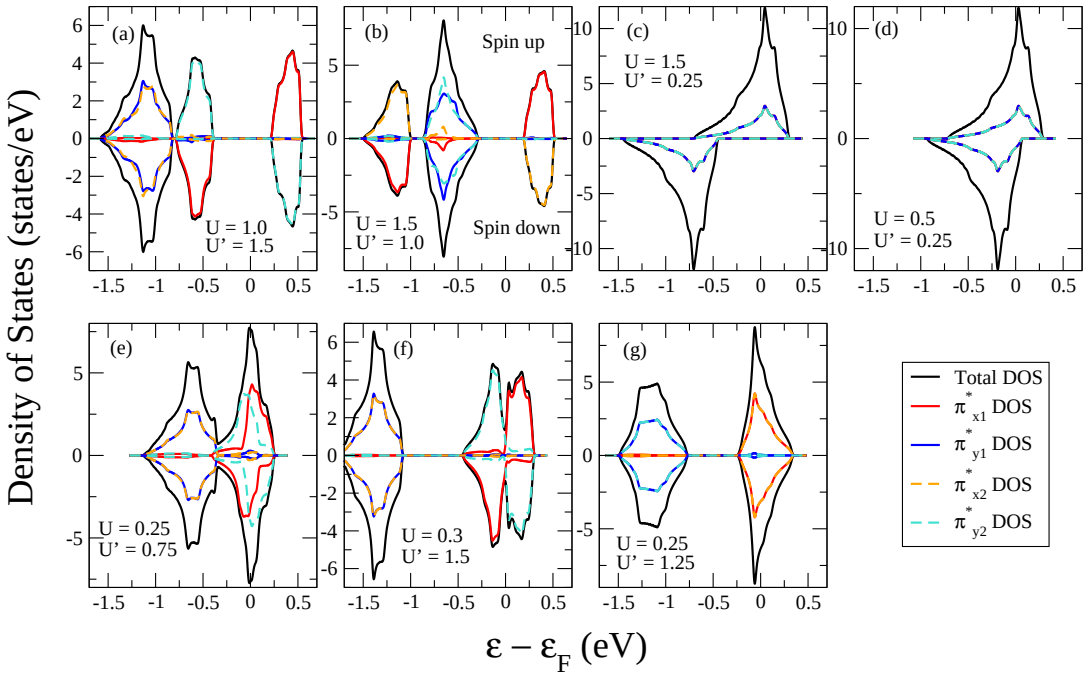

Figure 9.7: Full and projected density of states for selected values of U and U', measured relative to the Fermi energy at $V = 1.1V_0$. Orbitals on atom 1 are colored solid lines, and orbitals on atom 2 are colored dashed lines. (a) is an XY ordered AFM insulator. The unoccupied states are composed of π_x^* orbitals one one O_2 molecule, and π_y^* orbitals on the other O_2 molecule. (b) shows an XX ordered AFM insulator (or small gap semiconductor). The unoccupied states are the x orbitals on each O_2 molecule. (c) shows a ferromagnetic half-metal, which is the same solution as given by spin-polarized LDA. All orbital occupations are equal. (d) shows a ferromagnetic metal. (e) shows an XY ordered metal. The unoccupied states are the π_x^* orbital on atom 1, and the π_y^* on atom 2. (f) shows an XY ordered AFM metal. (g) shows an XX ordered metal. The unoccupied states are composed entirely of π_x^* orbitals on both atoms.

Bibliography

[1] W. Kohn and L. J. Sham. Self-consistent equations including exchange and correlation effects. *Phys. Rev.*, 140:A1133, 1965.

[2] John P. Perdew, Kieron Burke, and Matthias Ernzerhof. Generalized gradient approximation made simple. *Phys. Rev. Lett.*, 77(18):3865–3868, Oct 1996.

[3] J. P. Perdew and Alex Zunger. Self-interaction correction to density-functional approximations for many-electron systems. *Phys. Rev. B*, 23(10):5048–5079, May 1981.

[4] S. Yu. Savrasov. Linear response calculations of lattice dynamics using muffin-tin basis sets. *Phys. Rev. Lett.*, 69(19):2819–2822, Nov 1992.

[5] Xavier Gonze, Douglas C. Allan, and Michael P. Teter. Dielectric tensor, effective charges, and phonons in α-quartz by variational density-functional perturbation theory. *Phys. Rev. Lett.*, 68(24):3603–3606, Jun 1992.

[6] M. H. Hettler, M. Mukherjee, M. Jarrell, and H. R. Krishnamurthy. Dynamical cluster approximation: Nonlocal dynamics of correlated electron systems. *Phys. Rev. B*, 61(19):12739–12756, May 2000.

[7] Edward Teller. On the stability of molecules in the Thomas-Fermi theory. *Rev. Mod. Phys.*, 34(4):627–631, Oct 1962.

[8] Richard M. Martin. *Electronic Structure*. The Press Syndicate of the University of Cambridge, 2004.

[9] P. Hohenberg and W. Kohn. Inhomogeneous electron gas. *Phys. Rev.*, 136(3B):B864–B871, Nov 1964.

[10] D. M. Ceperley and B. J. Alder. Ground state of the electron gas by a stochastic method. *Phys. Rev. Lett.*, 45(7):566–569, Aug 1980.

[11] S. H. Vosko, L. Wilk, and M. Nusair. Accurate spin-dependent electron liquid correlation energies for local spin density calculations: a critical analysis. *Can. J. Phys.*, 58:1200, 1980.

[12] S. Goedecker, M. Teter, and J. Hutter. Separable dual-space Gaussian pseudopotentials. *Phys. Rev. B*, 54(3):1703–1710, Jul 1996.

[13] John P. Perdew and Yue Wang. Accurate and simple representation of the electron-gas correlation energy. *Phys. Rev. B*, 45(23):13244, 1992.

[14] Yingkai Zhang and Weitao Yang. Comment on Generalized Gradient Approximation Made Simple. *Phys. Rev. Lett.*, 80(4):890, Jan 1998.

[15] John P. Perdew, Adrienn Ruzsinszky, Gábor I. Csonka, Oleg A. Vydrov, Gustavo E. Scuseria, Lucian A. Constantin, Xiaolan Zhou, and Kieron Burke. Restoring the density-gradient expansion for exchange in solids and surfaces. *Phys. Rev. Lett.*, 100(13):136406, 2008.

[16] Xavier Gonze. First-principles responses of solids to atomic displacements and homogeneous electric fields: Implementation of a conjugate-gradient algorithm. *Phys. Rev. B*, 55(16):10337–10354, 1997.

[17] Xavier Gonze and Changyol Lee. Dynamical matrices, Born effective charges, dielectric permittivity tensors, and interatomic force constants from density-functional pertubation theory. *Phys. Rev. B*, 55(16):10355–10368, 1997.

[18] N. Troullier and J. L. Martins. Efficient pseudopotentials for plane-wave calculations. *Phys. Rev. B*, 43(3):1993, 1991.

[19] Alex Zunger and Marvin L. Cohen. First-principles nonlocal-pseudopotential approach in the density-functional formalism: Development and application to atoms. *Phys. Rev. B*, 18(10):5449–5472, Nov 1978.

[20] Steven G. Louie, Sverre Froyen, and Marvin L. Cohen. Nonlinear ionic pseudopotentials in spin-density-functional calculations. *Phys. Rev. B*, 26(4):1738–1742, Aug 1982.

[21] G. B. Bachelet, D. R. Hamann, and M. Schlüter. Pseudopotentials that work: From H to Pu. *Phys. Rev. B*, 26(8):4199–4228, Oct 1982.

[22] Klaus Koepernik and Helmut Eschrig. Full-potential nonorthogonal local-orbital minimum-basis band-structure scheme. *Phys. Rev. B*, 59(3):1743–1757, Jan 1999.

[23] Nicola Marzari and David Vanderbilt. Maximally localized generalized wannier functions for composite energy bands. *Phys. Rev. B*, 56(20):12847–12865, Nov 1997.

[24] Ivo Souza, Nicola Marzari, and David Vanderbilt. Maximally localized wannier functions for entangled energy bands. *Phys. Rev. B*, 65(3):035109, Dec 2001.

[25] Wei Ku, H. Rosner, W. E. Pickett, and R. T. Scalettar. Insulating ferromagnetism in $La_4Ba_2Cu_2O_10$: An *ab initio* Wannier function analysis. *Phys. Rev. Lett.*, 89(16):167204, 2002.

[26] Erik R. Ylvisaker and Warren E. Pickett. First-principles study of the electronic and vibrational properties of $LiNbO_2$. *Phys. Rev. B*, 74:075104, 2006.

[27] W. Kohn. Analytic properties of Bloch waves and Wannier functions. *Phys. Rev.*, 115(4):809, 1959.

[28] Neil W. Ashcroft and N. David Mermin. *Solid State Physics*. Thomson Learning, Inc., 1976.

[29] Walter A. Harrison. *Solid State Theory*. General Publishing Company, Ltd., 1979.

[30] Vladimir I. Anisimov, Jan Zaanen, and Ole K. Andersen. Band theory and Mott insulators: Hubbard u instead of Stoner i. *Phys. Rev. B*, 44(3):943–954, Jul 1991.

[31] S. L. Dudarev, G. A. Botton, S. Y. Savrasov, C. J. Humphreys, and A. P. Sutton. Electron-energy-loss spectra and the structural stability of nickel oxide: An LSDA+U study. *Phys. Rev. B*, 57(3):1505–1509, Jan 1998.

[32] A. G. Petukhov, I. I. Mazin, L. Chionel, and A. I. Lichtenstein. Correlated metals and the LDA+U method. *Phys. Rev. B*, 67:153106, 2003.

[33] A. I. Liechtenstein, V. I. Anisimov, and J. Zaanen. Density-functional theory and strong interactions: Orbital ordering in Mott-Hubbard insulators. *Phys. Rev. B*, 52(8):R5467–R5470, Aug 1995.

[34] Deepa Kasinathan, Klaus Koepernik, and Warren E. Pickett. Pressure-driven magnetic moment collapse in the ground state of MnO. *New J. Phys.*, 9:235, 2007.

[35] K.-W. Lee and W. E. Pickett. Infinite-layer $LaNiO_2$: Ni^{1+} is not Cu^{2+}. *Phys. Rev. B*, 70(16):165109, Oct 2004.

[36] V. I. Anisimov, I. V. Solovyev, M. A. Korotin, M. T. Czyżyk, and G. A. Sawatzky. Density-functional theory and NiO photoemission spectra. *Phys. Rev. B*, 48(23):16929–16934, Dec 1993.

[37] M. T. Czyżyk and G. A. Sawatzky. Local-density functional and on-site correlations: The electronic structure of La_2CuO_4 and $LaCuO_3$. *Phys. Rev. B*, 49(20):14211–14228, May 1994.

[38] V. I. Anisimov, F. Aryasetiawan, and A. I. Lichtenstein. First-principles calculations of the electronic structure and spectra of strongly correlated systems: the lda+u method. *J. Phys.: Condens. Matter*, 9:767, 1997.

[39] W. E. Pickett, C. Erwin, and E. C. Ethridge. Reformulation of the LDA+U method for a local orbital basis. *Phys. Rev. B*, 58:1201, 1998.

[40] I. V. Solovyev, P. H. Dederichs, and V. I. Anisimov. Corrected atomic limit in the local-density approximation and the electronic structure of d impurities in Rb. *Phys. Rev. B*, pages 16861–16871, 1994.

[41] Peter Blaha, Karlheinz Schwarz, Georg Madsen, Dieter Kvasnicka, and Joachim Luitz. *Wien2k Userguide*, 2001.

[42] A. B. Shick, W. E. Pickett, and A. I. Liechtenstein. Ground and metastable states in gamma-Ce from correlated band theory. *J. Electron Spectrosc. and Related Phen.*, 114-116:753, 2001.

[43] M. D. Johannes and W. E. Pickett. Magnetic coupling between nonmagnetic ions: Eu^{3+} in EuN and EuP. *Phys. Rev. B*, 72:195116, 2005.

[44] P. Larson, Walter R. L. Lambrecht, A. Chantis, and M. van Schilfgaarde. Electronic structure of rare-earth nitrides using the LSDA+U approach: Importance of allowing $4f$ orbitals to break the cubic crystal symmetry. *Phys. Rev. B*, 75:045114, 2007.

[45] G. A. Wigger, F. Baumberger, Z.-X. Shen, Z. P. Yin, W. E. Pickett, S. Maquilon, and Z. Fisk. Electronic band structure and kondo coupling in $YbRh_2Si_2$. *Phys. Rev. B*, 76:035106, 2007.

[46] V. I. Anisimov, M. A. Korotin, J. Zaanen, and O. K. Andersen. Spin bags, polarons, and impurity potentials in $La_{2-x}Sr_xCuO_4$ from first principles. *Phys. Rev. Lett.*, 65:345, 1992.

[47] A. N. Yaresko, A. Y. Perlov, R. Hayn, and H. Rosner. Exchange integrals of $Sr_2CuO_2Cl_2$ and $Ba_2Cu_3O_4Cl_2$ from LDA+U calculations. *Phys. Rev. B*, 65:115111, 2002.

[48] R. E. Cohen, I. I. Mazin, and D. G. Isaak. Magnetic collapse in transition metal oxides at high pressure: Inplications for the earth. *Science*, 275:654, 1997.

[49] Vladimir I. Anisimov, Pieter Kuiper, and Joseph Nordgren. First-principles calculation of NiO valence spectra in the impurity-anderson-model approximation. *Phys. Rev. B*, 50:8257, 1994.

[50] A. B. Shick, A. I. Liechtenstein, and W. E. Pickett. Implementation of the LDA+U method using the full-potential linearized augmented plane-wave basis. *Phys. Rev. B*, 60:10763, 1999.

[51] O. Bengone, M. Alouani, P Blchl, and J. Hugel. Implementation of the projector augmented-wave LDA+U method: Application to the electronic structure of NiO. *Phys. Rev. B*, 62:16392, 2000.

[52] L. V. Dobysheva, P. L. Potapov, and D. Schryvers. Electron-energy-loss spectra of NiO. *Phys. Rev. B*, 69:184404, 2004.

[53] P. Mohn, C. Persson, P. Blaha, K. Schwarz, and H. Eschrig. Correlation induced paramagnetic ground state in FeAl. *Phys. Rev. Lett.*, 87:196401, 2001.

[54] F. Lechermann, M. Fhnle, B. Meyer, and C Elssser. Electronic correlations, magnetism and structure of Fe-Al subsystems: An LDA+U study. *Phys. Rev. B*, 69:165116, 2004.

[55] K.-W. Lee, J. Kune, and W. E. Pickett. Charge disproportionation and spin ordering tendencies in Na_xCoO_2. *Phys. Rev. B*, 70:045104, 2004.

[56] K.-W. Lee and W. E. Pickett. Correlation effects in the high formal oxidation-state compound Sr_2CoO_4. *Phys. Rev. B*, 73:174428, 2006.

[57] B. N. Harmon, V. P. Antropov, A. I. Liechtenstein, I. V. Solovyev, and V. I. Anisimov. Calculation of magneto-optical properties for $4f$ systems: LSDA + Hubbard U results. *J. Phys. Chem. Solids*, 56:1521, 1995.

[58] S. Abdelouahed, N. Baadji, and M. Alouani. Electronic structure and x-ray magnetic circular dichroism of gadolinium beyond the local spin density approximation. *Phys. Rev. B*, 75:094428, 2007.

[59] P. M. Oppeneer, V. N. Antonov, A. Ya. Perlov, A. N. Yaresko, T. Kraft, and H. Eschrig. Theory of the optical and magneto-optical spectra of cerium and uranium coumpounds. *Physica B*, 230-232:544, 1997.

[60] H. Harima and K. Takegahara. Fermi surfaces of $PrOs_4Sb_{12}$ based on the LDA+U method. *Physica B*, 359-361:920, 2005.

[61] G. A. Wigger, F. Baumberger, Z.-X. Shen, Z. P. Yin, W. E. Pickett, S. Maquilon, and Z. Fisk. Electronic band structure and kondo coupling ini $YbRh_2Su_2$. *Phys. Rev. B*, 76:035106, 2007.

[62] J. Bouchet, B. Siberchicot, F. Jollet, and A. Pasturel. Equilibrium properties of δ-Pu: LDA+U calculations (LDA $\equiv$ local density approximation). *J. Phys.: Condens. Matter*, 12:1723, 2000.

[63] S. Y. Savrasov and G. Kotliar. Ground state theory of δ-Pu. *Phys. Rev. Lett.*, 84:3670, 2000.

[64] D. L. Price, B. R. Cooper, S.-P. Lim, and I. Avgin. Variation of the LDA+U method appropriate to f-state localization: Application to magneto-optical properties. *Phys. Rev. B*, 61:9867, 2000.

[65] A. B. Shick, V. Drchal, and L. Havela. Coulomb-U and magnetic-moment collapse in δ-Pu. *Europhysics Letters*, 69:588, 2005.

[66] A. O. Shorikov, A. V. Lukoyanov, M. A. Korotin, and V. I. Anisimov. Magnetic state and electronic structure of the δ and α phases of metallic Pu and its compounds. *Phys. Rev. B*, 72:024458, 2005.

[67] J. F. Janak. Uniform susceptibilities of metallic elements. *Phys. Rev. B*, 16:255, 1977.

[68] D.-K. Seo. Density functional perturbational orbital theory of spin polarization in electronic systesm. i. formalism. *J. Chem. Phys.*, 125:154105, 2006.

[69] Antoine Georges. Strongly correlated electron materials: dynamical mean-field theory and electronic structure. *arxiv:cond-mat/0403123*, 2007.

[70] Antoine Georges, Gabriel Kotliar, Werner Krauth, and Marcelo J. Rozenberg. Dynamical mean-field theory of stongly correlated fermion systems and the limit of infinite dimensions. *Rev. Mod. Phys.*, 68(1):13–125, 1996.

[71] G. Kotliar, S. Y. Savrasov, K. Haule, V. S. Oudovenko, O. Parcollet, and C. A. Marianetti. Electronic structure calculations with dynamical mean-field theory. *Rev. Mod. Phys.*, 78:865–951, 2006.

[72] Kristjan Haule. *Diagrammatic theory of strongly correlated electron systems.* PhD thesis, University of Ljubljana, 2002.

[73] R. Blankenbecler, D. J. Scalapino, and R. L. Sugar. Monte Carlo calculations of coupled Boson-Fermion systems. i. *Phys. Rev. D*, 24(8):2278–2286, Oct 1981.

[74] J. E. Hirsch and R. M. Fye. Monte Carlo method for magnetic impurities in metals. *Phys. Rev. Lett.*, 56(23):2521–2524, Jun 1986.

[75] H. B. Schüttler and D. J. Scalapino. Monte Carlo studies of the dynamics of quantum many-body systems. *Phys. Rev. Lett.*, 55(11):1204–1207, Sep 1985.

[76] H. J. Vidberg and J. W. Serene. Solving the Eliashberg equations by means of n-point Pad approximants. *J. Low Temp. Phys.*, 29:179, 1977.

[77] Grace Wahba. Practical approximate solutions to linear operator equations when the data are noisy. *SIAM Journal on Numerical Analysis*, 14(4):651–667, 1977.

[78] R. N. Silver, D. S. Sivia, and J. E. Gubernatis. Maximum-entropy method for analytic continuation of quantum Monte Carlo data. *Phys. Rev. B*, 41(4):2380–2389, Feb 1990.

[79] Mark Jarrell and Ofer Biham. Dynamical approach to analytic continuation of quantum Monte Carlo data. *Phys. Rev. Lett.*, 63(22):2504–2507, Nov 1989.

[80] M. Jarrell. Hubbard model in infinite dimensions: A quantum monte carlo study. *Phys. Rev. Lett.*, 69(1):168–171, Jul 1992.

[81] R. S. Fishman and M. Jarrell. Magnetic susceptibility of the double-exchange model. *Phys. Rev. B*, 67(10):100403, Mar 2003.

[82] Margret J. Geselbract, Thomas J. Richardson, and Angelica M. Stacy. Superconductivity in the layered compound Li_xNbO_2. *Nature*, 345:324, 325, 1990.

[83] J. Köhler, C. Svensson, and A. Simon. Oxoniobates containing metal clusters. *Angew. Chem. Int. Ed.*, 31:1437–1456, 1992.

[84] M. Veithen and Ph. Ghosez. First-principles study of the dielectric and dynamical properties of lithium niobate. *Phys. Rev. B*, 65:214302, 2002.

[85] V. A. Gasparov, G. K. Strukova, and S. S. Khassanov. *JETP Letters*, 60:440, 1994.

[86] G. K. Strukova, V. V. Kedrov, V. N. Zverev, S. S. Khassanov, I. M. Ovchinnikov, I. E. Batov, and V. A. Gasparov. On the synthesis and the electric and magnetic properties of superconducting barium-niobium-oxide compounds. *Physica C*, 291:207, 1997.

[87] Vitaly A. Gasparov, S. N. Ermolov, G. K. Strukova, N. S. Sidorov, S. S. Khassanov, H.-S. Wang, M. Schneider, E. Glaser, and Wo. Richter. Superconducting and anomalous electron transport properties and electronic structure of $BaNbO_{3-x}$ and $Ba_2Nb_5O_x$ films. *Phys. Rev. B*, 63(17):174512, Apr 2001.

[88] Y. Takano, S. Takayanagi, S. Ogawa, T. Yamadaya, and N. Mori. Superconducting properties of layered perovskite KCa2Nb$_3$o$_1$0 and $KLaNb_2O_7$. *Solid State Communications*, 103:215, 1997.

[89] M. Kato, A. Inoue, I. Nagai, M. Kakihana, A. W. Sleight, and Y. Koike. Superconductivity in the electrochemically li-intercalated niobates with the layered perovskite structure. *Physica C*, 388-389:445, 2003.

[90] J. E. L. Waldron, M. A. Green, and D. A. Neumann. Structure and electronic properties of monoclinic $Nb_{12}O_{29}$. *JPCS*, 65:79, 2004.

[91] E. N. Andersen, T. Klimczuk, V. L. Miller, H. W. Zandbergen, and R. J. Cava. Nanometer structural columns and frustration of magnetic ordering in $Nb_{12}O_{29}$. *Phys. Rev. B*, 72:033413, 2005.

[92] Gerd Meyer and Rudolf Hoppe. The first oxoniobate(iii): $LiNbO_2$. *Angew. Chem. Internat. Edit.*, 13(11), 1974.

[93] Jeremy K. Burdett and Timothy Hughbanks. Aspects of metal-metal bonding in early-transition-metal dioxides. *Inorg. Chem.*, 24:1741–1750, 1985.

[94] Margret J. Geselbracht, Angelica M. Stacy, Armando R. Garcia, Bernard G. Silbernagel, and George H. Kwei. Local environment and lithium ion mobility in $LiNbO_2$: Inferences from structure, physical properties, and NMR. *J. Phys. Chem*, 97:7102, 7103, 7104, 7105, 7106, 7107, 1993.

[95] D. L. Novikov, V. A. Gubanov, V. G. Zubkov, and A. J. Freeman. Electronic structure and electron-phonon interactions in layered Li_xNbO_2 and Na_xNbO_2. *Phys. Rev. B*, 49(22):15830–15835, 1994.

[96] E. G. Moshopoulou, P. Bordet, and J. J. Capponi. Superstructure and superconductivity in Li_{1-x} ($x \approx 0.7$) single crystals. *Phys. Rev. B*, 59(14), 1999.

[97] N. Kumada, S. Watauchi, I. Tanaka, and N. Knomura. Superconductivity of hydrogen inserted $LiNbO_2$. *Materials Research Bulletin*, 35:1743–1746, 2000.

[98] S. Yamanaka, H. Kawaji, K. Hotehama, and M. Ohashi. A new layer-structured nitride superconductor. lithium-intercalated β-zirconium nitride chloride, Li_xZrNCl. *Advanced Materials*, 8:771, 1996.

[99] A. Cros, A. Cantarero, D. Beltrán-Porter, J. Oró-Solé, and A. Fuertes. *Advanced Materials*, 9:771, 1996.

[100] W. E. Pickett, J. M. An, H. Rosner, and S. Y. Savrasov. Role of two dimensionality in MgB_2. *Physica C*, 387:117, 2003.

[101] A. F. McDowell, D. M. Snyderman, Mark S. Conradi, B. G. Silbernagel, and A. M. Stacy. Cross relaxation and atomic motion in $LiNbO_2$. *Phys. Rev. B*, 50(21):15764–15774, 1994.

[102] A. P. Tyutyunnik, D. G. Kellerman V. G. Zubkov, V. A. Pereliaev, and A. E. Kar'kin. Synthesis, superconducting properties and structural (including electron diffraction) studies of Na_xNbO_2 and Li_xNbO_2. *Eur. J. Solid State Inorg. Chem.*, 33:53–65, 1996.

[103] X. Gonze, J.-M. Beuken, R. Caracas, F. Detraux, M. Fuchs, G.-M. Rignanese, L. Sindic, M. Verstraete, G. Zerah, F. Jollet, M. Torrent, A. Roy, M. Mikami, Ph. Ghosez, J.-Y. Raty, and D.C. Allan. First-principles computation of material properties : the ABINIT software project. *Computational Materials Science*, 25:478–492, 2002. The ABINIT code is a common project of the Universit Catholique de Louvain, Corning Incorporated, and other contributors (URL http://www.abinit.org).

[104] Carsten Honerkamp. Instabilities of interacting electrons on the triangular lattice. *Phys. Rev. B*, 68(10):104510, Sep 2003.

[105] A. Kokalj. *J. Mol. Graphics Modelling*, 17:176–179, 1999. Code available from http://www.xcrysden.org/

[106] Ryan L. Barnett, Anatoli Polkovnikov, Eugene Demler, Wei-Guo Yin, and Wei Ku. Coexistence of gapless excitations and commensurate charge-density wave in the 2H-transition metal dichalcogenides. cond-mat/0508590, 2005.

[107] H. T. Stokes and L. L. Boyer. *SMODES program*, 2002. Available from www.physics.byu.edu/~stokesh/isotropy.html

[108] Zhenyu Li, Jinlong Yang, J. G. Hou, and Qingshi Zhu. First-principles lattice dynamics of $NaCoO_2$. *Phys. Rev. B*, 70:144518, 2004.

[109] Kwan-Woo Lee and Warren E. Pickett. Born effective charges and infrared response of LiBC. *Phys. Rev. B*, 68:085308, 2003.

[110] N. E. Christensen and D. L. Novikov. Predicted superconductive properties of lithium under pressure. *Phys. Rev. Lett.*, 86(9):1861–1864, Feb 2001.

[111] Katsuya Shimizu, Hiroto Ishikawa, Daigoroh Takao, Takehiko Yagi, and Kiichi Amaya. Superconductivity in compressed lithium at 20 K. *Nature*, 419:597, 2002.

[112] D. Kasinathan, K. Koepernik, J. Kunes, H. Rosner, and W. E. Pickett. Origin of strong coupling in lithium under pressure. *Physica C*, 2006. In Press.

[113] Katsuya Shimizu, Kiichi Amaya, and Naoshi Suzuki. Pressure-induced superconductivity in elemental materials. *J. Phys. Soc. Japan*, 74:1345, 2005.

[114] Takahiro Yabuuchi, Takahiro Matsuoka, Yuki Nakamoto, and Katsuya Shimizu. Superconductivity of Ca exceeding 25 K at megabar pressures. *J. Phys. Soc. Japan*, 75:083703, 2006.

[115] J. J. Hamlin, V. G. Tissen, , and J. S. Schilling. Superconductivity at 17 K in yttrium metal under nearly hydrostatic pressures up to 89 GPa. *Phys. Rev. B*, 73:094522, 2006.

[116] Z. P. Yin, S. Y. Savrasov, and W. E. Pickett. Strong electron-phonon coupling in yttrium under pressure. *Phys. Rev. B*, 74:094519, 2006.

[117] Takahiro Yabuuchi, Yuki Nakamoto, Katsuya Shimizu, and Takumi Kikegawa. New high-pressure phase of calcium. *J. Phys. Soc. Japan*, 74:2391, 2005.

[118] Rajeev Ahuja, Olle Eriksson, J. M. Wills, and Börje Johansson. Theoretical confirmation of the high pressure simple cubic phase in calcium. *Phys. Rev. Lett.*, 75:3473, 1995.

[119] Eugene Gregoryanz, Olga Degtyareva, Maddury Somayazulu, Russell J. Hemley, and Ho kwang Mao. Melting of dense sodium. *Phys. Rev. Lett.*, 94(18):185502, 2005.

[120] Eduardo R. Hernández and Jorge Iniguez. First-principles simulations on the nature of the melting line of sodium. *Phys. Rev. Lett.*, 98(5):055501, 2007.

[121] Jean-Yves Raty, Eric Schwegler, and Stanimir A. Bonev. Electronic and structural transitions in dense liquid sodium. *Nature*, 449:448, 2007.

[122] L. Koči, R. Ahuja, L. Vitos, and U. Pinsook. Melting of Na at high pressure from ab initio calculations. *Phys. Rev. B*, 77(13):132101, 2008.

[123] G. G. N. Angilella, N. H. March, and R. Pucci. Melting curve $T_m(p)$ of sodium under pressure p: transition from a wigner-like nuclear bcc structure near 30 GPa to lower symmetry states with negative dt_m/dp at higher pressures. *Phys. Chem. of Liquids*, 46(1):86, 2008.

[124] Chang-Sheng Zha and Reinhard Boehler. Melting of sodium and potassium in a diamond anvil cell. *Phys. Rev. B*, 31:3199, 1985.

[125] A. K. McMahan, C. Huscroft, R. T. Scalettar, and F. L. Pollock. Volume-collapse transitions in the rare earth metals. *J. Comput.-Aided Mater. Des.*, 5:131, 1998.

[126] A. K. McMahan, K. Held, and R. T. Scalettar. Thermodynamic and spectral properties of compressed Ce calculated using a combined local-density approximation and dynamical mean-field theory. *Phys. Rev. B*, 67:075108, 2003.

[127] A. K. McMahan. Combined local-density and dynamical mean field theory calculations for the compressed lanthanides Ce, Pr, and Nd. *Phys. Rev. B*, 72:115125, 2005.

[128] Luca M. Ghiringhelli, Jan H. Los, Evert Jan Meijer, A. Fasolino, and Daan Frenkel. Modeling the phase diagram of carbon. *Phys. Rev. Letters*, 94:145701, 2005.

[129] Xiaofei Wang, Sandro Scandolo, and Roberto Car. Carbon phase diagram from *ab initio* molecular dynamics. *Phys. Rev. Letters*, 95:185701, 2005.

[130] J. N. Glosli and F. H. Rhee. *J. Chem. Phys.*, 110:441, 1999.

[131] F. Lindemann. *Z. Phys.*, 11:609, 1910.

[132] Duane C. Wallace. *Statistical Physics of Crystals and Liquids*. World Scientific Publishing Co. Pte. Ltd., River Edge, NJ, 2002.

[133] A. Haenstroem and P. Lazor. *J. Alloys Compd.*, 305:209, 2000.

[134] Lidunka Vocadlo and Dario Alfe. Ab initio melting curve of the fcc phase of aluminum. *Phys. Rev. B*, 65:214105, 2002.

[135] Giulia Galli, Richard M. Martin, Roberto Car, and Michele Parrinello. Melting of diamond at high pressure. *Science*, 250:1547, 1990.

[136] K. Takemura and K. Syassen. Pressure-volume relations and polymorphism of europium and ytterbium to 30 GPa. *J. Phys. F*, 15:543, 1985.

[137] F. Barson, S. Legvold, and F. H. Spedding. Thermal expansion of rare earth metals. *Phys. Rev.*, 105(2):418–424, Jan 1957.

[138] The exciting fp-lapw code. 2008. http://exciting.sf.net/.

[139] A. K. McMahan, K. Held, and R. T. Scalettar. Thermodynamic and spectral properties of compressed Ce calculated using a combined local-density approximation and dynamical mean-field theory. *Phys. Rev. B*, 67:075108, 2003.

[140] A. K. McMahan, Richard M. Martin, and S. Satpathy. Calculated effective hamiltonian for La_2CuO_4 and solution in the impurity anderson approximation. *Phys. Rev. B*, 38(10):6650–6666, Oct 1988.

[141] Gary N. Chesnut and Yogesh K. Vohra. Structural and electronic transitions in ytterbium metal to 202 GPa. *Phys. Rev. Let.*, 82:1712, 1999.

[142] K. Syassen, G. Wortmann, J. Feldhaus, K. H. Frank, and G. Kaindl. Mean valence of Yb metal in the pressure range 0 to 340 kbar. *Phys. Rev. B*, 26:4745, 1982.

[143] C. Dallera, O. Wessely, M. Colarieti-Tosti, O. Eriksson, R. Ahuja, B. Johansson, M. I. Katsnelson, E. Annese, J.-P. Rueff, G. Vanko, L. Braicovich, and M. Grioni. Understanding mixed valent materials: Effects of dynamical core-hole screening in high-pressure x-ray spectroscopy. *Phys. Rev. B*, 75:081101(R), 2006.

[144] J. J. Joyce, A. B. Andrews, A. J. Arko, R. J. Bartlett, R. I. R. Blythe, C. G. Olson, P. J. Benning, P. C. Canfield, and D. M. Poirier. Photoelectron spectroscopy of strongly correlated Yb compounds. *Phys. Rev. B*, 54(24):17515–17535, Dec 1996.

[145] Hitoshi Sato, Kunta Yoshikawa, Koichi Hiraoka, Masashi Arita, Koji Fujimoto, Kenichi Kojima, Takayuki Muro, Yuji Saitoh, Akira Sekiyama, Shigemasa Suga, and Masaki Taniguchi. Soft-x-ray high-resolution photoemission study on the valence transitions in $YbInCu_4$. *Phys. Rev. B*, 69(16):165101, Apr 2004.

[146] S. Schmidt, S. Hüfner, F. Reinert, and W. Assmus. X-ray photoemission of $YbInCu_4$. *Phys. Rev. B*, 71(19):195110, 2005.

[147] B. P. Doyle, E. Carleschi, E. Magnano, M. Malvestuto, A. A. Dee, A. S. Wills, Y. Janssen, and P. C. Canfield. Temperature-independent ytterbium valence in YbGaGe. *Phys. Rev. B*, 75(23):235109, 2007.

[148] R. I. R. Blyth, J. J. Joyce, A. J. Arko, P. C. Canfield, A. B. Andrews, Z. Fisk, J. D. Thompson, R. J. Bartlett, P. Riseborough, J. Tang, and J. M. Lawrence. Temperature-invariant valence-band $4f$ photoemission features in the heavy-fermion compound $YbAl_3$. *Phys. Rev. B*, 48(13):9497–9507, Oct 1993.

[149] Richard T. Scalettar, Reinhard M. Noack, and Rajiv R. P. Singh. Ergodicity at large couplings with the determinant Monte Carlo algorithm. *Phys. Rev. B*, 44(19):10502–10507, Nov 1991.

[150] O. Volnianska and P. Boguslawski. Moleculare magnetism of monoclinic SrN: a first-principles study. *Phys. Rev. B*, 77:220403, 2008.

[151] M. Labhart, D. Raoux, W. Känzig, and M. A. Bösch. Magnetic order in $2p$-electron systems: Electron paramagnetic resonance and antiferromagnetic resonance in the alkali hyperoxides KO_2, RbO_2, CsO_2. *Phys. Rev. B*, 20:53, 1979.

[152] M. Rosenfeld, M. Ziegler, and W. Känzig. X-ray study of the low temperature phases of alkali hyperoxides. *Helvetica Physica Acta*, 51:299, 1978.

[153] Gerhard H. Fecher *et al. Private communication*, 2007.

[154] S. C. Abrahams, R. L. Collins, and W. N. Lipscomb. The crystal structure of hydrogen peroxide. *Acta Cryst*, 4:15, 1951.